A Study on the MUCH Geometry Optimization and Physics Observables of the Proposed FAIR-CBM Experiment

Kalyan Dey

Department of Physics
Gauhati University

This thesis is submitted to
Gauhati University as requirement for the degree of
Doctor of Philosophy

Faculty of Science

August 2017

Certificate

This is to certify that the thesis titled "A Study on the MUCH Geometry Optimization and Physics Observables of the Proposed FAIR-CBM Experiment" is the result of research work of Kalyan Dey, carried under our supervision, submitted to Gauhati Uiversity for the award of the degree of Doctor of Philosophy in Physics.

This thesis conforms to the standard of PhD Thesis under Gauhati University including the standard related to plagiarism and has a similarity index not more than 20% (twenty percent), excluding the bibiliography.

10.8.17

Prof. B. Bhattacharjee, Supervisor
Professor
Department of Physics
Gauhati University

7/8/17

Prof. S. Chattopadhyay, Co-Supervisor

August 2017

डॉ. शुभाशीष चट्टोपाध्याय / Dr. Subhasis Chattopadhyay
वैज्ञानिक अधिकारी (एच) / Scientific Officer (H)
प्रमुख, प्रायोगिक उच्च ऊर्जा भौतिकी एवं अनुप्रयोग समूह
Head, Experimental high Energy Physics and Applications Group
वीईसीसी / VECC / DAE
1/AF, Bidhan Nagar, Kolkata-700064
पश्चिम बंगाल, भारत / West Bengal, India

Declaration

I hereby declare that this thesis is the result of my own research work which has been carried out under the guidance of Prof. B. Bhattacharjee of Gauhati University and Prof. S. Chattopadhyay of VECC, Kolkata. I further declare that this thesis as a whole or any part thereof has not been submitted to any university (or institute) for the award of any degree or diploma.

This thesis contains less than 90,000 (ninety thousand) words excluding bibliography and captions.

Kalyan Dey

August 2017

Acknowledgements

First and foremost, I would like to express my sincere appreciation and gratitude to my supervisor Prof. Buddhadeb Bhattacharjee for his guidance and generous support during the entire course of my research at Gauhati University. It is his marvelous teaching during my M.Sc., that inspired me a lot to pursue my research under his guidance. He has always provided me his helping hand when I am in difficulties. We always had plenty of critical and fruitful discussions regarding various research findings. Without his help and selfless support, the accomplishment of this thesis would not have been possible.

It is my privilege to acknowledge my co-supervisor Prof. Subhasis Chattopadhyay for his encouragement and support. Every discussion with him regarding my research is inspiring and fruitful. I learned a lot regarding various critical issues related to the `CBMROOT` software. Specially, I would like to thank him for providing me his time during my stay at VECC, where I was preparing to present my research related to CBM simulation for the CBM collaboration meeting.

I also wish to offer my sincere respect to all my teachers at Gauhati University for their teaching and encouragement. Further, I wish to offer my humble respect to (Late) Prof. Syed Abu Saleh Ahmed for his motivational teaching.

I would specially like to thank Dr. Volker Friese, the physics coordinator of the CBM collaboration for many helpful discussion. The discussions with him on various physics issues related to my research work was simply amazing. Further, I also would like to thank him for his hospitality during my visit to Germany.

I wish to take the opportunity to thank all the members of the CBM Collaboration specially Dr. P. Senger (spokesperson of CBM collaboration), Dr. Y. P. Viyogi, Partha da, Arun da, Hushnud, Mukesh, and Shabir for their constant support and encouragement.

I extend my sincere words of thanks to Prof. Steffen A. Bass of Duke University, USA for stimulating discussions regarding UrQMD physics. Further, I would like to thank Dr. Gunner Gräef for his support on various UrQMD related computational issues and incorporation of some useful changes in UrQMD code. The discussions with Prof. Hannah Petersen is also kindly acknowledged.

My heartiest thank goes to my senior Lab-mates – Barnali di, Rupalim di and Ranjan da for all their support and encouragement during the initial days of my stay in the Lab. We had shared many joyful moments together in our Lab. Also, I wish to thank my junior Lab mates – Nur, Pranjal, and Somen for always being there and bearing with me.

I wish to thank all my seniors at the Department of Physics, specially Simanta da, Samiran da, Nabaratna da, and Amir da for all their help and encouragement. I further like to acknowledge my juniors particularly Tapan, Baishali, Mausumi, Kuldeep, Tapashi, Luxmi, and Jugal for their cheerful company. Also, I like to convey my heartfelt thanks my friends Mintu, Sashikanta, Kamal Jyoti Nath for the joyful time we had spent together both at the department as well as at the university hostel. Specially, I like to thank Subhankar da for his kind support and brotherly affection.

I also thank Mr. Paran Goswami, my roommate at the V. V. Rao Research Scholar Hostel for staying with me in my ups and downs. Special thank goes to my hostel mates viz. Arun da, Biswa da, Khaund da, Ashish da, Phaguna da, Rituparna da, Nani da, Bidyout da, Mayur da, Bhupen da, Dhiraj da, Subhasis da, Biswajit da, Mazi da, Diganta da, Abhijit da, Pathok da, and Kibriya da for providing their personal and professional help all throughout. I also, like to acknowledge all the supporting staff of the hostel for their help and support.

I wish to thank Nihar da, Sudipan da, Subhash, Nasim, Sumit, Subikash, and Partha Bagchi for meaningful discussions in multiple occasions on various physics topic.

My heartfelt thanks to Dr. Bedangadas Mohanty and Dr. Ashish Choudhury for helpful discussions on heavy-ion physics during my stay at VECC, Kolkata. I also like to thank Prof. Rajeev S. Bhalerao of TIFR for helpful discussion during his visit to Gauhati University.

I also wish to thank all my colleagues at Bodoland University specially Dr. Rajeeb Brahma, Dr. Sanjeeb Baruah, Dr. Sanjay Basumatary, Dr. Dhrubajyoti Haloi, Dr. Dulur Brahma, Dr. Ananta Swargiary, Ms. Yutika Narzary for their constant support and suggestion.

I acknowledge the Department of Science and Technology (DST), Govt. of India for providing me with the necessary funding and fellowship to pursue my research at Gauhati University.

My heartfelt thanks goes to Tanushree for all her love, support and patience.

Finally, I would like to convey my deep sense of gratitude to my parents Mr. Kalipada Dey and Mrs. Aruna Dey for their unconditional love and affection and without their support, the accomplishment of this work would not have been possible. It is my father, who always taught me to think rationally and whose support helped me to achieve this feat. I will always be indebted to my mother for all her love and care. I would also like to thank my sister Mrs. Binita Dey Bhowmick and brother Mr. Bikash dey for their unconditional support and affection. Finally, I would like to pay my homage to my Pisi (Aunt) Late Kanika Das for her love and affection.

Abstract

The CBM experiment will utilize the unprecedented beam intensity of FAIR to study the rare probes (such as J/ψ, D-mesons etc.) of the fireball with considerable statistics. J/ψ suppression was predicted to be one of the critical signatures of QGP. The proposed MUon CHamber (MUCH) detector for the CBM experiment will detect J/ψ via dimuon measurement. In this thesis, an attempt has been made to optimize various parameters of the MUCH detector. The present study reveals that the optimized MUCH detector, coupled with the TOF is compatible enough for the J/ψ measurement at FAIR energies. Being leptons, muons do not participate in strong interaction and thus provide undistorted information of the interior of the fireball. Therefore, the temperature calculated from the transverse mass distribution of dimuons reflects the early stage temperature of the fireball. An attempt has therefore been made to study the sensitivity of the optimized MUCH detector for measuring the temperature of the fireball from the dimuon transverse mass spectra. The temperature calculated from the present study with reconstructed J/ψ is found to be in agreement with that of the MC values within the uncertainty indicating the usefulness of MUCH design for the CBM experiment.

At FAIR energies, very high baryon density ($\sim 5-10\rho_0$) would be produced and as a result, effects which couple with net-baryon density are expected to be very prominent in this energy regime. Net-baryon density distribution depends strongly on beam rapidity. The NA49 collaboration has reported a strong dependence of the width of the rapidity distribution on beam rapidity at SPS energies. Considering the large acceptance detector of the CBM experiment, the width of the rapidity distribution of various produced particles were estimated at FAIR energies with UrQMD generated Au+Au data. A comparison of the results of this investigation with NA49 results reveals a separate mass ordering for the studied mesons and baryons.

Further, net-baryon density distribution might influence other observables as well. For example, there are a number of strange particles that do (not) contain leading quarks i.e. K^+, Ξ^-, Λ (K^-, $\bar{\Xi}^+$, $\bar{\Lambda}$, Ω^-, $\bar{\Omega}^+$) and hence strangeness enhancement factor (E_S) could get influenced by net-baryon density distribution. Moreover, due to the limitation of detector acceptance, past and existing heavy-ion experiments could measure E_S at mid rapidity only. Steinheimer et al. using UrQMD hinted towards the possibility of local violation of strangeness conservation. The study of rapidity dependent strangeness enhancement is therefore quite significant and hence rapidity dependent strangeness enhancement has been studied for various strange particle. The rapidity dependent strangeness enhancement exhibits two distinct patterns for particles containing and not containing leading quarks.

Table of contents

List of figures

List of tables

1

Introduction

The asymptotic freedom – the peculiar property of strong interaction led the physicist to believe that under the extreme condition of temperature and/or pressure, the ordinary nuclear matter undergoes a phase transition to form a deconfined soup of quarks and gluons known as Quark Gluon Plasma (QGP). The study of QGP is significant from the point of view that this very state of matter is believed to exist just few microsecond after the big bang and presently may lie at the core of the neutron star. Study of QGP will help to better understand strong interaction and QCD, CP violation, and many other fundamental laws of physical world. Relativistic heavy-ion collisions are the only way before the experimentalists to create such a hot and dense matter in the laboratory. Over the past three decades, the hadron-QGP phase transition has been studied by means of the large collaborative fixed target experiments at the Alternating Gradient Synchrotron (AGS), Super Proton Synchrotron (SPS) facility and few collider experiments at the Relativistic Heavy Ion Collider (RHIC) and more recently at Large Hadron Collider (LHC). In future, a new accelerator facility known as FAIR (Facility for Antiproton and Ion Research) will be set up where a fixed target experiment called the Compressed Baryonic Matter (CBM) experiment will be conducted (in the year 2022) to study the QCD phase diagram at the region of moderate temperature and high baryon density. The unprecedented beam intensity of FAIR will make it possible to study the rare probes of the fireball and might provide a comprehensive information of the hot and dense matter

created. In this chapter, an attempt has been made to provide a brief introduction of the Standard model, Quantum Chromodynamics: the underlying theory of strong interaction and the study of QGP by means of heavy-ion collision.

1.1 Standard Model and Quantum Chromodynamics

Standard Model (SM) of particle physics is the underlying theory concerning three of the four known fundamental forces or interactions of nature viz. Electromagnetic, Strong and Weak, barring Gravity. According to Standard Model, the whole universe is composed of two basic types of particles – matter particle and the fields particles responsible for the interaction between the matter particles [1–3]. Further, there are two kinds of matter particles – *quarks and leptons*. In the present understanding, each group consists of six particles. For instance, quarks come in six flavors e.g. u, d, s, c, b and t. Similarly, the lepton family includes e, μ, τ and the associated neutrinos viz. ν_e, ν_μ, ν_τ[1]. Both quarks and leptons fall under the category of fermions, the particle with spin $S = \frac{1}{2}$ and obey Fermi-Dirac statistics. On the other hand, the field particle includes photon (γ), $W^{\pm}$, Z^0 and gluon (g). For example, photons (γ) mediate the electromagnetic interaction between two electrically charged particles, $W^{\pm}$ and Z^0 mediate weak interaction between different flavors of quarks and leptons. Similarly, gluons are responsible for the strong interaction between the particles having color charge i.e. quarks. The field particles fall under the category of bosons, the particle with integral spin and obey Bose-Einstein statistics. Standard Model was developed in the early 1970s which successfully explains nearly all the experimental findings. Over the years, the Standard Model (SM) of particle physics has become one of the well-tested physics theory. Many predictions of the model have been experimentally confirmed e.g. Higgs boson, an essential component of the SM has recently (in the year 2012) been discovered by CMS and ATLAS experiment at Large Hadron Collider (LHC) at CERN [4, 5]. The number of particles which are included in the SM is listed in the left panel of Fig. 1.1.

Quantum Chromodynamics (QCD) is the microscopic quantum field theory of strong interaction [6]. In QCD, color charge plays the same role as electrical charge does in Quantum Electrodynamics (QED). At very short distances, the force among quark and gluons are very similar to the ones between electrons and photon, the electric charge being replaced by eight color charge [6]. The strong interaction potential between two color charge (quarks) can be

[1] Besides quarks and leptons, anti-quarks and anti-leptons are also included in the SM.

written as,

$$V(r) = -\frac{\alpha_s}{r} + kr, \tag{1.1}$$

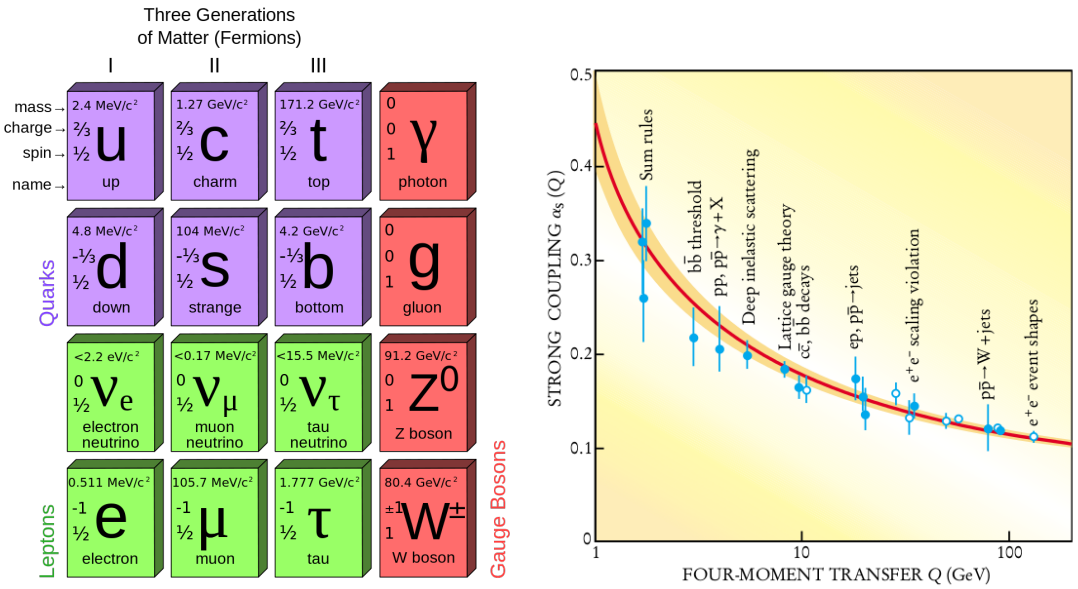

Fig. 1.1 **Left:** Listing of the particles included in the Standard Model [7]. **Right:** The strong coupling constant as a function of momentum transfer calculated from various experiments as shown by the data points. The solid line correspond to the pQCD estimation where the measured coupling of a quark pair to a virtual gluon at the Z boson mass is an empirical input; the orange swath reflects its uncertainty [8].

where, α_s is the strong coupling constant which physically signifies the strength of the interaction, r is the distance between the interacting color charges, and k represents the string tension between the quarks. The first term in Eqn. 1.1 is nothing but the Coulomb-like term which is dominated at short distances. On the other hand, the linear term (second term) is motivated by string picture of quark confinement [9]. In this picture, quarks are considered to be interacted through color string. If the distance between the interacting quarks increases, the string tension k increases, and more energy is required to separate them. In other words, an infinite amount of energy will be required to free a quark from a hadron. This peculiar property of strong interaction is known as confinement[2]. The strong coupling constant is not a fixed quantity rather it is energy dependent, also known as *running coupling constant*. The

[2]This property explains why free quarks have never been observed.

expression for strong coupling constant can be written as,

$$\alpha_s(Q^2) = \frac{12\pi}{\left[\beta \ln(Q^2/\Lambda^2_{QCD})\right]}, \tag{1.2}$$

where, Λ_{QCD} is the QCD scale whose value is roughly equal to 200 MeV, Q^2 is the momentum transfer. One striking fact about QCD is that the mediator of strong interaction i.e. gluons (g) can interact with itself by virtue of its color charge[3]. Similar to QED, in QCD also due to vacuum polarization the color charge is screened causing the coupling constant to be energy dependent. Although the quark polarization causing a screening effect, the gluon polarization providing an anti-screening effect [10]. As a result, there will be a competition between quark-polarization and gluon-polarization. The critical parameter β is given by [10],

$$\beta \equiv 2f - 11n, \tag{1.3}$$

where, f is the number of quark flavor while n represents the number of colors. If β is positive, then as in QED, the effective coupling constant increases at short distance; if it is negative, the coupling decreases (from Eqn. 1.2). In Standard Model, $f = 6$ and $n = 3$ which makes $\beta = -21$. This is the reason why the effective strong coupling strength decreases at short distances (see right panel of Fig. 1.1). This phenomenon of strong interaction is known as asymptotic freedom[4] [11, 12]. The discovery of asymptotic freedom rescued the Feynman calculus (perturbation method) as a legitimate tool for QCD, in the high energy regime [10].

1.2 Quark Gluon Plasma

The very idea of asymptotic freedom led Collins and Perry to suggest that under the condition of extremely high density, quarks are too close to assigning them to a particular hadron [13]. The matter at such high densities is suggested to a be quark soup [13] which is believed to exist at the core of neutron stars[5]. Similarly, at very high temperature (or at very large momentum transfer), the weakly coupled color charges or quarks due to asymptotic freedom can move freely within a volume larger than the hadronic volume. Such a deconfined state of matter consisting of thermalized quarks and gluons are termed as Quark-Gluon Plasma (QGP) [14].

[3] the QED counterpart of gluon i.e photon is charge less and thus can't interact with itself

[4] Gross, Wilczek and Politzer were awarded Nobel prize for the discovery of asymptotic freedom in 2004

[5] The matter density at the core of neutron stars is $\sim 10^{16} - 10^{17}$gm.cm^{-3}

In order to understand the dynamics of the created matter, the relevant thermodynamic quantities e.g. pressure, temperature, and energy density can be calculated approximately by assuming the produced matter to consist of non-interacting relativistic massless particles i.e. relativistic ideal gas and is given by,

$$P = g_{\text{eff}} \frac{\pi^2}{90} T^4 \qquad \text{and} \qquad \varepsilon = 3P = g_{\text{eff}} \frac{\pi^2}{30} T^4, \tag{1.4}$$

where, g_{eff} is the number of effective degrees of freedom.

For simplicity, if one approximates the hadron gas as a pion gas, the effective degrees of freedom will be equal to 3. On the other hand, if QGP is believed to have consisted of three flavors of quarks, their anti-particles, and gluons, the effective degrees of freedom become $g_{\text{eff}} = (g_{\text{gluon}} + \frac{7}{8} g_{\text{quark}}) = (8 + \frac{7}{8} N_c N_f N_s N_a) = 47.5$, where, N_c = number of colors = 3, N_f = number of flavors = 3, N_s = number of spin degrees of freedom = 2, and N_a = degrees of freedom for particles and anti-particles = 2. Thus, by calculating the thermodynamic quantities of interest e.g. P/T^4 or ε/T^4, one can have an idea about the effective degrees of freedom of the thermodynamic phase.

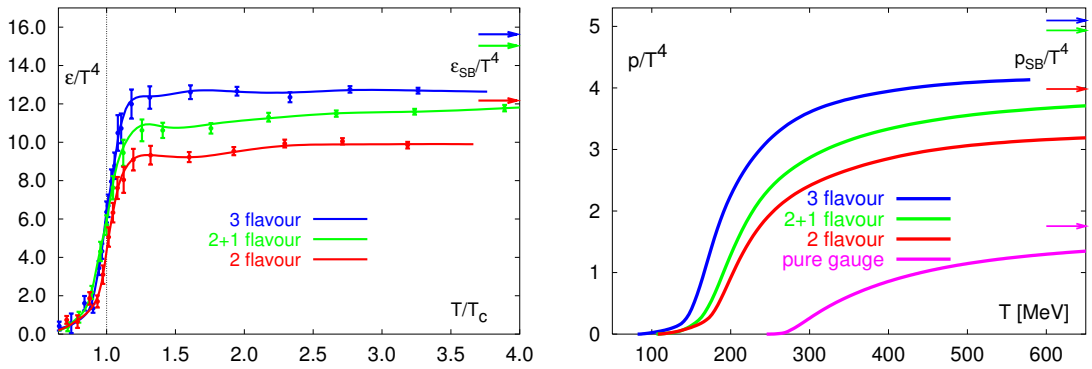

Fig. 1.2 **Left:** ε/T^4 as a function of temperature normalized by the critical temperature (T_c). The red, green and blue lines (also points) signify the lattice QCD calculation using 2-flavor, 2+1 flavor and 3-flavor respectively. **Right:** p/T^4 as a function of temperature. The horizontal arrow indicates the Stefan-Boltzmann limit [15].

Although perturbative QCD (pQCD) calculations work nicely at large momentum transfer (Q), yet, at small Q corresponding to a distance of the order of hadronic size ($\sim$ 1fm), perturbative calculation fails and thus non-perturbative approach is essential. One such non-perturbative approach is the Lattice QCD [16]. Lattice QCD is the branch of QCD based on numerical Monte-Carlo simulation where the space-time is treated as discrete points on a lattice. Lattice QCD predicted a phase transition from hadronic matter (relevant degrees of freedom are hadronic) to a deconfined state of quarks and gluons (relevant degrees of

freedom are partonic) at a critical temperature of about 170 MeV and at a critical energy density of 1 GeV/fm^3 [17, 15]. Figure 1.2 shows the variation of energy density and pressure both normalized by T^4 as a function of temperature as calculated from Lattice QCD simulation[6] [15]. The sudden abrupt change in both pressure and energy density at a particular temperature $T = T_C$ is an indicator of the phase transition from hadronic to partonic degrees of freedom.

Although Lattice QCD predicted a clear cut indication of phase transition, yet, the order of phase transition is a matter of debate. In Lattice QCD calculation, the order of phase transition depends both on the masses and number of quark flavors considered in the calculation. At moderate temperature and high baryon density the order of phase transition is predicted as 1st order, whereas, Lattice QCD calculation, using non-zero quark masses (m_u , $m_d \neq 0$) predicted a rapid cross-over at high temperature and low baryon density [18–20].

1.3 QCD phase diagram

Figure 1.3 is the schematic illustration of the QCD phase diagram in which temperature is plotted as a function of net-baryon density. It is evident from the figure that at a very low net-baryon density (or almost at zero baryon chemical potential, $\mu_B = 0$), the phase transition occurs from hadronic to deconfined QGP phase nearly at the temperature of 170 MeV. This region of the phase diagram corresponds to the early universe i.e. just a few micro-seconds after the Big Bang, where, there is a similar transition from the possible QGP to the hadronic phase. Lattice QCD predicted the nature of the phase transition to be a smooth crossover at vanishing net-baryon densities [21, 22].

On the other extreme, i.e. at intermediate temperature and at high baryon density, the Lattice calculations suggested a 1st order phase transition. This very end of the phase diagram corresponds to the superdense core of the neutron star. The point along the phase boundary at which the 1st order transition line ends is known as the critical point. It is to be noted that, unlike the phase diagram of water, the QCD phase diagram is not fully quantified e.g. the exact location of the phase boundary and critical point is still unknown and is a matter of investigation. Although there are some theoretical estimates about the location of the critical point, the experimental verification is yet to be done. The Lattice QCD calculation at finite baryon density [24] predicted the location of the critical point to be at T = 160 MeV and $\mu_B = 725$MeV. However, the result need to be improved further as a unphysically large value of the quark mass was considered during the Lattice calculation [24].

[6]The quantity ε/T^4 is proportional to the number of degrees of freedom as clearly seen from equation 1.4

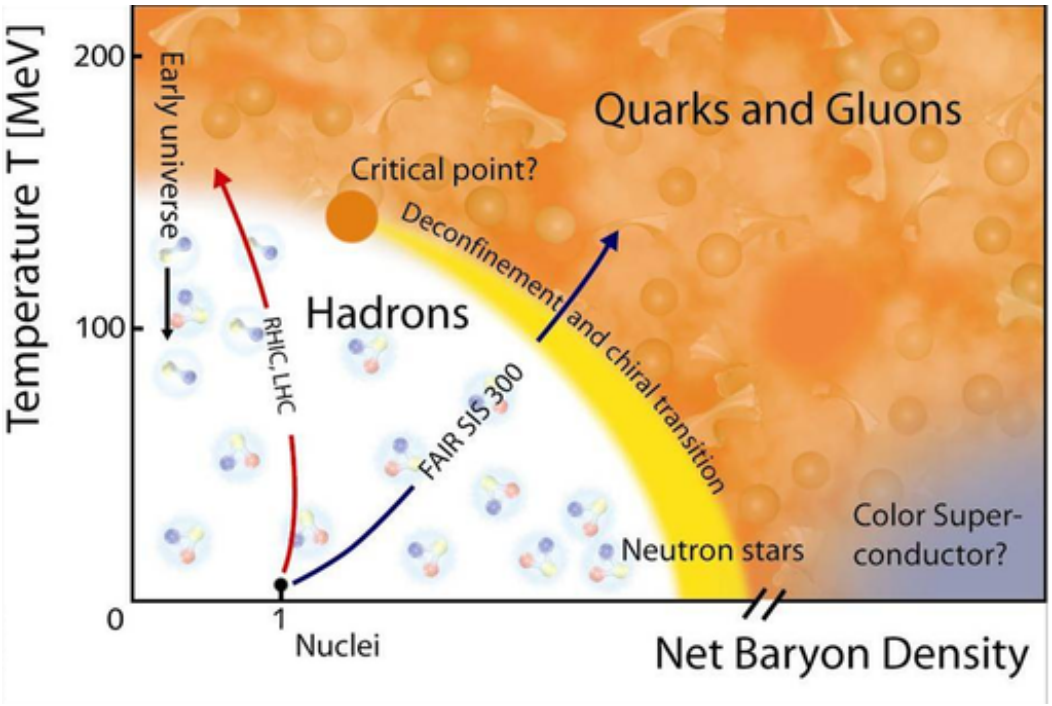

Fig. 1.3 Schematic representation of the phase diagram of strongly interacting matter [23].

1.4 Relativistic heavy-ion collision

One can reach the Quark-Gluon Plasma phase either by having a situation with high temperature and low net-baryon density or with intermediate temperature and high net-baryon density. For the first time in 1975, T.D. Lee [25] suggested that a superdense matter could be created by colliding heavy ions at relativistic speeds. Nuclear matter away from normal density and temperature can only be produced on this earth through high energy heavy-ion collisions and to achieve this, a large number of accelerators have been set up all over the world. An experimental overview of the past and ongoing heavy-ion experiments is presented in the following section.

1.4.1 Experimental overview of heavy-ion experiments

Bevalac[7] at the Lawrance Berkeley National Laboratory (LBNL), USA was the first ever heavy-ion accelerator facility used for the study of nuclear equation-of-state and the search for Quark Gluon Plasma. Using this facility for Ca+Ca and Nb+Nb collisions at $E_{lab} = 400A$ MeV, and with the help of 'Plastic ball' spectrometer, the first evidence of *collective flow*

[7]The name Bevalac was coined by the physicist Ed Lofgren when the Bevatron was coupled with SuperHILAC (Super Heavy Ion Linear Accelerator) in 1971.

was found [26]. A few years later, at the GSI Helmholtz Centre for Heavy Ion Research, Germany, new accelerator facilities viz. Universal Linear Accelerator (UNILAC: 2-11.4A MeV) and Schwer Ionen Synchrotron (SIS18: 0.010-2A GeV) were developed in order to boost the experimental research on heavy-ion physics. In the meantime, at the Brookhaven National Laboratory (BNL), USA, a new accelerator facility called Alternating Gradient Synchrotron (AGS) had become operational, which can accelerate as heavy as Au-ion up to a maximum energy of 11.4A GeV. Several experiments such as E866, E877, E802, E891, E896, and E917 were performed using the AGS facility. On the other hand, at the European Organization for Nuclear Research (CERN), a new accelerator facility known as SPS (Super Proton Synchrotron) which is the successor of PS (Proton Synchrotron) has come up that can accelerate Pb-ions with the maximum energy of E_{lab} = 158A GeV ($\sqrt{s}$ = 17.8 GeV). Different experiments like WA80, WA97, WA98, NA34, NA35, NA44, NA45/CERS, NA49, NA50, NA57, NA60 etc. were conducted over the several decades at CERN. Several fruitful results were obtained over the span of few decades both from AGS and SPS facilities. In order to scan the QCD phase diagram at the region of high temperature and low net-baryon density, the situation demands to build accelerators even with higher energies. In view of this demand, a dedicated heavy-ion collider facility known as Relativistic Heavy Ion Collider (RHIC) at BNL has been designed, which is capable of accelerating Au-ions to the maximum energy of $\sqrt{s}$ = 200 GeV. BRAHMS, PHENIX, STAR, PHOBOS are the different existing experiments running at the RHIC facility. Observation of large *elliptic flow* and the *jet quenching* were among the top two remarkable results obtained by the experiments at RHIC. Further, at RHIC, a beam energy scan (BES) program is also underway in order to scan the low energy regime of the QCD phase diagram and to locate QCD critical point. Large Hadron Collider (LHC) at CERN, on the other hand, is the collider facility built to provide lead (Pb) ions at the highest ever beam energies i.e. $\sqrt{s}$ = 2.76, 5.5 and 7 TeV. ALICE, ATLAS, CMS and LHCb are the four major experiments at CERN's LHC. A list of the past and ongoing heavy-ion experiments is provided in the following table.

1.4.2 Space-time evolution of heavy-ion collision

Heavy ions at relativistic velocities are believed to be Lorentz contracted along the direction of motion and thus appeared to be '*disc*'-like shaped as observed from the laboratory frame of reference. As a matter of fact, if two such relativistic heavy ions collide head-on, nearly all the nucleons from each ion collide almost simultaneously. As a result, within the overlapping region, almost the entire kinetic energy of the beam is deposited and a huge energy density and temperature is believed to be produced. Figure 1.4 illustrates the space-time evolution of heavy-ion collision. Two possible situations might occur when two relativistic heavy

Experimental Facility	**Colliding system with energy**	**Experiments**
BEVLAC (1975-1993)	Ar+KCl (1.8A GeV), Ca+Ca, Nb+Nb (400A MeV)	Streamer Chamber, Ball/Wall, EOS Plastic
SIS (1990-now)	Ni+Ni, Au+Au (0.5-2A GeV)	FOPI, KaoS, ALADIN, HADES
AGS (1086 - 1997)	Si+Al, Si+Pb (14.6A GeV), Au+Au (1.96A, 4A, 5.93A, 7.94A, 11.4A GeV)	E866, E814/E877, E802, E891, E896, E917
SPS (1986-2003)	O+O (60, 200 GeV/c), S+S, S+Au, S+U (200 GeV/c) Si+Al, Pb+Pb (158 GeV/c)	WA80, WA97, WA98, NA34, NA35, NA44, NA45/CERS, NA49, NA50, NA57, NA60
RHIC (2000-)	Au+Au (7.7, 11.5, 14.5, 19.6, 27, 39, 62.4, 200 GeV) Cu+Cu (62.4, 200 GeV)	BRAHMS, PHENIX, STAR, PHOBOS
LHC (2007 -)	Pb+Pb (2.76, 5.5, 7 TeV)	ALICE, CMS, ATLAS
SPS (2011-2015)	p+p, p+Pb, Be+Be, Ar+Ca, Xe+La, Pb+Pb (13A, 20A, 30A, 40A, 80A GeV), Be+Be (158A GeV)	NA61/SHINE

Table 1.1 The details of the past and ongoing heavy-ion experimental facilities along with the names of different experiments and the collision systems with their energies.

nuclei collide with each other. After the collision, if the temperature and energy density or matter density fail to attain the critical value, the system will believe to be composed only of hadrons (as shown by the left-hand side of Fig. 1.4) and after sufficient amount of scattering, the system will behave as hadron gas [27]. The hadrons so produced will collide inelastically among themselves to produce new hadrons and photons. Due to the pressure gradient in the medium with the surrounding vacuum, the system continues to expand with the further fall of temperature. If the temperature of the system falls below T_{ch}, the hadronic interactions become elastic with the cease of new particle production and chemical freeze-out occurs. The temperature T_{ch} is known as chemical freeze-out temperature and below this temperature the particle compositions (or particle ratios) become fixed i.e. the collisions become elastic. On further expansion of the system, the temperature reaches T_{fo}, the kinetic or thermal freeze-out temperature below which, the system dilutes to such an extent that the mean-free-path becomes larger than the system size. Below this temperature, the elastic collision between hadrons ceases and no change in momentum of the particle is further expected. The particles then freely fly to fall onto the detector [27].

On the other extreme, if the temperature and energy density or matter density exceed the critical value, Quark-Gluon Plasma might be formed as is shown in the right hand side of the

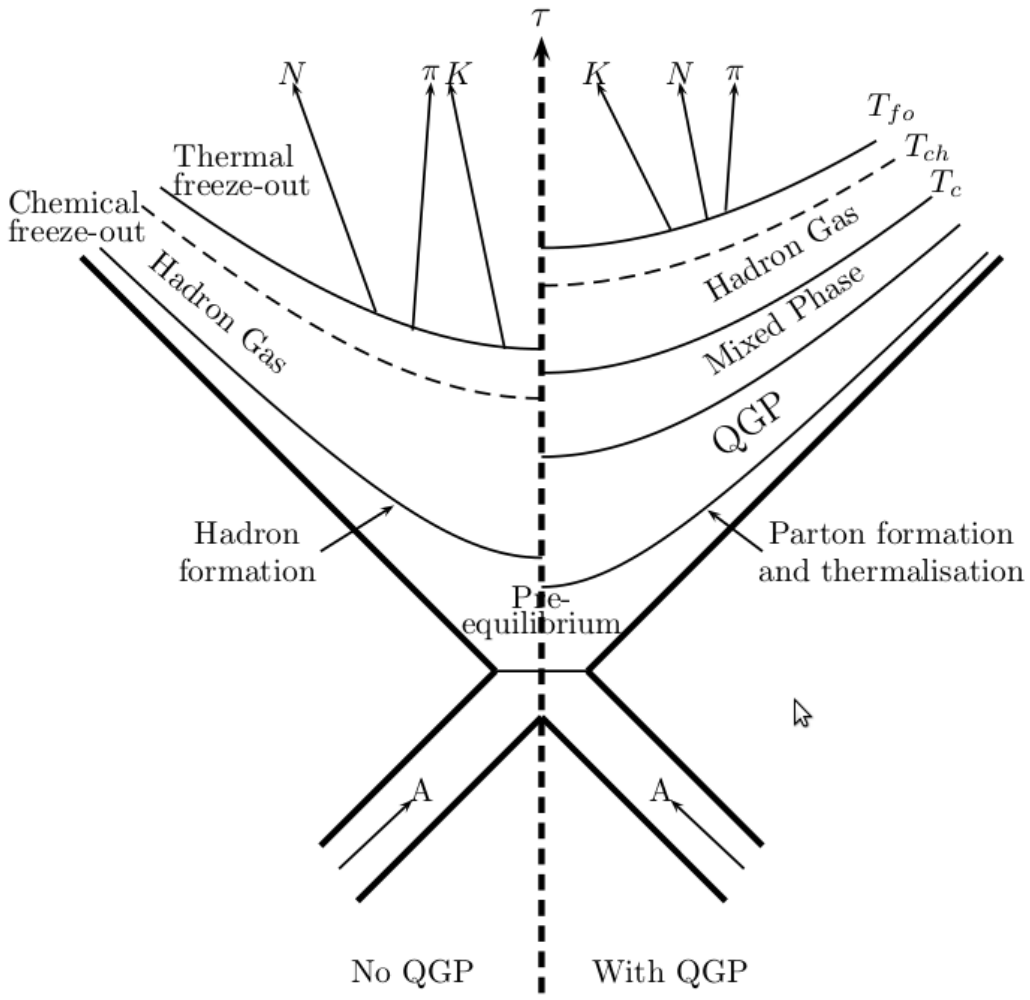

Fig. 1.4 A schematic illustration of the space-time evolution of high energy heavy-ion collision [27].

Fig. 1.4. In QGP-scenario, where the energy/matter density is so large that partons (quarks and gluons) are liberated out of the hadrons in the violent collisions between the nucleons and form a soup of quarks and gluons. At this stage, the produced matter is yet to achieve thermal equilibrium. This stage of the evolution is known as the pre-equilibrium stage. If the produced partons interact sufficiently in the medium and if the mean-free paths of the collisions are smaller than the system size, the medium might subsequently achieve thermal equilibrium and can be termed as a phase of matter with a definite equation-of-state (EOS). This phase of matter is known as Quark-Gluon Plasma. Due to the build-up of a pressure gradient in the medium with the surrounding vacuum, the produced QGP expands and during the expansion, the temperature of the medium drops down. The collisions between the

partons become less violent. When the temperature of the medium becomes smaller than the critical temperature, partons coming in close contact with each other are unable to overcome the strong attractive potential and hadronization begins to take place. Since the formation time from partons to hadrons is finite, the system evolves through a mixed phase, where there will be a simultaneous existence of partons and hardons [27]. After a short while ($\sim$ few fm/c), when all the partons get converted into hadrons, the produced hadron gas will further expand in the similar fashion as described earlier and will pass through both chemical and kinetic freeze-out stages and finally fly to the detectors for their detection and identification.

1.5 Observables of heavy-ion collisions

In the heavy-ion collision, one starts with hadrons (nuclei) and ends up with hadrons again. The deconfined partons coalesce into hadrons in a time $\sim 10^{-23}$ seconds. The hadrons thus produced move almost with the velocity of light and fly to the detectors within a time scale of $\sim 10^{-9}$ second or so. Thus, be it the signals of QGP, or any other thermodynamical properties like temperature, pressure, energy density etc. of heavy-ion collisions, cannot be realized directly. One, therefore, has to rely on a number of indirect evidence. The observables of HIC can broadly be categorized into three categories viz. global observable or soft probes (particles with p_T up to 2 GeV/c), hard probes, and electromagnetic probes. Global observables basically quantify the bulk features of the collisions, whereas, hard probes generally address the medium-induced modification of processes known in the collisions of elementary particles and the electromagnetic probes, on the other hand, characterizes the early-stage dynamics of heavy-ion collisions. The global observable includes rapidity, pseudo-rapidity and transverse energy distributions of the bulks (charged hadrons) constituting almost 95% of the total number of particles produced. It further includes particle multiplicities, abundance ratios, momentum distributions, strangeness enhancement, collective flow (both transverse and longitudinal flow) etc. of identified particles. Similarly, the hard probes include J/ψ suppression, Jet quenching etc. On the other hand, electromagnetic observable refers to the study of photons and dileptons.

1.5.1 Global observables

Rapidity and pseudo-rapidity and transverse energy distribution

The first step towards the search of Quark-Gluon Plasma is to establish whether the energy density created in the collisions surpass the theoretically predicted value which is $\sim$1 GeV$/$fm^3 [28]. Charged particle rapidity/pseudo-rapidity distribution is one of the first mea-

surement performed in order to characterize the global properties of high-energy heavy-ion collisions. A detailed discussion regarding rapidity distribution and its significance is presented in section 4.2 of Chapter 4. The charged particle pseudo-rapidity density ($dN_{ch}/d\eta$) or rapidity density (dN/dy) according to Landau's hydrodynamic model is proportional to the entropy of the system and hence to the energy density produced in the collision [29]. Further, the mean transverse energy per unit pseudo-rapidity $\langle dE_T/d\eta \rangle$ contains all important information regarding how much of the initial longitudinal energy carried by the incoming nuclei is converted into energy carried by the particles produced transverse to the beam axis [30]. The energy density was measured by various heavy-ion experiments at AGS, SPS, RHIC and recently at LHC accelerator facilities and their findings are summarized in Table 1.2. It is clearly visible from the Table 1.2 that all the mentioned heavy-ion experiments can create a situation conducive to the creation of QGP. It is to be noted that the FAIR-CBM experiment [31–35] whose energy lies between AGS and SPS energies is well suited for the creation of QGP.

Accelerator Facilities	**Energy** ($\sqrt{s}$)	**Energy density** (GeV/fm^3)
AGS	5 GeV	1.5
SPS	17 GeV	2.9
RHIC	200 GeV	≈ 5
LHC	2.76 TeV	$\approx 12 - 14$

Table 1.2 The estimated energy density at various experimental facilities [36–40]

The rapidity distribution of net-protons, on the other hand, can not only determines the energy available for the particle production but also determines the stopping of the ions due to their mutual interaction. A compilation of net-proton rapidity distribution from different experiments is shown in Fig. 1.5 [41]. It is clearly seen from the figure that at AGS, the net-proton rapidity distribution is peaked at mid-rapidity indicating a large stopping i.e. most of the baryons ended up near mid-rapidity. As one go higher up in the energy, one finds a clear development of a baryon-free region at mid-rapidity.

The energy required for the particle production comes from the kinetic energy lost by the baryons during collisions, which can be determined by measuring a quantity called 'mean rapidity loss' and is defined as [42, 43],

$$\delta y = y_b - \frac{2}{N_{part}} \int_0^{y_b} y \frac{dN_{B-\bar{B}}}{dy} dy, \tag{1.5}$$

where, y_b is the beam rapidity, $dN_{B-\bar{B}}/dy$ represents the rapidity distribution of net-baryon number and N_{part} is the number of participant in the collision.

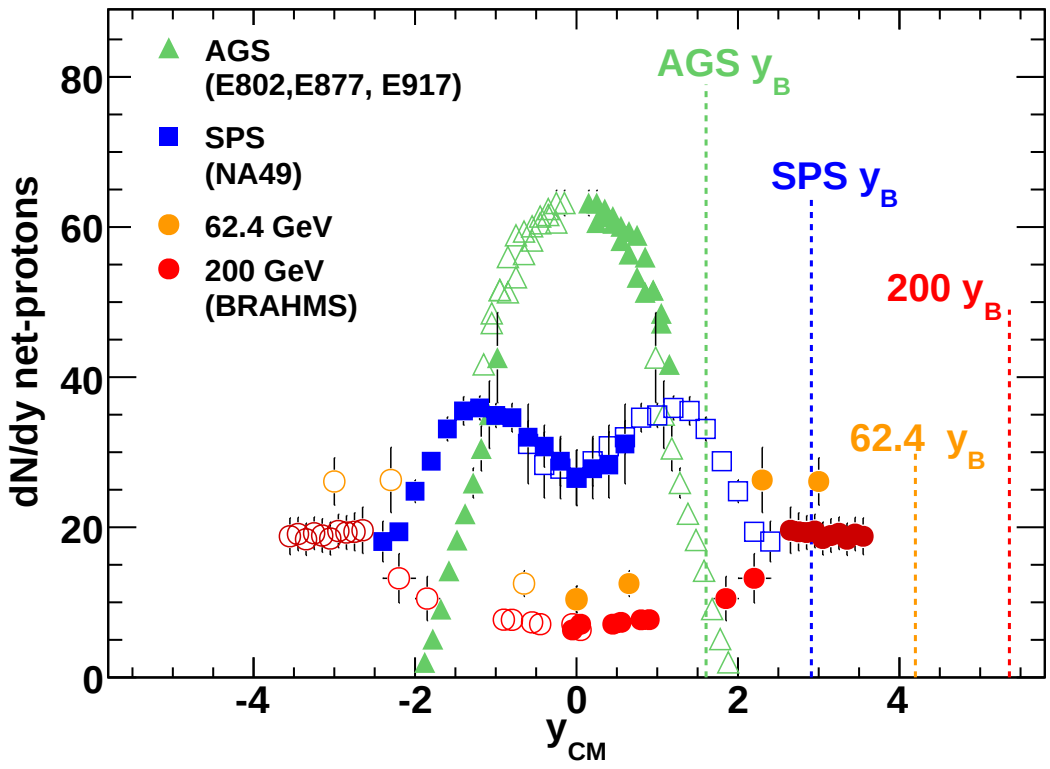

Fig. 1.5 A compilation of net-proton rapidity distribution from different experiments. The vertical dashed lines represents the beam rapidity [41].

Mean rapidity loss is nothing but the difference between beam rapidity and mean rapidity of the net-baryons between $y = 0$ to y_b.

Particle multiplicity

In heavy-ion collisions, the incident beam energy is converted into the creation of particles consisting of both baryons and mesons. At lower beam energies e.g. SIS18/AGS energies due to stopping, the net-baryon density at mid-rapidity is large and the created matter is generally baryon-dominated and is termed as baryonic matter. On the other hand, at higher beam energies e.g. RHIC and LHC, the incident nuclei almost pass through each other and as a result of that the net-baryon density of the created fireball will be close to zero. In this regime, pair creation is the major source of particle production and the created matter is meson-dominated. Therefore, excitation function of particle multiplicity can provide a better understanding of the dynamics of the fireball and thereby the particle production mechanism. A compilation of particle multiplicity at mid-rapidity in central AA collisions is illustrated in the left panel of Fig. 1.6 [44, 45]. The experimental data has been scaled to the number of

participant nucleons, $N_{part} = 350$[8]. As is clear from the figure that the lower energy domain is mainly contributed by the incoming protons while the higher energy regime is dominated by the number of produced pions and kaons. The second feature that can be noticed from the figure is that the yield of strange hadrons follows a sharp increase with energy and the characteristic feature is controlled by their quark content [44, 45]. Further, at lower energies (AGS and low SPS energies) both the yield of K^+ mesons and Λ hyperons[9] are larger than that of K^- mesons. Despite the huge mass difference, the excitation function of the yield of K^+ and Λ possesses a remarkable similarity. This feature can be explained from the point of view that K^+ and Λ respectively contains a newly produced $\bar{s}$ and s quark respectively and thus both of them are produced as a consequence of associated strangeness production, a remarkable feature of strong interaction[10] [44, 45]. Similarly, anti-proton and anti-hyperon which contains produced quarks only show a strong energy dependence. On the other hand, at higher beam energies like RHIC, the difference between the particle and anti-particle production is seen to be negligible as a consequence of small net-baryon density at higher energies [44, 45].

The right panel of Fig. 1.6 shows the excitation function of hadron yields measured at (or extrapolated to) full solid angle (4π). It is interesting to see from the figure (also seen from the left panel) that the yield of Λ hyperon shows a pronounced maximum near $\sqrt{s} = 7 - 10$ GeV, a feature that can be attributed to the fact that at the higher energy regime the baryon chemical potential decreases indicating the transition from baryon to meson dominated matter [44, 45].

Particle abundance ratio

Statistical hadronization or thermal models are found to be extremely successful in explaining the particle multiplicity in both elementary and heavy-ion collisions [46, 44]. The main assumption of the thermal models is that the fireball created in heavy-ion collisions is of thermal origin [46, 44]. At chemical freeze-out, the particles are believed to be produced from a thermal source and are characterized by the two thermal parameters viz. temperature and chemical potential [45]. The particle multiplicity ratios[11], measured [47–50] in a wide range of beam energies ($\sqrt{s}$ = 2.7 – 200 GeV), were fitted in order to extract the thermal parameters (μ_B and T). The particle multiplicity, as shown in the left panel of Fig. 1.6, has

[8] since the centrality selection is different for different experiment.

[9] both K^+ and Λ contains one produced strange quark.

[10] Associated strangeness production is the direct consequence of strangeness conservation in strong interaction

[11] Hadron yield ratios instead of yields itself is used for fitting in order to cancel out the fireball volume parameter [45].

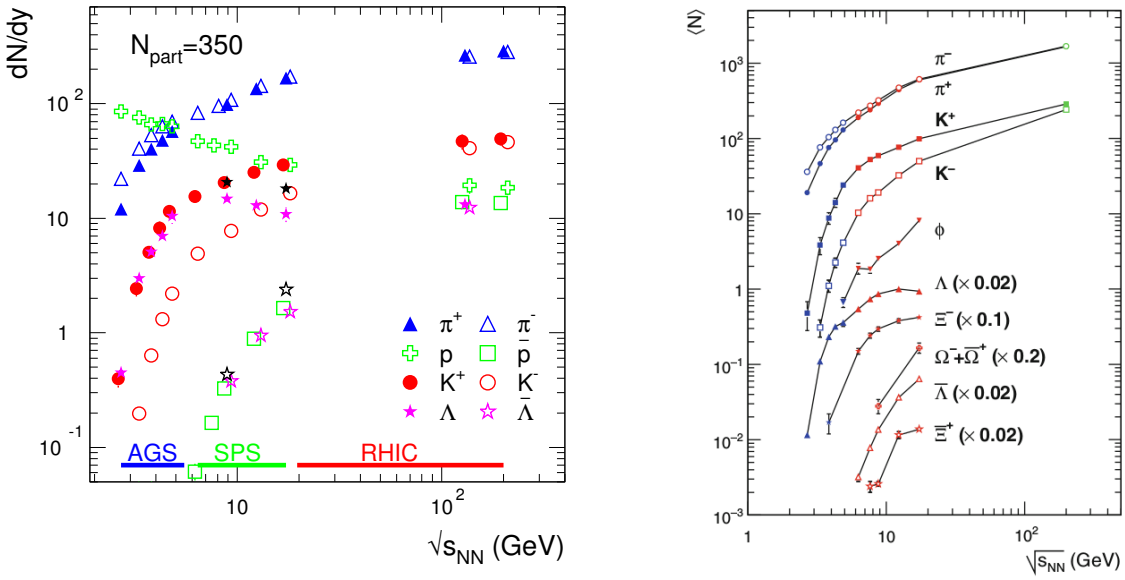

Fig. 1.6 **Left:** Particle multiplicity at mid-rapidity as a function of center of mass energy. **Right:** Excitation function of particle yield measured in (or extrapolated to) full solid angle (i.e. 4π) in central nucleus-nucleus (Au+Au, Pb+Pb) collisions.

been fitted with the help of thermal model and the extracted parameters have been plotted as a function of energy (see left panel of Fig. 1.7). It is seen from the figure that the baryochemical potential decreases exponentially as a function of energy, whereas the chemical freeze-out temperature increases rapidly and saturates nearly at $T \sim 160$ MeV. The correlation between the extracted parameters are shown in the QGP phase diagram (see the right panel of Fig. 1.7). The Lattice QCD calculations with two flavors i.e u and d with masses close to physical quark masses are also shown in the diagram. The open triangle represents the QCD critical point in the diagram where the 1st order phase transition ends and beyond which there is a cross-over. It can also be seen from the plot that, beyond the laboratory energy of 30A GeV i.e near 40A GeV and above, the thermal parameters match with the phase boundary calculations with Lattice QCD implying that hadron yields are frozen at the phase boundary.

Transverse momentum distributions

Transverse momentum (p_T) distribution of the produced particles is one of the most important observables in the heavy-ion collision. The transverse momentum distribution reflects the kinetic freeze-out temperature as well as the radial flow of the fireball. The radial flow is highly sensitive to the equation-of-state [52] and hence by comparing the experimental data

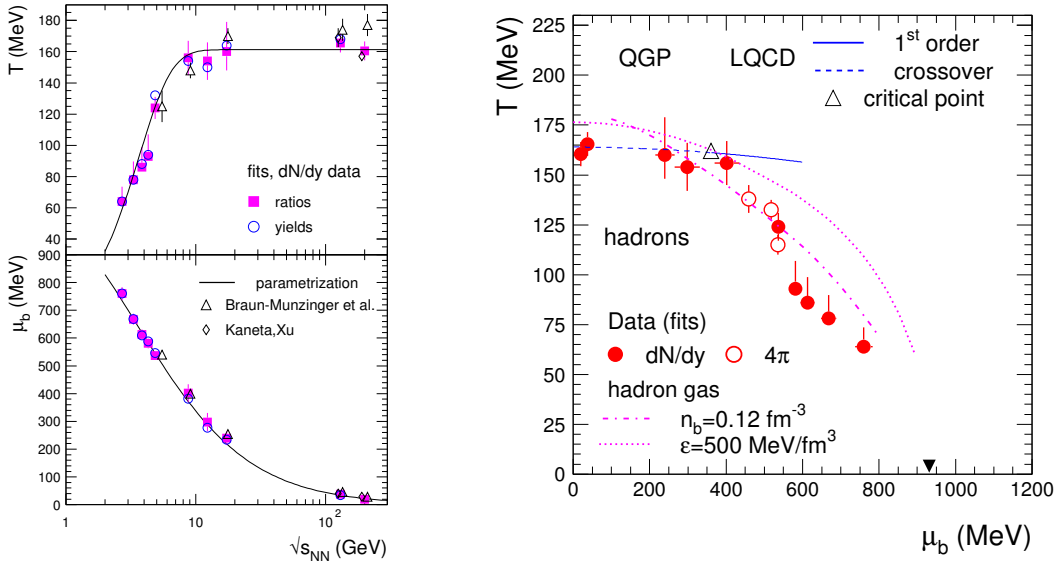

Fig. 1.7 **Left:** Energy dependence of the thermal parameters i.e. chemical freeze-out temperature T and chemical potential μ_B. The solid line corresponds to the parameterization of T and μ_B. **Right:** The phase diagram of QCD matter in $T-\mu_B$ plane. The LQCD results (for different EOS) along with the experimental freeze-out values are shown [51]. The predicted QCD critical point is shown by the open triangle. The freeze-out lines calculated for hadron gas at constant energy density ($\varepsilon = 500\text{MeV}/\text{fm}^3$) and constant baryon density ($n_b = 0.12\text{fm}^{-3}$) are also shown.

with hydrodynamic model calculation, one can constraints the hydrodynamic models. Thus, a study of transverse momentum distribution and its comparison with the model calculation provides a better insight into the dynamics of the fireball. Mean transverse momentum $\langle p_T \rangle$ or transverse mass $\langle m_T \rangle$ which is a measure of temperature at kinetic freeze-out is believed to be a promising tool to study the QCD phase transition. It has been predicted that the excitation function of mean transverse momentum will show a plateau if there is a 1st order phase transition [53]. The flattening is because of the fact that at the coexistence of a hadron gas and QGP phase (i.e. at the mixed phase) temperature of the system stays constant [53].

Strangeness enhancement

Strangeness enhancement was predicted by Rafelski and Müller [54, 55] as one of the crucial signatures of QGP. They showed that, in the QGP phase, the strange quarks can either be produced via (i) $q+\bar{q} \rightarrow s\bar{s}$ or (ii) $gg \rightarrow s\bar{s}$ channels. The threshold energy required for $s\bar{s}$ production is just the sum of the mass of two strange quarks. In QGP, due to the restoration of

chiral symmetry, the mass of strange quarks are reduced to their bare masses. Thus in a QGP phase, the threshold energy required to produce a strange anti-strange quark pair is something around $2m_s \approx 200$ MeV. On the contrary, in a hadronic scenario, due to the strangeness conservation (in strong interaction), strangeness is produced via associated channels and threshold energy required for that is very very large in comparison to QGP scenario (shown below).

- $N + N \rightarrow N + \Lambda + K$ Q = 670 MeV
- $N + \pi \rightarrow \Lambda + K$ Q = 500 MeV

It is therefore energetically easier to produce strange hadrons in a QGP phase than the hadronic scenario. Thus, if at all QGP is created, the copiously produced strange and anti-strange quarks along with u and d quarks after hadronization (see Fig. 1.8) might lead to an enhanced production of strange particles as compared to a scenario where no QGP is formed. Strangeness enhancement is therefore recognized as an important signature of the formation of QGP.

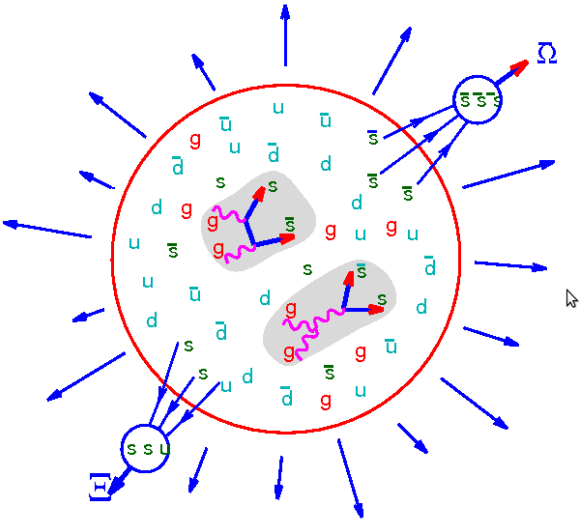

Fig. 1.8 A cartoon showing the production of multi-strange hadrons from a soup of quarks and gluons [56].

In experiments, the strangeness enhancement is quantified by the ratio of the normalized yield of a strange particle in nucleus-nucleus collisions and the respective normalized yield in elementary pp collisions. The enhancement of different strange particles was indeed observed in WA97 and NA57 experiment at SPS. They measured the enhancement with respect to p+Be collisions. In those experiments, the enhancement pattern follows a clear

hierarchical order. The value of enhancement for Λ (S = -1) is around 3-4, while the value reaches to around 10 for Ξ^- (S = -2), and for Ω (S = -3), the enhancement as high as 30 has been observed (see Fig. 1.9). Further, other heavy-ion experiments like STAR at RHIC and ALICE at LHC have also measured the strangeness enhancement. Although a similar hierarchical enhancement pattern is observed both at STAR and ALICE, the overall enhancement is found to be decreasing with increasing energy. The above two features of enhancement pattern (i.e. the hierarchical strangeness enhancement ordering and energy dependence of enhancement) are in agreement with the competing hadronic scenario called canonical suppression. According to the canonical suppression scenario, due to lack of phase space, in a small system like pp collision, the production of strange quarks are suppressed. The magnitude of this suppression increases with the strangeness content of the hadrons. Further, in this canonical suppression model, the enhancement is predicted to be more at lower energies. Considering the above facts, the observed strangeness enhancement as measured by several heavy-ion experiments might not be conclusively associated with the formation of a partonic medium.

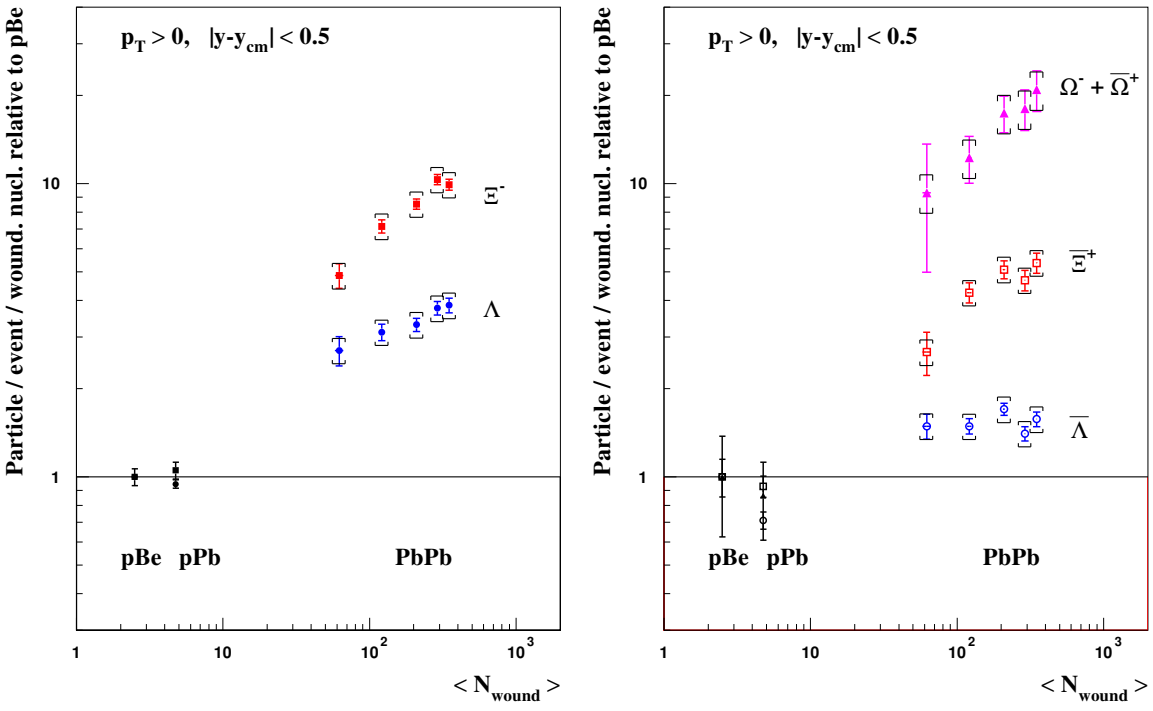

Fig. 1.9 Centrality-dependent enhancement of multi-strange hyperons in heavy-ion collisions at SPS (NA57 collaboration) [57].

However, ϕ meson, consisting of strange and anti-strange quarks will not be suppressed canonically even in a small system like pp collision. STAR collaboration measured the centrality-dependent enhancement of ϕ meson at $\sqrt{s}$ = 62.4 GeV and $\sqrt{s}$ = 200 GeV (see

Fig. 1.10) and found the enhancement to be greater for larger $\sqrt{s}$. Also, ϕ mesons violate the strange quark ordering as expected in the canonical picture for the production of other strange hadrons [58]. It is therefore concluded from the study of ϕ mesons that the production of QGP could be the main reason for the enhancement of all the strange hadrons in Au+Au collisions at RHIC. It might be interesting to verify the enhancement pattern of ϕ meson at low energies e.g. at the FAIR energy domain (i.e. E_{lab} = 10A to 40A GeV).

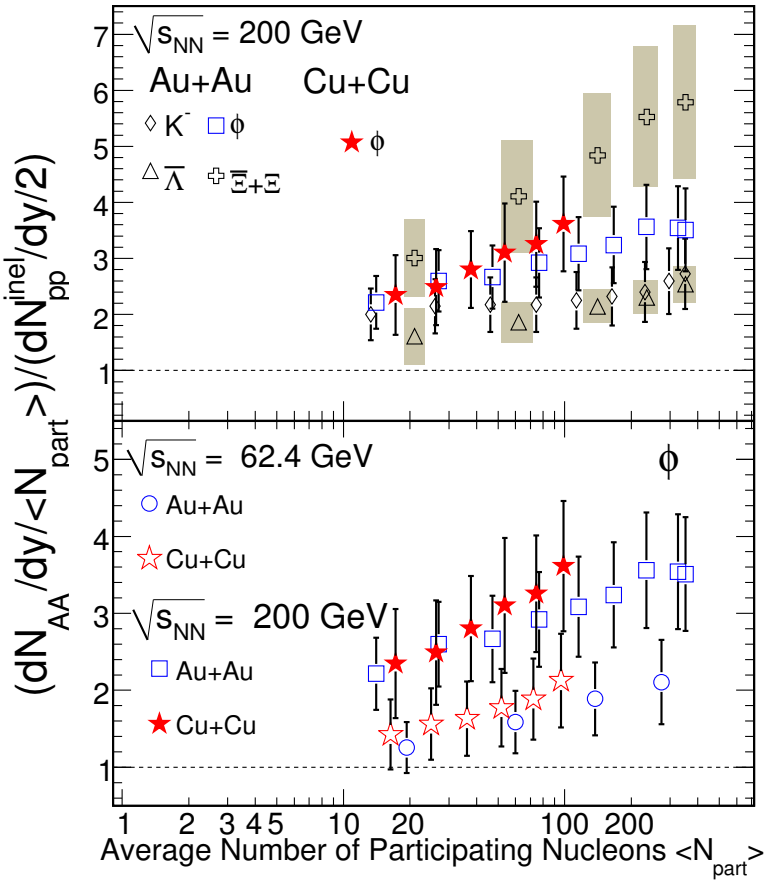

Fig. 1.10 Enhancement of ϕ mesons along with other particles (K^- , Λ, Ξ) with respect to pp collisions [58, 59].

Collective flow

The collective expansion of the constituents of the fireball, produced in heavy-ion collisions, due to the pressure gradient, is known as collective flow. If the initial shape of the fireball is anisotropic, this pressure gradient might lead to an anisotropic expansion of the fireball. The spatial anisotropy of the created fireball can cause an anisotropy in momentum space

(see Fig. 1.11). The azimuthal distribution of the produced particles can be decomposed following the Fourier expansion [60],

$$\frac{dN}{d\phi} = 1 + 2\sum v_n \cos\left[n(\phi - \psi_R)\right], \tag{1.6}$$

where, ϕ and ψ_R respectively denotes the azimuthal angle and the orientation of the reaction plane. Reaction plane is defined as the plane spanned by the beam direction and impact parameter vector. From equation 1.6, the co-efficient v_n can be written as,

$$v_n = \langle \cos n(\phi - \psi_R) \rangle, \tag{1.7}$$

where, the angular bracket $\langle ... \rangle$ denotes average over particles in all events. The co-efficients v_1 , v_2 , and v_3 are respectively known as direct, elliptic and triangular flow.

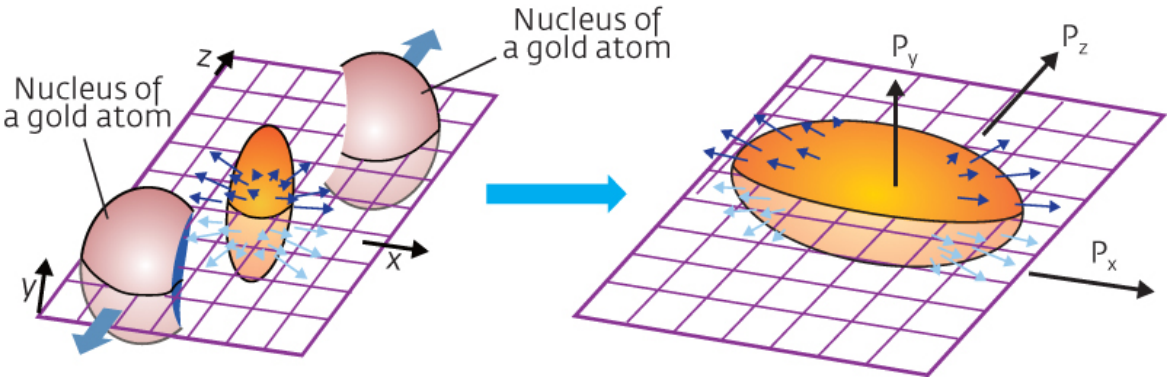

Fig. 1.11 A graphical illustration showing how spatial anisotropy results momentum anisotropy in semi-central heavy-ion collision.

Among all the other harmonics, v_2 is believed to provide vital information regarding the formation of hot and dense medium created in high energy heavy-ion collision. The elliptic flow is regarded as a relevant observable for the studies of EOS (equation of state) [61–64]. Further, hydrodynamic calculations also predicted the elliptic flow parameter to be highly sensitive to the EOS [65]. The EOS is a relation which tells how the pressure (or alternatively the energy per particle) depends on the density or temperature and is of fundamental interest in heavy-ion physics. Moreover, since the magnitude of elliptic flow is proportional to the asymmetry of the created matter, it provides very significant information about the early stage of the collision. The elliptic flow, therefore, might shed some light on the fundamental degrees of freedom of the created matter.

1.5.2 Hard probes

J/ψ suppression

J/ψ, also known as charmonium, is a particle consisting of c and $\bar{c}$. The suppression of charmonium or J/ψ was predicted by Matsui and Satz [66] in 1986. It is considered to be one of the unambiguous signatures of the formation of Quark-Gluon Plasma (QGP). In vacuum (i.e. in the absence of QGP), the attractive potential between the charm and anti-charm quark in a charmonium can be expressed as,

$$V(r) = kr - \frac{\alpha_s}{r}. \tag{1.8}$$

In presence of the deconfined phase i.e. QGP, the string tension between c and $\bar{c}$ will disappear i.e. the confinement term (1st term) in the above equation vanishes. In that scenario, c and $\bar{c}$ still remain interacting with each other by Coulomb-type color interaction known as Yukawa interaction. The Coulomb potential has, in vacuum, the form e^2/r and in presence of many other charges, a situation that might arise if a QGP is formed, it becomes subject to Debye screening and we obtain the form $e^2\frac{e^{-r/\lambda_D}}{r}$ with λ_D, the Debye screening radius inversely proportional to the overall charge density of the system. Thus, in presence of QGP, the potential between c and $\bar{c}$ quark is modified and Eqn. 1.8 becomes,

$$V(r) = -\frac{\alpha_s e^{-r/\lambda_D}}{r}. \tag{1.9}$$

It is to be noted that, within the distance λ_D, this attractive interaction is effective and beyond λ_D, the magnitude of interaction decreases exponentially and thus negligible. The modification of 2nd term arises because of the influence of other surrounding light quarks, anti-quarks and gluons and might screen the color charge of charm and anti-charm quarks. The effect is known as Debye-color screening (see Fig. 1.12).

The Debye screening length is temperature dependent. In the lowest order perturbative QCD (pQCD) calculations, the Debye screening length (λ_D) in terms of temperature (T) of the medium can be written as [67],

$$\lambda_D(T) = \sqrt{\frac{2}{9\pi\alpha_s}}\frac{1}{T}. \tag{1.10}$$

Thus, with increasing temperature of the medium, the effective range of interaction i.e. the Debye screening length decreases. With increasing temperature of the medium, the quark-gluon density surrounding the charm and anti-charm quark increases, which basically diminished the c and $\bar{c}$ interaction. Thus, if the Debye screening length becomes smaller than

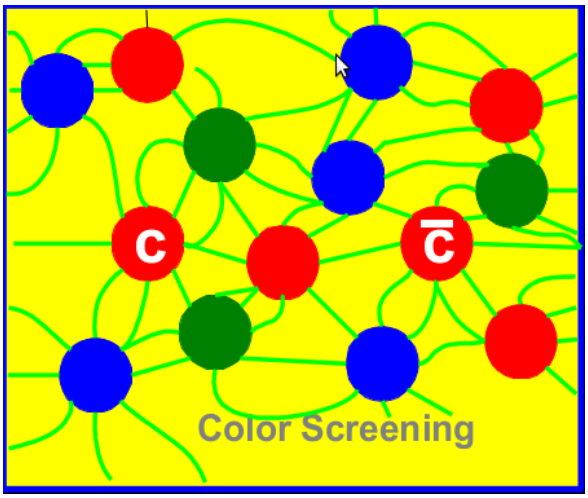

Fig. 1.12 A schematic view of color screening occurring at high baryonic density environment.

the binding radius of J/ψ, the $c\bar{c}$ system dissociates into a separate charm and anti-charm quark. This is known as the so-called J/ψ suppression. Matsui and Satz [66], in their seminal paper, showed that, in presence of QGP, the Debye screening radius become smaller than the radius of J/ψ, leading to dissociation of J/ψ bound states. It is to be noted that the binding radius of different quarkonium states e.g. ψ', ψ'' are different. Thus, the suppression of different quarkonium states occurs at different temperatures. Hence, the suppression of different quarkonium states can be used as an indicator of the temperature (thermometer) of the plasma.

On the other hand, there are some competing hadronic processes which might also lead to the suppression of charmonium: (i) Shadowing of the parton distribution function (PDF) [68, 69] and (ii) Comover effect [70–72, 17]. Nuclear shadowing effect refers to the modification of initial state parton distribution function due to the presence of nucleons, which might reduce the production cross-section of $c\bar{c}$ pair. Moreover, by virtue of the inelastic collisions of the produced $c\bar{c}$ pair during its evolution along with the hadronic comovers e.g. π, ρ and ω might also lead to the dissociation of $c\bar{c}$ pair.

Although in a QGP scenario, charmonium suppression occurs due to the reasons stated above, at the same time, the dissociated charm and anti-charm quarks, might combine with other light quarks to produce D-mesons. Hence, the production of D-mesons might be large if QGP is produced in high-energy heavy-ion collisions.

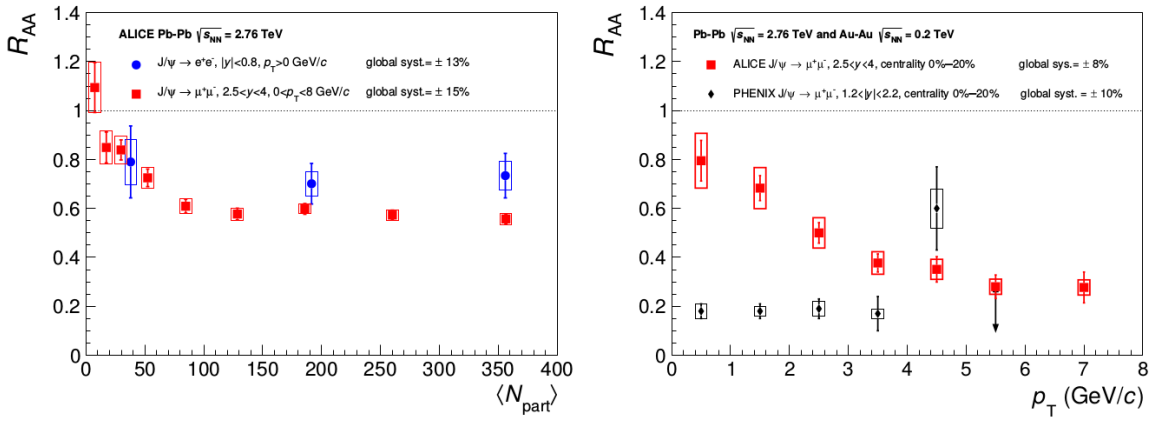

Fig. 1.13 **Left:** p_T integrated J/ψ R_{AA} as a function of centrality ($\langle N_{part} \rangle$) both from the dielectron ($|y| < 0.8$) and dimuon ($2.5 < y < 4$) channels by ALICE experiment. **Right:** p_T dependent J/ψ R_{AA} measured by both ALICE and PHENIX experiment from the dimuon channel at $\sqrt{s}$ = 2.76 and 0.2 TeV respectively [73].

Experimentally, J/ψ suppression was first observed by the experiments at SPS [74][12]. Consequently, at RHIC and recently at LHC energy as well a suppression of J/ψ has been observed. The inclusive R_{AA} of J/ψ was measured both by the PHENIX experiment at RHIC and ALICE experiment at LHC [73]. The left panel of Fig. 1.13 shows the p_T integrated centrality-dependent R_{AA} measurement of J/ψ both from the dielectron ($|y| < 0.8$) and dimuon ($2.5 < y < 4$) channels by ALICE experiment [73]. It is clearly observed from the figure that both at the central and forward rapidity, the value of R_{AA} is less than unity, indicating a suppression. The right panel of Fig. 1.13, on the other hand, depicted the p_T-dependent R_{AA} of J/ψ as measured by ALICE experiment from the dimuon channel at $\sqrt{s}$ = 2.76 TeV and its low energy values as obtained by PHENIX experiment at RHIC [73]. Although at both the energies, a suppression of J/ψ has been observed, at intermediate transverse momentum, J/ψ is less suppressed at higher energies. This observation can be interpreted as the result of regeneration of J/ψ in the environment where copiously produced c and $\bar{c}$ quarks may coalesce to form J/ψ again [73].

Jet quenching

The life-time of QGP is of the order of 10^{-23}s. It is, therefore, impossible to characterize the QGP phase with the help of any external probe. Instead, hard partons, produced at the very early stage of the collision, could be used as an internal probe to characterize the hot and dense medium produced in the high-energy heavy-ion collision. In high-energy collisions,

[12] Although the observed suppression at SPS are believed to be caused by the non-QGP sources as discussed above

gluons from the target and projectile may interact and produce two highly energetic (with large transverse momenta) gluons which might travel in the opposite direction [75]. These gluons after hadronization might emerge as jets of particles[13] [75]. During its passage through the medium, the jets interact with the medium and lose energy and might be quenched. The magnitude of energy loss depends upon the path length the jet travels inside the medium. A schematic diagram of the back-to-back jets produced in both p-p and nucleus-nucleus collisions are depicted in Fig. 1.14. Due to the production of a hot and dense medium in the nucleus-nucleus collision, one of the jets is getting quenched owing to passage through a large distance through the medium (right panel of Fig. 1.14). Thus by measuring jets in nucleus-nucleus collisions and comparing it with pp collisions, one can distinguish between the hadronic and partonic medium created in high-energy heavy-ion collisions.

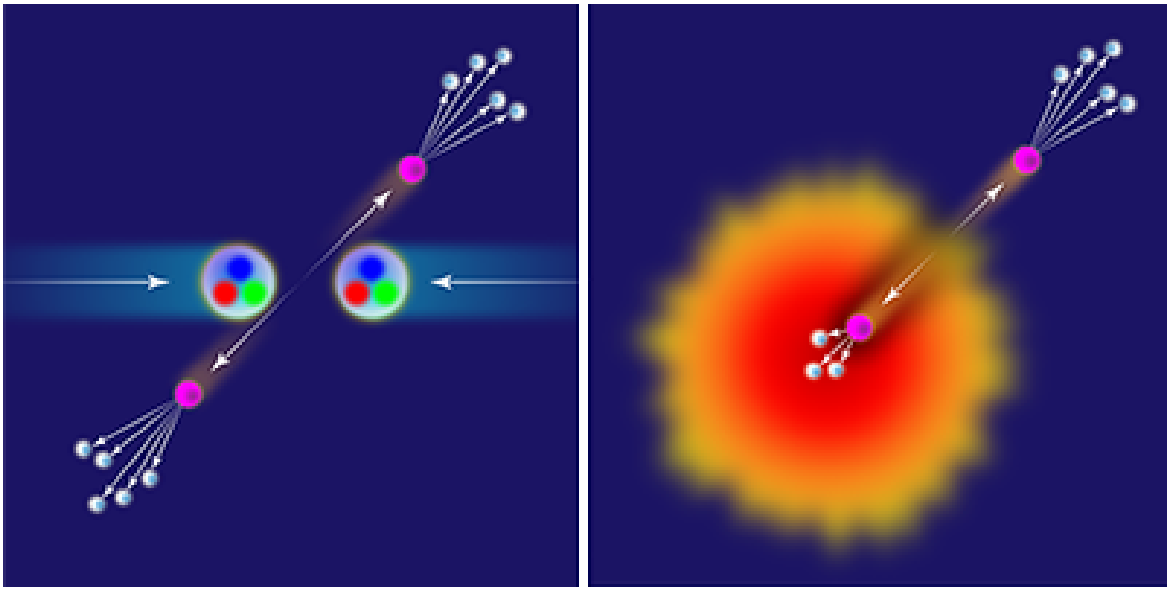

Fig. 1.14 The schematic representation of di-jet moving in the opposite direction *(Left)* for pp collision and *(Right)* for heavy-ion collisions showing jet quenching [76].

1.5.3 Electromagnetic probes

Photons and dileptons are regarded as the electromagnetic probes. They are believed to be the cleanest and most efficient tool to characterize the first few instances of heavy-ion collisions. Unlike hadrons, which are emitted from the freeze-out surface after undergoing intense re-scatterings, photons come out from each and every phases of the expanding fireball [77, 78]. Both photons and dileptons participate only in electromagnetic interaction and thus

[13] A jet is the collimated set of hadronic decay products of a parent parton.

comes out of the fireball almost without suffering any interaction and thus brings undistorted information of the interior of the fireball. Photons emitted from heavy ion collisions are broadly classified into two categories – direct and decay photons. In general, 90% of the photons detected by the detector in experiments are the decay photons. Direct photons on the other hand can be subdivided into the following categories – (a) prompt photons (created in hard parton-parton scattering); (b) pre-equilibrium photons; (c) thermal photons (from both QGP and hadronic phase); and (d) jet conversion photons.

Along with photons, dileptons are also produced in every stage of the evolution of heavy-ion collisions. Dileptons are considered as the most reliable messengers of the in-medium modification of vector mesons [77]. A detailed description of the dileptons is provided in Chapter 2.

1.6 Exploring superdense matter in laboratory

The observation made by the experiments at Relativistic Heavy Ion Collider (RHIC) have suggested the formation of partonic matter in Au+Au collision at $\sqrt{s} = 200$ GeV [79]. In the same spirit, few other experiments at the Large Hadron Collider (LHC) facility have also started taking data in order to investigate QCD phase diagram at the regime of high temperature and almost zero net-baryon density. As already discussed, at zero baryon chemical potential, LQCD predicted a smooth crossover from hadronic to partonic matter [45]. On the other hand, a first-order phase transition is predicted by LQCD at large net-baryon density [45]. Thus at the low energy regime, one would expect a critical point. The experimental discovery of these prominent landmarks of the QCD phase diagram would be a major breakthrough in our understanding of the properties of nuclear matter [45]. The experimental findings at CERN-SPS: the “hron" like structure in the excitation function of K/π ratio and “step" or plateau observed in the excitation function of inverse slope parameter triggered a healthy debate regarding the onset of deconfinement at lower SPS energies. In view of this fact, in order to explore the high density region of the QCD phase diagram, several experiments are planned world wide. The STAR and the PHENIX experiment at RHIC, BNL have already conducted beam energy scan (BES) program in order to locate the QCD critical point. Similarly, NA61-SHINE experiment at CERN-SPS with the up-gradation of the NA49 detectors has also started investigations at the similar beam energies. Further, NICA experiment at JINR will also investigate the superdense region of the QCD phase diagram. All these experiments due to the luminosity/intensity limitations can only study the bulk observables. In contrast, the proposed CBM experiment at FAIR is focused on the measurement of rare probes of the fireball.

1.7 The Facility for Antiproton and Ion Research

The planned Facility for Antiproton and Ion Research (FAIR) will be a unique international particle accelerator facility that will provide research opportunities in diverse fields of physics viz. nuclear, hadron, atomic and plasma physics [80, 81]. The facility will accelerate varieties nuclei right from Proton to Uranium with beam energies ranging from 2 – 45A GeV. This facility is unique in the sense that it will provide beams with unprecedented beam intensity[14] with brilliant beam quality[15] [82]. In this new facility a set of four beamlines will be operational with the objective of using: (i) radioactive ion beams for nuclear physics; (ii) exploring novel phenomena in hadron physics using antiprotons; (iii) laser and plasma physics, and (iv) physics of strongly interacting matter at extreme density [82]. Accordingly four scientific collaborations, comprising of nearly 3000 researchers from 53 countries were formed viz. APPA: Atomic, Plasma Physics and Applications [83]; PANDA: anti-Proton ANnihilation at DArmstadt [84, 85]; NUSTAR: NUclear STructure, Astrophysics and Reactions [86]; and CBM: Compressed Baryonic Matter experiment [31–35].

Fig. 1.15 illustrates the schematic layout of both the existing and the planned FAIR accelerator facility. The existing facility (shown by blue lines) comprises of the two GSI accelerators: UNILAC and SIS-18 will serve as injectors for the new facility [88]. The new FAIR facility will be comprising of (i) a proton-LINAC in order to inject high-intensity proton beam to the main rings; (ii) double rings (having circumference 1.1 km) with rigidities 100 and 300 Tm known as SIS-100 and SIS-300 respectively housed in the same tunnel; and (iii) superconducting fragment separator (Super-FRS).

1.8 The CBM research program

The Compressed Baryonic Matter (CBM) experiment is one of the four experiments to be performed at FAIR accelerator facility at Darmstadt, Germany. The proposed CBM experiment at FAIR is designed in order to explore the QCD phase diagram in the region of high baryon densities but moderate temperature [31–35], a condition that is believed to be analogous to the situation at the heart of neutron star[16]. Along with bulk particles, the main thrust of CBM experiment is the detection of the messengers of the fireball created at the early stages of the heavy-ion collisions. These are the particles with very low production

[14] three order magnitude higher than any other existing accelerator facility.

[15] beam quality in general is quantified in terms of their energy spread and emittance.

[16] Neutron star is a celestial object of typical radius $\sim$ 11km and typical mass about twice solar mass with core density of the order of 10^{16} - 10^{17} gm.cm^{-3}

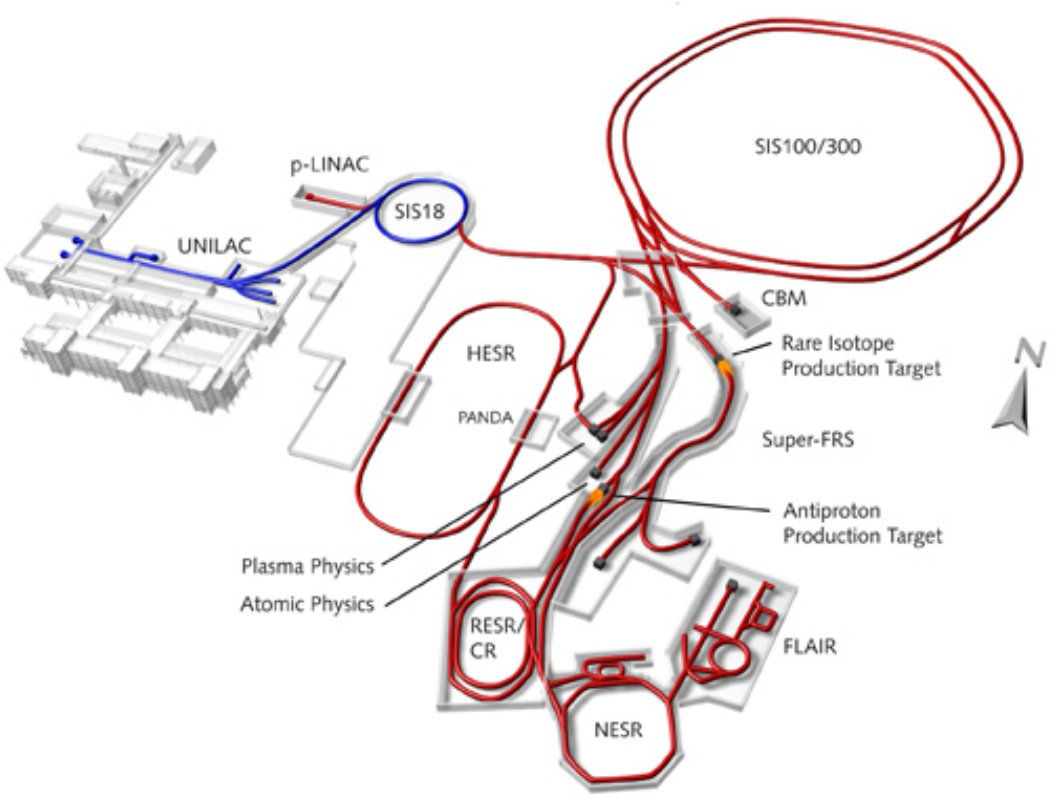

Fig. 1.15 The schematic layout of existing and planned FAIR accelerator facility [87].

cross-section, also known as *rare probes* such as ψ', J/ψ, $\bar{D}^0$, D^0, $D^{\pm}$ etc. Fig. 1.16 shows the production probability (multiplicity $\times$ branching ratio) of both bulk and rare particles in central Au+Au collisions at 25A GeV using HSD [89–91] and statistical models [44]. In order to measure these rare probes, the CBM experiment will be run under extreme reaction rate. For some observables, there will be a dedicated run with intensity up to 10 MHz. To work efficiently under such an unprecedented reaction rate, it requires developing ultra-fast and extreme radiation hard detectors and electronics. A list of few physics observables for the CBM experiment is presented in Table 1.3.

1.8.1 CBM detector system

The aim of CBM experiment is to detect both hadrons and leptons and extract the rare probes at the reaction rate of the order of 10MHz [92]. The detectors thus need to be both fast and radiation hard in order to work efficiently. The CBM detector system consists of various sub-detectors: Micro Vertex Detector (MVD), Silicon Tracking System (STS), Muon Chamber (MUCH), Ring Imaging Cerencove Detector (RICH), Time of Flight (TOF),

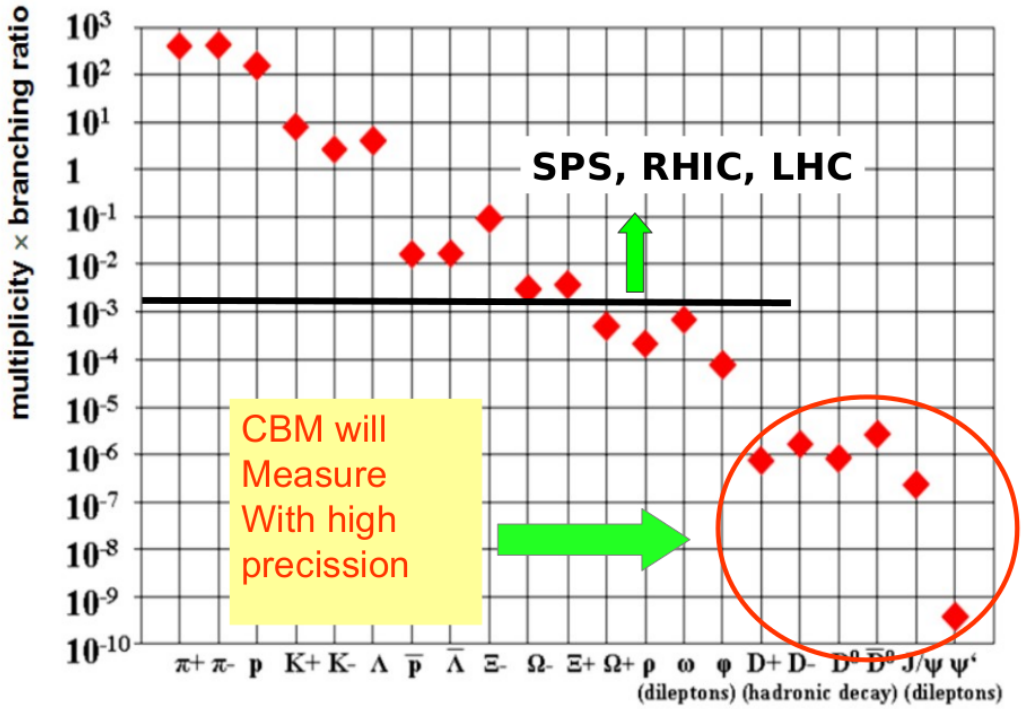

Fig. 1.16 Production probability (multiplicity × branching ratio) of various particles for central Au+Au collisions at 25A GeV using HSD [89–91] and statistical model [44]. Dileptonic channel has been assumed for the vector mesons whereas, for D-meson, hadronic decay into pions and kaons has been assumed.

Transition radiation detector (TRD), Electromagnetic Calorimeter (ECAL), and Projectile Spectator Detector (PSD) [45].

Micro Vertex Detector (MVD)

The Micro Vertex Detector (MVD) is responsible for the high precision measurement of the displaced or secondary vertex in the measurement of D-mesons (open charm). The MVD is based on highly-granulated Monolithic Active silicon Pixel Sensors (MAPS) technology. For the obvious reason, MVD lies very close to the target [45].

Silicon Tracking System (STS)

Silicon Tracking System (STS), situated within the superconducting dipole magnet, is the heart of the CBM experiment and is required for the measurement of almost all the proposed observables. STS, consisted of microstrip and hybrid pixel detectors, can be used to reconstruct particle tracks having momentum ranging from 100 MeV to around 10 GeV with a momentum resolution $\triangle P/P \sim 1\%$ [93, 45].

Physics case	Observables
EOS at high baryon density	Excitation function of collective flow of hyperons
	Excitation function of yield of multi-strange hadrons
In-medium modification	Invariant mass distribution of vector mesons decaying into the dipelton channels
	yield and transverse mass distribution of charmed mesons for different beam energies
Phase transition from hadronic to partonic matter at high baryon densities	The excitation function of yields, spectra, and collective flow of strange particles, charmed particles and lepton pairs in heavy-ion collisions from 6 - 45 AGeV (SIS100/300)
	Event-by-event fluctuations of conserved quantities from 6 - 45 AGeV (SIS100/300)
Charm production mechanisms, charm propagation, and their in-medium properties in (dense) nuclear matter	Cross sections, momentum spectra and collective flow of open charm (D-mesons) and J/ψ at SIS100/300 energies.
	J/ψ suppression

Table 1.3 A list of few physics observables of the CBM experiment [45].

Muon Chamber (MUCH)

Muon measurement is one of the prime objectives of the CBM experiment. Muon Chamber (MUCH) will be the detector responsible for the detection of J/ψ decayed muons. It consists of segmented hadron absorber and detector layers based on the state-of-the-art detector technology known as GEM (Gas Electron Multiplier) [94, 45]. A brief description on MUCH detector is provided in Chapter 2.

Ring Imaging Cerencove Detector (RICH) and Transition radiation detector (TRD)

Both the Ring Imaging Cerencove Detector (RICH) and Transition Radiation Detector (TRD) will be used for the identification of electrons (and positrons). The RICH detector is capable of measuring the high-momentum electrons ($\sim$ 10 GeV/c) while low momentum electrons beyond 1.5 GeV/c can be measured with the help of TRD detector. Apart from electron identification TRD can also be used for particle tracking and thus helps to suppress the background for the detection several observables like charged particles (π, k, p), hyperons, open charm [45].

Time-Of-Flight (TOF)

In the present design, being located 10 m downstream of the target and covering an active area of about 130 m^2, the Time-Of-Flight (TOF) detector will be responsible for the identification of charged hadrons (π, k, p). Resistive Plate Chamber (RPC) will be used to measure the time-of-flight with a time resolution about 80 ps [45].

Electromagnetic Calorimeter (ECAL)

To measure direct photons and photons emitted from the decay of neutral mesons (π^0, η^0) Electromagnetic Calorimeter (ECAL) will be used. For CBM experiment, “shashlik" type calorimeter as used for LHC-b, PHENIX and HERA-B will be used [45].

Projectile Spectator Detector (PSD)

The information regarding the centrality class is the most important task to extract any physics information out of the measured experimental observable. By measuring the number of non-interacting nucleons, from the projectile in A+A collision, one can measure the centrality. PSD is nothing but a lead-calorimeter consisting of 12×9 individual modules, each consisting of 60 lead/scintillator layers with a surface of 10×10 cm^2 [45].

A schematic layout of the CBM experiment with all the individual sub-detectors is illustrated in Fig. 1.17. Various sub-detectors needed for the measurement of different observables are also presented in Table 1.4.

Observables	MVD	STS	MUCH	RICH	TRD	TOF	ECAL	PSD
π, k, P		$\surd$		($\surd$)	($\surd$)	$\surd$		$\surd$
Hyperons		$\surd$			($\surd$)	($\surd$)		$\surd$
Open charm	$\surd$	$\surd$		($\surd$)	($\surd$)	($\surd$)		$\surd$
Electrons	$\surd$	$\surd$		$\surd$	$\surd$	$\surd$		$\surd$
Muons		$\surd$	$\surd$			($\surd$)		$\surd$
Photons							$\surd$	$\surd$

Table 1.4 CBM physics observables along with the required set of detectors for their measurement. For example, in order to identify π, k, P, the required set of detectors are STS, RICH, TRD, and TOF. It is to be noted here that, PSD detector is required for the centrality measurement [45].

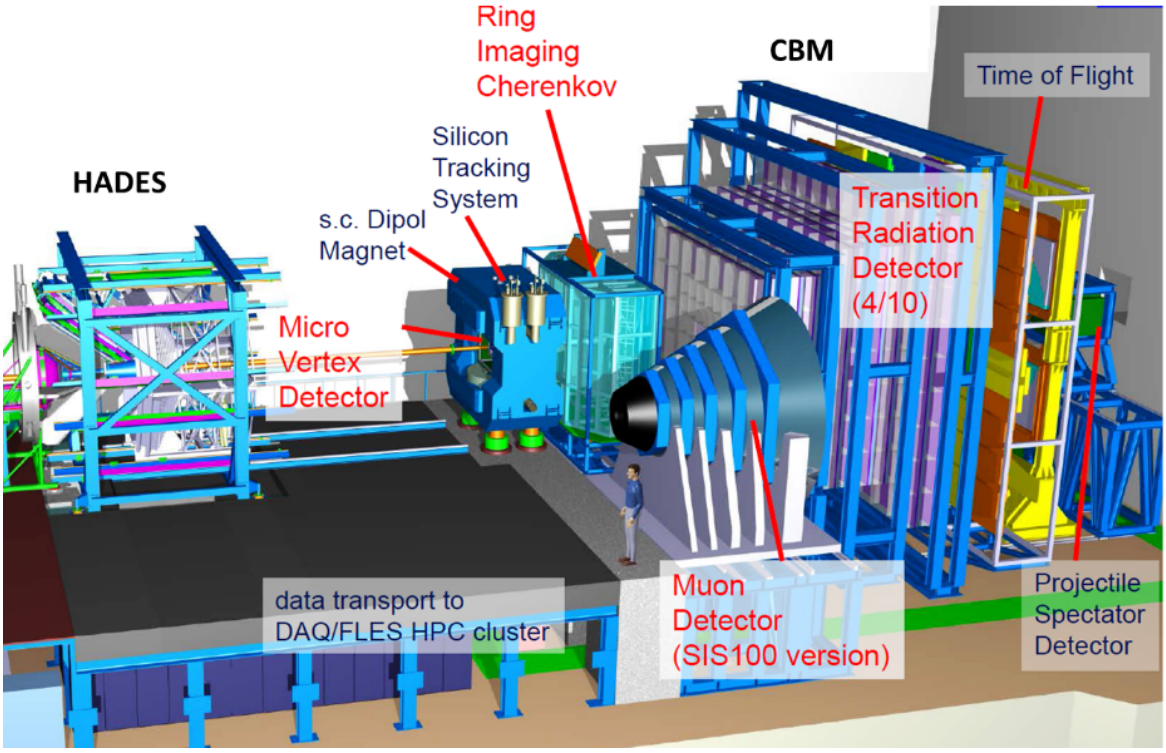

Fig. 1.17 A complete schematic layout of the CBM experiment at FAIR [95].

1.9 Goal of the thesis

The idea of asymptotic freedom of strong interaction led the physicist to believe that under the condition of extreme temperature and/or net-baryon density, hadrons might melt into its constituents i.e. quarks and gluons and produces a new state of matter known as Quark-Gluon Plasma (QGP). Relativistic heavy-ion collisions are the only way to create QGP in the laboratory. Several heavy-ion experiments have already been conducted to create and characterize this new state of matter. The proposed Compressed Baryonic Matter (CBM) experiment at FAIR is designed to study the phase diagram of strongly interacting matter in the region of moderate temperature and high net-baryon density. The uniqueness of the CBM experiment lies on its enormous beam intensity or reaction rate and high baryon density. This humongous interaction rate will make it possible to study the rare probes of the fireball with a considerable amount of statistics. The CBM experiment thus believed to have a unique discovery potential [45]. In order to obtain a complete picture, a comprehensive set of observables will be measured in pp, pA, and AA collisions over wide range of beam energies i.e. E_{lab} = 2–45A GeV [45]. A list of the physics observables of the CBM experiment is provided in Table 1.3. The civil construction works of FAIR are in full progress at GSI, Darmstadt, Germany and first set of data will be collected in the year 2022. At this stage, it is

therefore extremely essential to carry out simulation studies of various detectors' performance and also the feasibility study of various physics observables of CBM experiment, one of the four proposed major experiments of FAIR. Keeping these things in mind the present investigation has been undertaken, the aim of which can broadly be divided into two parts:

(i) Simulation of MUCH detector for optimization of J/ψ reconstruction and to estimate the temperature of the fireball to be created in CBM experiment.

(ii) Prediction of physics observables of proposed CBM experiment with model generated data.

- As mentioned above (section 1.8 of chapter 1), one of the key observables of the CBM experiment is the measurement of charmonia via their decay into dilepton channels. However, the multiplicity of charmonium is extremely low at FAIR energies which therefore requires extreme interaction rates (up to 10^7 collisions per second) to have reasonably good statistics. Thus, one of the major challenges of CBM experiment is to identify the primary muons coming out from the decay of J/ψ or low mass vector mesons in an environment of high background mostly due to electrons and hadrons. The idea is to track the particles through hadron absorber and detector systems and to perform a momentum dependent muon identification. This concept would be realized by building a muon chamber (MUCH) detector where the hadron absorber will be segmented into several layers and placing triplets of tracking detectors planes in the gaps between the absorber layers. Simulation is an important aspect for the proper functioning of MUCH. Thus, in the first part our investigation (in Chapter 2) an effort will be made to optimize a few parameters of the proposed muon chamber (MUCH) of the FAIR-CBM experiment.

  As discussed in section 1.8, the main aim of Muon Chamber (MUCH) of the CBM experiment is to measure the dimuons ($\mu^+\mu^-$) coming from the decay of both charmonium and low mass vector mesons. Leptons do not participate in the strong interaction and therefore believed to carry the undistorted signal or the cleanest information about the interior of the fireball. Thus, the measurement of the temperature from the dilepton transverse mass spectra might be associated with the early stage temperature of the fireball itself. Hence, in Chapter 3 an attempt will be made to study the feasibility of measuring the fireball temperature using the optimized muon chamber (MUCH) detector.

- The CBM experiment at FAIR is expected to address a few unanswered questions related to the strongly interacting matter at high baryon density. The beam energies for

heavy-ion collisions at FAIR are chosen in such a way that the created matter possesses the highest net-baryon density something of the order of 5-10 times the normal nuclear matter density. Under high baryon density environment, various dynamical properties are expected to modify. As a result, effects which couple with baryon density would be very prominent at FAIR energies. In heavy-ion collisions, the pattern of variation of net-baryon density is observed to be a function of beam energy. For example, at lower beam energies (SIS18/AGS), due to baryon number transfer from beam rapidity to central rapidity region, the variation of net-baryon density with rapidity is found to be of Gaussian shape with its peak at mid-rapidity. Similarly at the highest beam energies (LHC), due to 'nuclear transparency', net-baryon density at mid-rapidity is almost found to be close to zero. It is further believed that the rapidity distribution of a particle, the production of which is sensitive to net-baryon density might tend to follow the net-baryon density. Thus, a study on the width of the rapidity distribution and its evolution with beam rapidity might believe to have considerable significance at FAIR energies. An attempt will, therefore, be made in Chapter 4 to study in details the width of the rapidity distribution of the produced particles as a function of beam-rapidity.

Strangeness is a conserved quantity in strong interaction. This implies (strange)pair-creation in high energies and associated strangeness production in relatively lower energies. A hadronic transport model like UrQMD (Ultra Relativistic Quantum Molecular Dynamics) suggested an uneven distribution of strangeness in rapidity space leading to the local violation of strangeness conservation. The study of rapidity dependent strangeness enhancement is therefore believed to have a considerable significance and would be carried out with UrQMD generated $Au+Au$ events at 30A GeV. Moreover, because of the limited detector acceptance, the measurement of strangeness enhancement with the past and ongoing heavy-ion experiment was limited to the mid-rapidity only. But CBM experiment will have the capability of detecting the strange particles in a wide rapidity range due to the large detector acceptance. Therefore, in the present investigation (in Chapter 5), UrQMD generated data will be used to measure the rapidity dependent strangeness enhancement of the produced strange particles at FAIR energies.

2

Simulation of Proposed Muon Chamber of FAIR-CBM Experiment

High energy nuclear and particle physics experiments are generally aimed to achieve a number of physics goal and are pretty expensive in nature due to their complexity in design. Such a complex experiment generally consists of several subsystems and sub-detectors. The goal of such an experiment may not be achieved if the design and performance of the subsystems and sub-detectors are not perfect. It is therefore extremely essential that detailed simulation studies on design and performance are conducted using proper simulation tools for individual detector systems. In this chapter, an attempt has therefore been made to simulate and optimize the Muon Detection system (MUCH) for detecting J/ψ from its decay into dilepton channel ($\mu^+\mu^-$) for the FAIR-CBM experiment.

2.1 Introduction

One of the prime objectives of CBM experiment [31–35] is to study the notion of Quark Gluon Plasma (QGP) by measuring the J/ψ suppression which was suggested to be a smoking gun signature of QGP [66]. J/ψ, popularly known as charmonium, is a vector meson and is the bound state of charm (c) and anti-charm ($\bar{c}$) quark. The rest mass of J/ψ is

3.0969 GeV/c^2 [96] with life-time of the order of 7.2×10^{-21} s [96]. At relativistic energy, if we assume that J/ψ is moving with the velocity of light, after its production it can move only up to a distance of $d = c\tau = 0.2$ A before decay. Thus, the direct detection of J/ψ is impossible. The only way out is to detect the J/ψ from its decay products. J/ψ can decay either to hadrons or di-leptons ($\mu^+\mu^-$ or e^+e^-). In heavy-ion collision environment, the leptonic channels are believed to be the cleanest and thus, CBM experiment aims to detect J/ψ from the leptonic channels i.e. $\mu^+\mu^-$ and/or e^+e^-. CBM-India group has proposed the MUon CHamber (MUCH) detector [97] for the detection of J/ψ from the dimuon channel. The idea is to allow the J/ψ decayed muons, along with other produced particles, to pass through a number of absorbers and detector layers stationed downstream of the STS detector. The proposed MUCH detector [97] will be different than the other existing muon detectors in the sense that in case of MUCH, the total absorber is sliced into thinner segments and placed along the beam direction with detector triplets in between the absorber segments [97]. The inherent design of the detector will make it possible to measure both low as well as high momentum muons[1] . However, the difficulties in designing the muon detector for the CBM experiment is manyfold. The multiplicity (or production cross-section) of J/ψ is very very less, of the order of 10^{-7} at 10A GeV (see Table. 2.1), while the branching ratio to the $\mu^+\mu^-$ channel is 0.06. Thus, on an average about 10^8 events will be required to produce a single J/ψ. In order to measure the rare probes[2] with a considerable statistics, CBM is planned to run the experiment at 10 MHz interaction rate. This unprecedented interaction rate imposes many practical challenges to design the detector. The challenges are

(i) to suppress huge unwanted hadronic background particles

(ii) to remove the contribution from pion and kaon decay muons i.e. $\pi^\pm \to \mu^\pm + \nu_\mu(\bar{\nu}_\mu)$ and $K^\pm \to \mu^\pm + \nu_\mu(\bar{\nu}_\mu)$,

(iii) high interaction rate requires fast detector response and radiation hardness,

(iv) the cost effectiveness.

It is, therefore, essential to perform simulation works on the design and performance of the proposed detector before making prototypes and finally the production of the detector. The simulation studies are needed not only during the planning of an experiment but also during the running of the experiment as well. A flow chart depicting the necessity of simulation is shown in Fig. 2.1. As shown in the left panel of Fig. 2.1, the simulation during the

[1]The low and high momentum muons are expected to arrive from the decay of LMVM (low mass vector mesons) and charmonia (J/ψ) respectively.

[2]includes D^+, D^-, D^0, $\bar{D}^0$, J/ψ, ψ'

Lab. Energy	Decay channel	Multiplicity (J/ψ)	B.R	Mult $\times$ B.R
10 A GeV	$J/\psi \to \mu^+\mu^-$	1.74×10^{-7}	0.06	1.000×10^{-8}
25 A GeV	$J/\psi \to \mu^+\mu^-$	1.92×10^{-5}	0.06	1.152×10^{-6}
35 A GeV	$J/\psi \to \mu^+\mu^-$	5.49×10^{-5}	0.06	3.294×10^{-6}

Table 2.1 The production cross-section of J/ψ at 10*A*, 25*A* and 35*A* GeV taken from HSD model [89–91], branching ratio into the $\mu^+\mu^-$ channel.

planning stage of an experiment lead to the estimation of optimized detector design in terms of required performance (S/B ratio and efficiency). Similarly, during the running stage of an experiment simulation is required in order to estimate the performance i.e. acceptance and efficiency of the detector, which is mandatory for any physics study (right panel of Fig. 2.1).

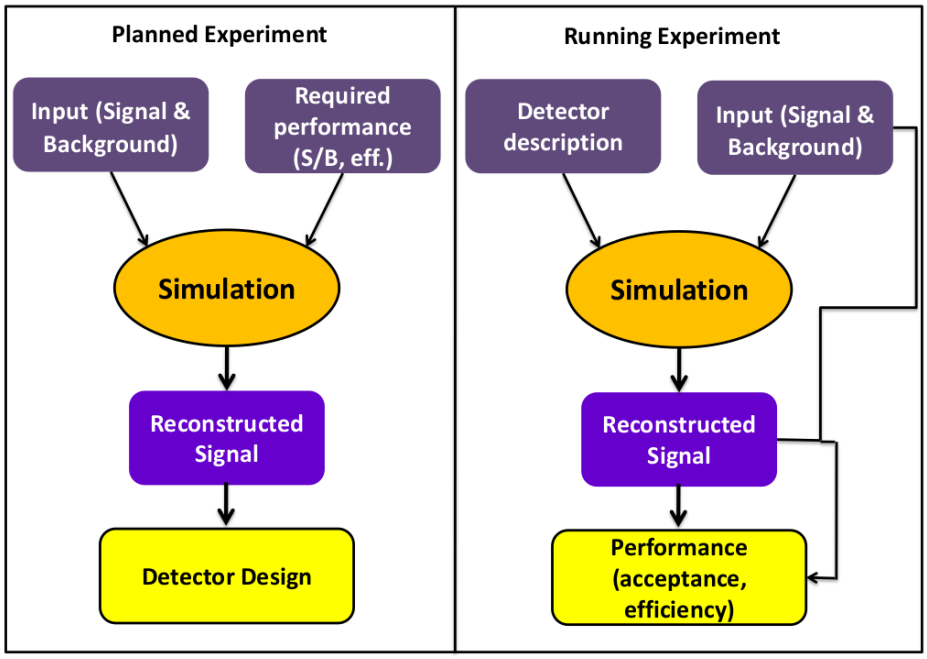

Fig. 2.1 A flow chart illustrating the utility of simulation in nuclear and high energy physics experiment [98].

The simulation study of the present investigation comprises mainly of two parts:

(a) the detector geometry optimization and

(b) performance study using optimized MUCH set-up on the basis of reconstruction efficiency and S/B ratio.

The geometry optimization can further be divided into several subclasses as depicted in Fig. 2.2. A detailed study regarding the geometry optimization has been performed and is

discussed in the section 2.4.1.

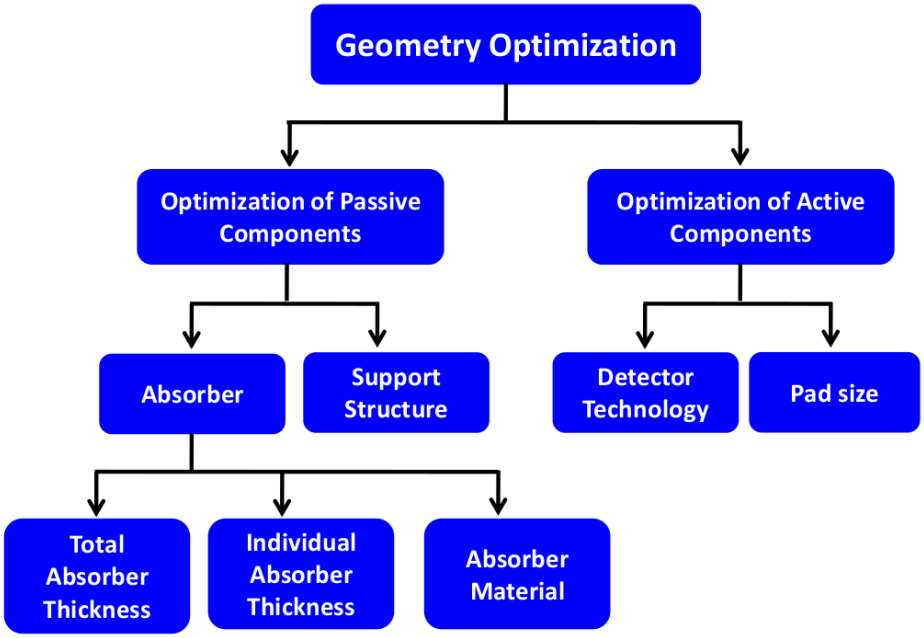

Fig. 2.2 Illustration of the geometry optimization employed for MUCH.

In the following sections an effort has been made to discuss the details of the software tools used for the entire simulation.

2.2 Software Tools

The entire CBM simulation software can broadly be divided into two major components –

(a) Fairsoft (or external package), and

(b) CbmRoot.

The structure of CBM simulation software in the form of a cartoon is depicted in Fig. 2.3.

2.2.1 FairSoft

FairSoft, also called *external package*, is a collection of third-party software packages required by `CbmRoot` [54]. The essential components of FairSoft are: ROOT [99], event generator (UrQMD [100–102], pluto [103], pythia [104, 105]), transport (GEANT3 [106], GEANT4 [107]) and libraries (GSL [108], CLHEP [109], boost [110] etc).

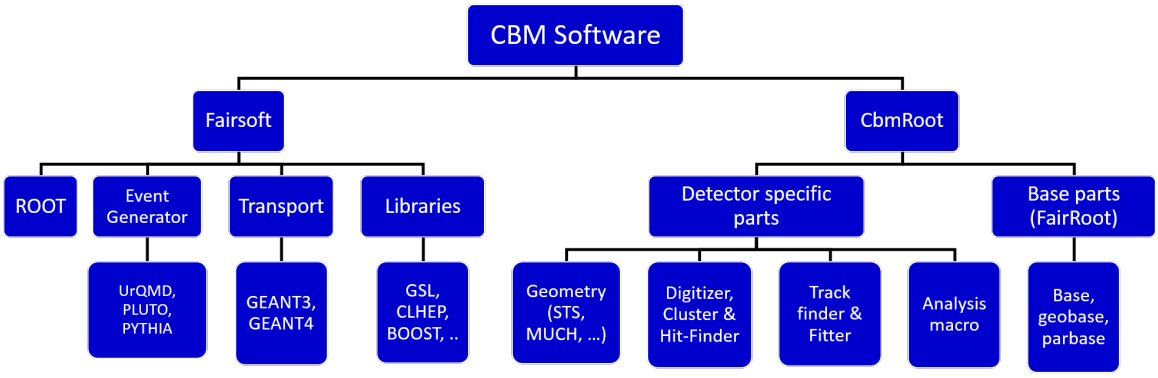

Fig. 2.3 A cartoon depicting the structure of entire CBM simulation software.

ROOT

ROOT [99] is a data analysis software framework extensively used by the high energy physics community. ROOT is based on the object-oriented design. The design of ROOT was initiated by Rene Brun and Fons Rademakers in the mid-1990s. The major advantage of ROOT is that it can handle a huge volume of data in an efficient way. ROOT was developed in the context of the NA49 experiment at CERN [111]. The basic functionality in ROOT are – histogramming, graph plotting, curve fitting, statistical tools for data analysis, four-vector as needed in high energy physics, matrix algebra, multivariate analysis, interfacing Monte-Carlo event generators, 3D geometry visualization etc. ROOT is, therefore, an inevitable part of CBM simulation and analysis.

Event generator

Event generators are the Monte Carlo based computer programs, written in HLL, to generate particles created in collisions (events) between elementary particles (or nuclei). The main input ingredients of event generators are [112],

1. Calculated matrix elements for various physical processes.

2. Experimentally measured or parametrized cross-sections for different physical processes.

3. Fragmentation functions etc.

In event generators, Monte Carlo technique is adopted to select all relevant variables according to the desired probability distributions [112]. The concept of randomness (or probability) as introduced by quantum mechanics can be realized in the event generators with the help of Monte Carlo technique. Normally an 'event' is a list of all final state observable particles i.e. hadrons, leptons, and photons, together with their momenta, isospin, charge, pdg code, and space-time coordinates etc. [112]. The following processes are generally simulated in a typical event generator [113],

- Hard processes
- Semi-hard processes
- Resonance decays
- Hadronization

The various event generators that are available with the FairSoft package are PLUTO [103], UrQMD [100–102] and PYTHIA [104, 105]. PLUTO is a Monte Carlo (MC) event generator based on both hadronic and heavy ion reactions and can be used from intermediate to moderately high energies. It consists of several c++ libraries e.g. `PParticle`, `PReaction`, `PFireball`, `PDecayManager` etc. PLUTO is entirely based on ROOT and is extensively used in CBM simulation for the generation of muons from the decay of J/ψ.

In CBM simulation, J/ψ particles has been generated with the help of a thermal fireball model (PLUTO) assuming a thermal p_t or m_t distribution,

$$\frac{dn}{m_t dm_t} = \frac{dn}{p_t dp_t} = m_t K_1\left(\frac{m_t}{T}\right) \propto e^{-m_t/T}, \tag{2.1}$$

where, K_1 is the modified Bessel function of second kind and order 1, $m_t = \sqrt{m^2 + p_t^2}$ is the transverse, m is the rest mass of the particle (J/ψ.), T is known as the inverse slope parameter whose value coincides with the thermal freeze-out temperature T_f in the static-fireball approximation i.e. when the flow velocity is zero.

The rapidity, on the other hand, can be approximated by a Gaussian distribution,

$$\frac{dn}{dy} = \exp\left(\frac{-y^2}{2\sigma_y^2}\right), \tag{2.2}$$

where, σ_y is the width of the rapidity distribution of J/ψ.

The J/ψ meson with thermal p_t/m_t and Gaussian rapidity distribution thus produced is, allowed to decay in its rest frame to $\mu^+\mu^-$– pairs. The longitudinal momentum of the daughter particles is boosted from center-of-mass frame to laboratory frame according to

Lorentz transformation. The multiplicity of J/ψ in central $Au+Au$ collision is taken from the Hadron String Dynamics (HSD) model (see Table. 2.1).

In CBM simulation, UrQMD, on the other hand, is used for the generation of hadronic background to mimic the heavy ion collision. UrQMD (Ultra-relativistic Quantum Molecular Dynamics) [100–102] is a microscopic transport model which describes the phenomenology of heavy-ion collision in terms of known hadrons and their resonances at low energies ($\sqrt{s} \leq 5$ GeV). Fifty five baryon species up to an invariant mass of 2.25 GeV and 32 meson species up to 2 GeV have been included in this model. At higher incident beam energies the string degrees of freedom are dominant and generally determine the dynamics of particle production. A brief introduction of the UrQMD model is provided in section 4.4.1 of Chapter 4.

Similarly, PYTHIA is an event generator generally describes the phenomenology of particle production in elementary particle collisions. Various known physical processes included in PYTHIA are,

(i) Hard QCD processes, e.g. $qg \rightarrow gq$,

(ii) Soft QCD processes,

(iii) Heavy flavor production processes, e.g $gg \rightarrow t\bar{t}$, $gg \rightarrow J/\psi g$,

(iv) photon induced processes, e.g. $\gamma g \rightarrow q\bar{q}$ and many more.

A comprehensive description of the PYTHIA model can be found in the refs. [104, 105].

Transport

GEANT3 [106] and GEANT4 [107], the software programs, written in FORTRAN and `c++` respectively, are used to transport the particles (generated from the Monte-Carlo event generators) through the detector set-up. Nearly all the Standard Model physics processes have been incorporated in GEANT package. GEANT4 is the successor of GEANT3 and consequently, some new physical processes have been incorporated there. The physical processes which have been considered in GEANT package can be broadly classified as – (1) electromagnetic, (2) hadronic, (3) decay etc. The **electromagnetic** processes involved

(i) **photon induced processes** such as photo-electric effect, Compton scattering, pair production, Rayleigh scattering etc.,

(ii) **electron/positron induced processes** such as multiple scattering, Bremsstrahlung, ionization and delta (δ) ray production, positron annihilation into two gammas, two muons and two hadrons etc.

(iii) **muon induced processes** such as ionization and delta (δ) ray production, Bremsstrahlung, e^+e^- pair production, multiple scattering etc.

The **hadronic** processes include the process like pion and kaon absorption, neutron capture, anti-proton and anti-neutron annihilation etc.

The **decay** process includes all the known strong, electromagnetic and weak processes. Apart from nuclear and particle physics experiments, GEANT finds application in several diverse subject area of science including accelerator, medical, space-physics etc.

Libraries

GSL, [108] also known as GNU Scientific Library, is a set of software library needed for numerical computation is also included in FairSoft. The distinct subject areas covered by GSL are – Complex number, special functions, statistics, interpolation, integral transforms, minimization, roots of polynomials, vectors and matrices, linear algebra, random numbers, Monte Carlo integration, differential equations etc.

CLHEP [109] or Class Library for High Energy Physics consists of several needed packages for high energy physics data analysis. The functionality included in CLHEP are – vectors, random numbers generation, matrix, geometry, etc.

Boost [110] contains a set of libraries of `c++`. It also supports several functionality such as linear algebra, pseudo-random number generation etc.

2.2.2 CbmRoot

CbmRoot [114] on the other hand is an experiment-specific code. Since virtual Monte-Carlo is incorporated in CbmRoot, the user code that creates simulated data does not depend on a particular Monte-Carlo engine [115]. During simulation, the sensitive detectors (active components) provide the simulated data which is stored into the binary ROOT file on an event-by-event basis. The class `CbmMCPoint` is responsible for defining the structure of registered hits in a detector [116]. The output data is organized in the form of “ntuple like" data structure with the help of the ROOT class called `TTree`. During analysis, the class `CbmRootManager` could be utilized to read the generated data. During analysis of the simulated data, various numerical parameters are needed e.g. calibration, digitization parameter, geometry positions of the detector etc. [116]. The class `CbmRuntimeDb` is responsible for handling the parameter definitions. Different format of inputs are supported in CbmRoot viz. Ascii, ROOT binary format and Oracle database input [116]. The inner structure of CbmRoot is shown Fig. 2.4. It could be seen from the figure that the framework has two

broad components: detector-specific component and base part as also illustrated in Fig. 2.3.

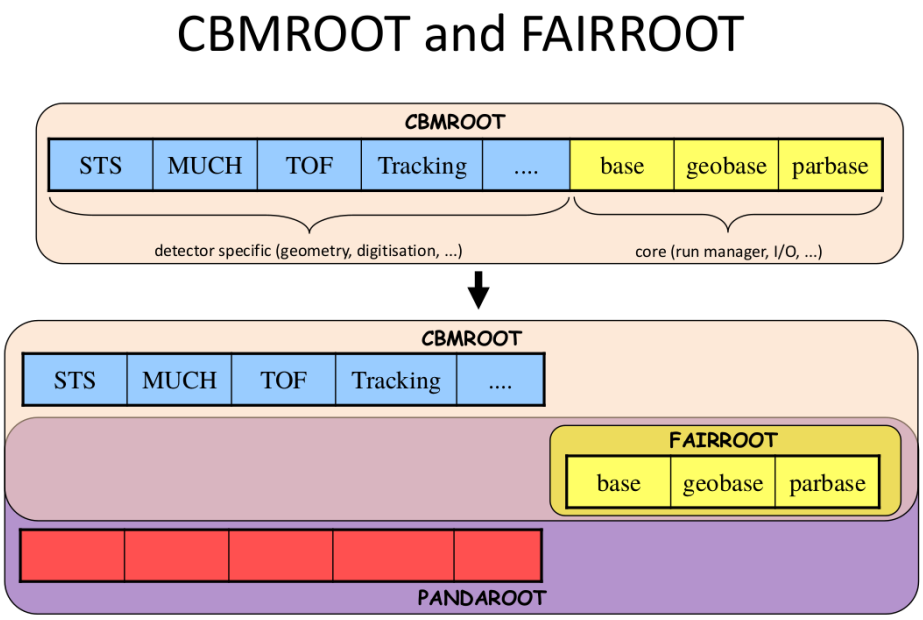

Fig. 2.4 The structure of CbmRoot and FairRoot [98].

The detector specific part have the following components and will be discussed in details in the section 2.3

- Geometry
- Digitizer
- Cluster finder
- Hit finder
- Track finder
- Analysis macro etc.

FairRoot [115, 117] is a software framework based on ROOT [99] which has been effectively used by CbmRoot for performing detector design simulation, track reconstruction, and online/offline data analysis. The basic structure of FairRoot is illustrated in Fig. 2.5. In this framework, a notoriously complex analysis task could be performed simply by making use of the task mechanism of ROOT framework. Although FairRoot was originally designed for CBM experiment [31–35], other upcoming experiments viz. PANDA [118, 119], R3B [120], ASYEOS [121] at GSI/FAIR etc. have subsequently been using the FairRoot framework as the base for their simulation, reconstruction, and analysis. The framework provides necessary arrangements to handle the classes responsible for performing simulation, reconstruction, handling of IO file and building of necessary geometry. On the other hand, the framework manages the base classes so as to handle the detector specific tasks e.g. defining

magnetic field, Monte-Carlo event generators and analysis. *Run Manager*, the main class of the framework executes (a) initialization (b) running event loops (c) handling IO with the help of IO Manager and (d) handling parameters using runtime database (*RTDatabase*). During simulation, it also sets up the necessary environment and sends the information (regarding geometry definition, material, magnetic field, event generators etc.) to the Virtual Monte Carlo application (*Application*).

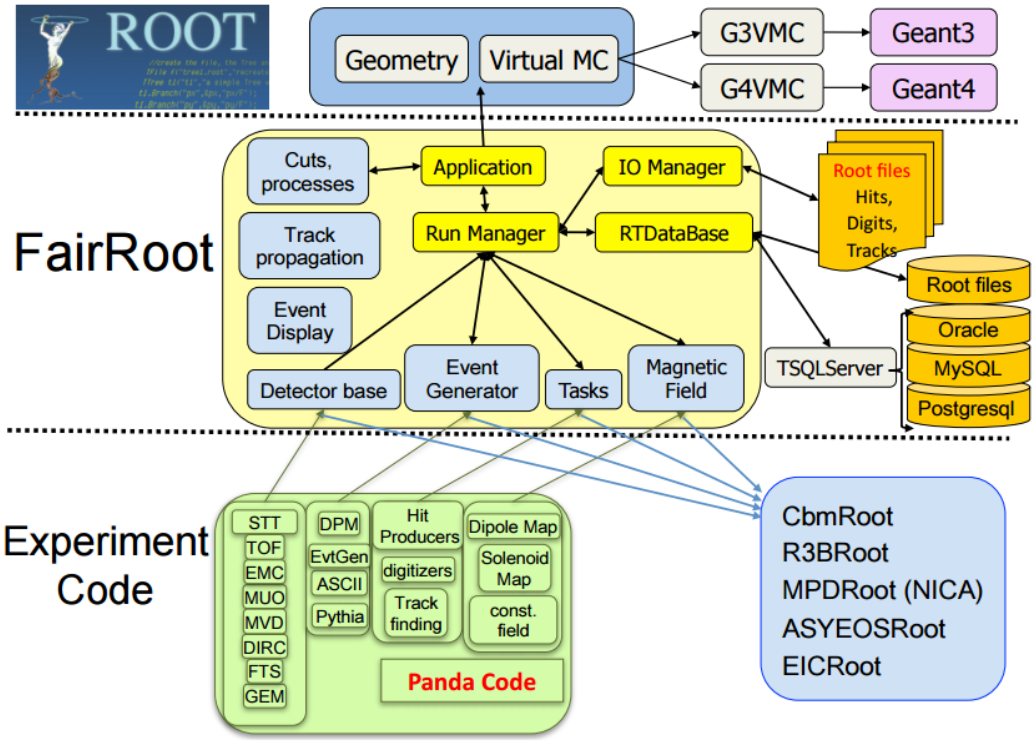

Fig. 2.5 The schematic layout of the FairRoot framework [116].

2.3 Simulation procedure

The various steps involved in the MUCH simulation are illustrated in Fig. 2.6. The simulation procedure consists of the following steps – (i) event generation (signal and background), (ii) implementation of the geometry (active and passive components), (iii) transportation of the generated particle through the detector geometry, (iv) segmentation of the detector plane, (v) digitization, (vi) clustering and hit-finding, (vii) track-finding and fitting and (e) identification of muon track candidates [31]. In the following, an effort has been made to discuss all the necessary steps of the simulation in details.

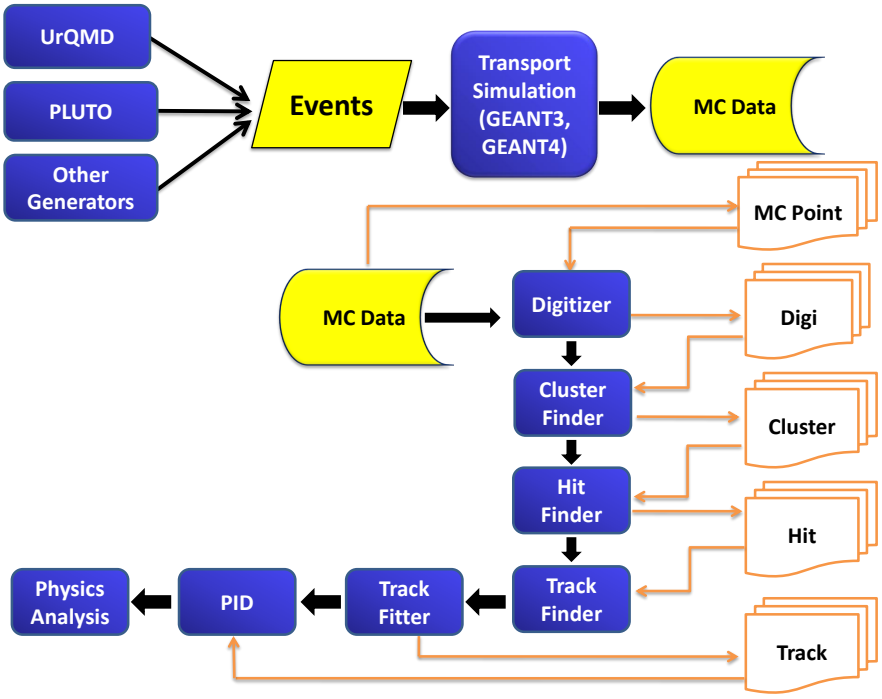

Fig. 2.6 A flowchart illustrating the simulation procedure employed in MUCH.

2.3.1 Event generation

The first step of the simulation involves the generation of particles to be transported through the detector geometry. The aim of the proposed Muon Chamber is to detect the primary muons coming from the J/ψ decay in a high-density environment. To mimic this situation, a hadronic string transport model UrQMD [100–102] is used which generates the required hadronic background. Since dileptons decaying from high mass vector mesons are not included in UrQMD model[3], a thermal model PLUTO [103] has been used to generate the muon-pairs from the decay of J/ψ. As stated earlier, for a 100% efficient detector nearly 10^8 events will be needed to detect a single J/ψ. The effect of acceptance and reconstruction efficiency of the detector will further reduce the J/ψ detection probability. Thus, to produce a reasonable number of J/ψ, a huge number of events need to be generated. Therefore, the kind of simulation where one J/ψ is embedded with 10^8 UrQMD events is quite unrealistic as it involves a huge amount of computational resource and lots of CPU time. To resolve this issue, in the present work, one $J/\psi \rightarrow \mu^+\mu^-$ has been embedded with each UrQMD event (central Au + Au collision). Thus, in the present simulation, both signal and background have been generated separately and at the analysis level, proper normalization has been

[3] although low mass dileptons are included in UrQMD model via Dalitz decays of π^0, η^0, ω, η' mesons etc. [100, 101]

incorporated. In this work, for the sake of comparison, both central and minimum biased $Au+Au$ collisions have been generated. Central collision events (impact parameter ~ 0 fm) are used to get an idea of the performance of the detector in the worst possible scenario.

2.3.2 Implementation of the detector geometry

CBM is a fixed-target experiment [31–35]. A fixed-target geometry generally produces particles in the forward direction. Thus, the detector needs to be placed in the forward direction to accept and detect the stream of forward-focused particles. The MUCH will be consisting of segmented absorbers (conical in shape) and thin detector layers (sector-shaped gaseous chambers). Each detector layer contains a support structure. An equal number of trapezoidal modules are placed on both sides of a support structure. The modules are arranged in such a manner that the border of the module in one side has an overlap with the modules of the other side so that the dead space is minimized. Various geometry related parameters such as the number of detector layers, the size, and thickness of the absorber, the absorber material etc. are needed to be optimized in terms of detection efficiency and S/B ratio.

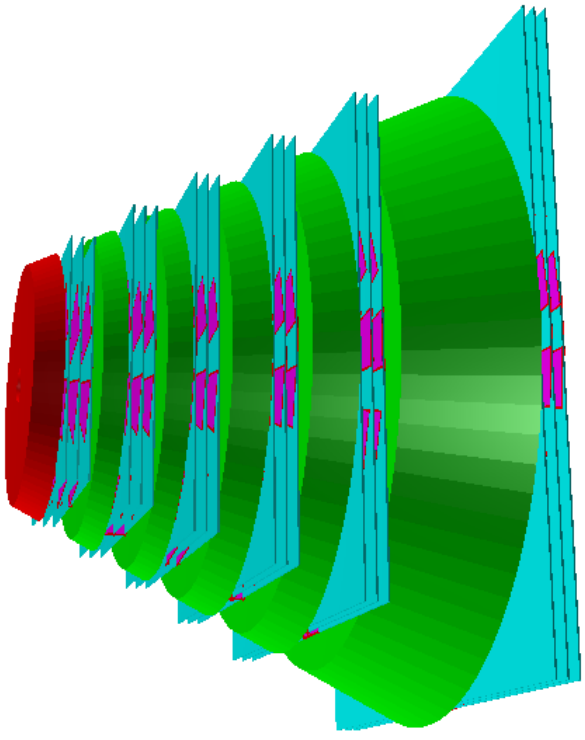

Fig. 2.7 Implemented detector geometry consisting of segmented absorber and detector triplets.

2.3.3 Transport simulation

The transportation of the produced particles through the detector set-up is done with the help of transport engine GEANT3/GEANT4 [106, 107]. As already discussed, the GEANT software package describes the interaction of the produced particles with the passive detector components (i.e. absorber medium in our case) via almost all the known physics processes. Although both the GEANT3 and GEANT4 functionality are available in the CbmRoot software framework, for the present simulation GEANT3 has been used for the transportation of the produced particles through the detector set-up. When the produced particles from the event generator level, termed as MC Tracks, are transported through the detector setup, GEANT3 provides the position of energy deposition inside the detector module (i.e. in the active component). These locations along with the energy depositions taken together are called MUCH points as illustrated in Fig. 2.8.

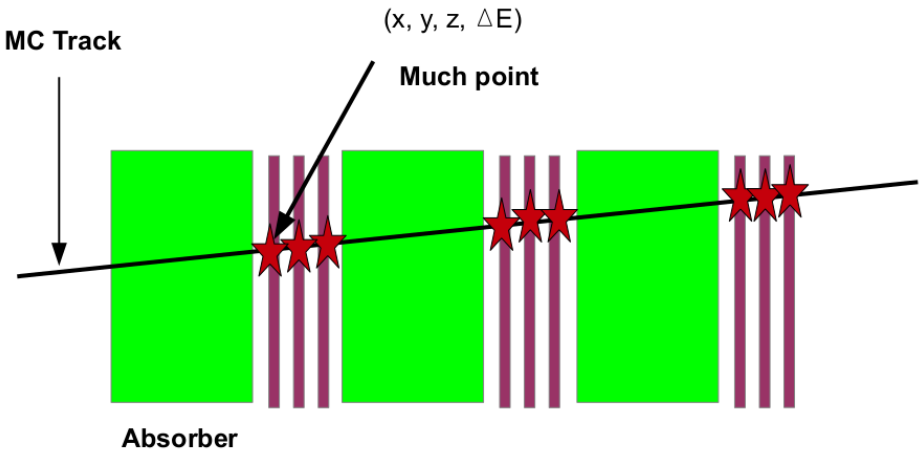

Fig. 2.8 The illustration of a MUCH point which is nothing but the coordinate of intersection of the MC track from the event generator with the detector layer along with the energy loss.

2.3.4 Segmentation

Position sensitivity is required for getting information about x, y, z of a particle. Thus, the readout modules are segmented in *pads* for obtaining the final detectable response [122, 31]. It is to be noted that with each individual *pads* a separate data acquisition set-up (i.e. pre-amplifier, amplifier etc.) are needed to be connected. For muon chamber, the projective segmentation scheme (see Fig. 2.9) has been implemented. In the projective segmentation scheme, the segmentation has been performed in such a way that the size of the *pad* increases radially and the dimensions of the *pads* are determined by the angular separation on the

transverse plane. To optimize the size of the *pads*, the following points are to be taken into consideration.

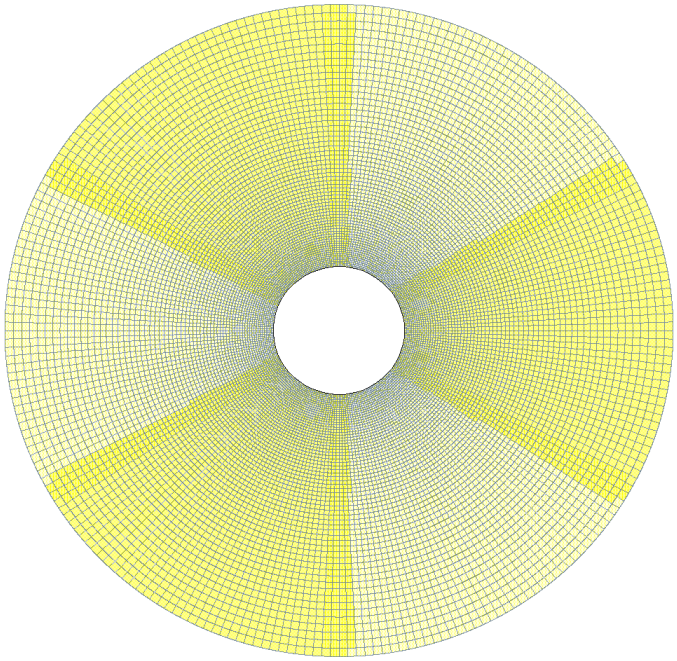

Fig. 2.9 Projective segmentation scheme for muon chamber.

Hit-Occupancy

Hit-occupancy is defined as the fraction of the total number of pads fired per event which gives an estimate of the data rate. The magnitude of hit-occupancy increases with increasing pad size. Occupancy is a useful quantity when comes to designing the readout boards. For the suitable functioning of the detector electronics, the desired value of occupancy is of the order of 5%. Thus, to keep the occupancy value small, the size of the pads need to be made as small as possible.

Fabrication, cost and position resolution

In order to minimize the hit-occupancy and from the point of view of position resolution, the pad-size need to make as small as possible. On the other hand, there is some practical limit (from the manufacturing point of view) and beyond which the size of the pads can not be reduced. Further, more number of pads will be required if one go for smaller pad sizes. And since for data acquisition, each pad needs to be connected to separate electronics, the

cost will rise exponentially. Thus, from optimization point of view, one has to compromise between cost and position resolution.

2.3.5 Digitization

After performing the segmentation of the detector plane into pads, the next task is digitization. The procedure/routine with the help of which the produced MUCH points can be redistributed among the pads are known as *digitization* [94]. Two types of digitization routine is available in the CbmRoot framework – (a) *Simple* digitization, and (b) *Advanced* digitization. In *simple* digitization, the points falling on a given pad area are collectively called *digit*. It is the simplest possible type of digitization and is quite unrealistic in nature since detector response is not included. For the present work, the *Advanced* digitization procedure is followed.

Advanced digitization

In Advanced digitization scheme, the GEM (Gas Electron Multiplier) detector response is taken into consideration. For the simulation presented here, Argon (Ar) gas is taken inside the detector volume. An incoming charged particle enters into the detector volume producing primary ionization. Corresponding to the MUCH point (location of energy deposition along with the space coordinate) primary ionization takes place in the gas volume and thus creating primary electrons. The number of these primary electrons depend upon the incident energy and the particle type. Since the fluctuation in energy loss follow Landau distribution and thus the primary electrons also follow the similar type of distribution [123]. The parameters of the Landau distribution (most probable value and FWHM) are taken from a simulation package HEED [124] and used in the present simulation. The number of primary electrons created in the drift region are amplified in the avalanche region due to the formation of secondary ionization. The gas gain or amplification factor is chosen to be 10^4 in the present simulation. The overlap between the transverse diffusion of the avalanche with the pad is known as *spot size*. The value of the *spot size* is obtained from the beam test and for the present case the value is taken to be 600 μm. The electric charge, accumulated in each pad, has been calculated, which depends upon the number of secondary electrons falling on it. Further to make the simulation realistic, random noise (with Gaussian smearing) in terms of electrons has been added to the system. The charge accumulated in a pad has been compared with the threshold value and the particular pad having accumulated charge greater than the threshold value with coordinate (r, ϕ) is known as a *digi*. Finally, the accumulated charge is converted into ADC channel following the standard methods for further processing. Here, the total number of ADC channel is considered to be 2048. Few other parameters related to

readout electronics are also needed to be tuned for the simulation. One such parameter is known as dynamic range of the ASIC (Application-Specific Integrated Circuit) used for data acquisition, which is defined as the maximum charge (Q_{max}) that can be collected. The value of Q_{max} for the present work was taken to be to 100 fc. To remove electronic noise, a charge threshold i.e. Q_{thr} = 1 fc was chosen [94].

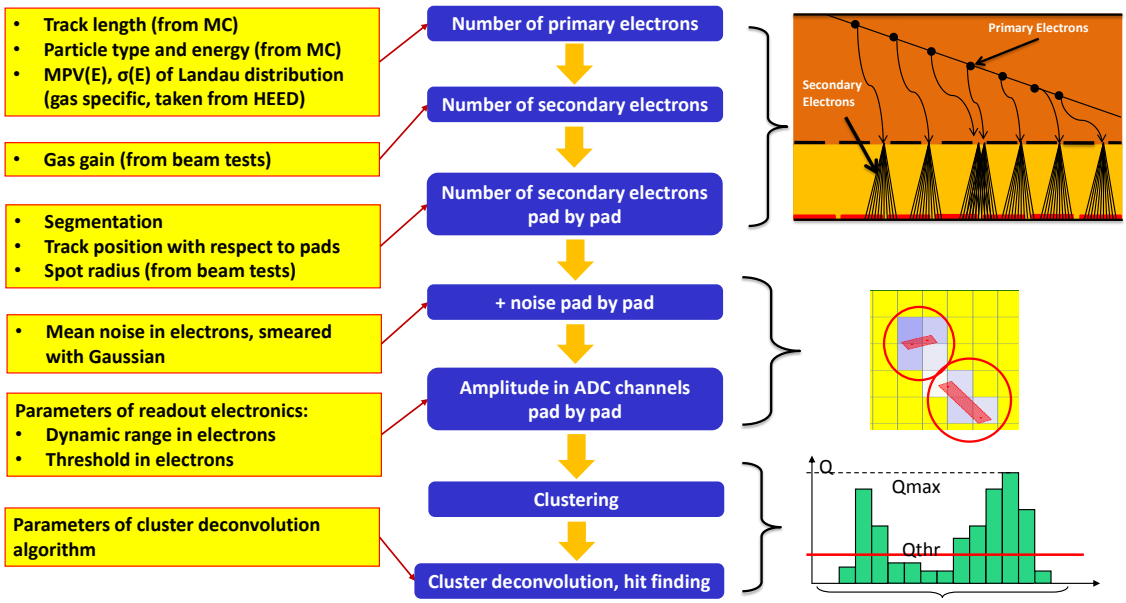

Fig. 2.10 Digitization and clustering procedure employed in MUCH [125, 126]

2.3.6 Clustering and Hit-finding

As discussed earlier, the fired pads with its coordinates are termed as *digit* object. Since the production of primary electrons in the gas volume is a statistical phenomena and generally described by Poissonian statistics [123], the secondary electrons thus produced from a single ionizing particle may also hit more than one pads. The similar situation may also occur for an inclined track coming from a decay. The *digits* thus produced are clubbed into clusters using a suitable clustering algorithm and finally, the clusters need to be deconvoluted to produce *hits*. Depending upon the nature of cluster formed, several cluster deconvolution algorithm/routine has been developed viz. (a) One hit per pad, (b) One hit per cluster and (c) Local maxima finder [31].

One hit per pad

It is the simplest of all and according to this algorithm, each fired pad i.e. each *digit* is termed as a hit [31]. In this algorithm, the hit-coordinates correspond to the center of the pad while hit-uncertainty can be calculated as follows.

If we consider that the probability of finding the particle between the two points a and b (Fig. 2.11) is uniform then the probability density can be written as,

$$\mathrm{p}(x) = \begin{cases} \frac{1}{b-a}, & \text{if} \quad a \leq x \leq b \\ 0 & \text{otherwise.} \end{cases}$$

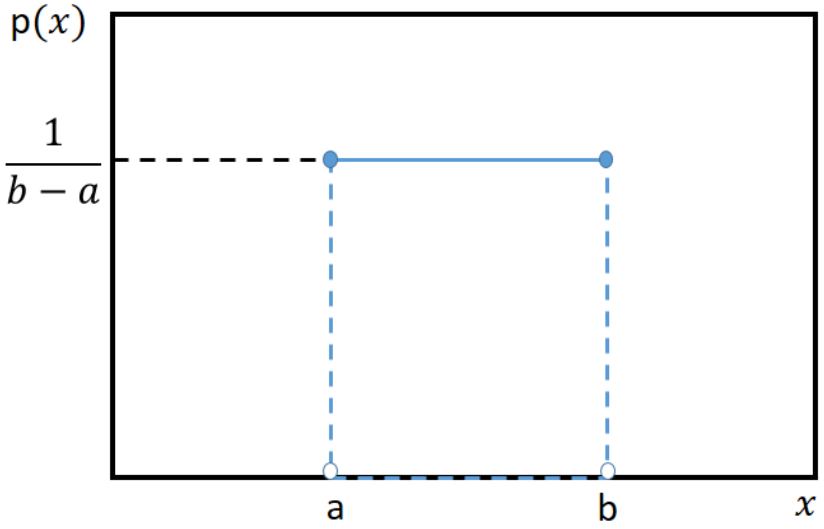

Fig. 2.11 The continuous uniform or rectangular distribution.

The expectation value of finding the particle between a and b is given by,

$$\langle x \rangle = \int_a^b x\mathrm{p(x)dx} = \int_a^b x\frac{1}{b-a}\mathrm{dx} = \frac{a+b}{2}. \tag{2.3}$$

The variance is given by ,

$$\begin{aligned} \sigma^2 &= \int_a^b (x - \langle x \rangle)^2 \mathrm{p(x)dx} \\ &= \int_a^b \left(x - \frac{a+b}{2}\right)^2 \frac{1}{b-a}\mathrm{dx} \\ &= \frac{1}{12}(b-a)^2. \end{aligned} \tag{2.4}$$

Thus, the standard deviation (S.D.) or uncertainty in finding the particle between the point a and b is given by,

$$\sigma = \frac{(b-a)}{\sqrt{12}}. \tag{2.5}$$

Here, the uncertainty of the *hit* will be equal to $\frac{1}{\sqrt{12}}$ times the pad dimension (see eqn. 2.5).

Although, from the implementation point of view this algorithm is best suited (needed less computational resource and less CPU time) yet, unrealistic in the sense that it generates lots many hits and most of them are fake hits and thus inefficient if used for track reconstruction.

One hit per cluster

In this algorithm, a cluster corresponds to a single hit. The hit coordinate can be obtained from the center of gravity averaging with weights corresponds to the charge accumulated in a pad. The hit coordinate and its error is given by,

$$x = \frac{\sum\limits_i x_i q_i}{\sum\limits_i q_i}; \qquad y = \frac{\sum\limits_i y_i q_i}{\sum\limits_i q_i} \tag{2.6}$$

$$\sigma_x = \frac{\text{(pad length)}}{\sqrt{12}}; \qquad \sigma_y = \frac{\text{(pad width)}}{\sqrt{12}} \tag{2.7}$$

where, q_i is the charge accumulated in the i^{th} pad and the *dummy* index i will run over the number of pads in a cluster. Though this algorithm works pretty nicely for smaller pads, for larger clusters there might be a considerable difference between the true track coordinate and the reconstructed hit.

Local maxima finder

This algorithm typically works very well for large clusters. The basic philosophy of this routine is to breakup the larger cluster into smaller sub-clusters. In this method, for each cluster, a search has been performed to locate the local maxima in the charge distribution. The reconstructed hit corresponds to the center of the pad having the maximum charge. For smaller clusters with a dimension less than 2×2, the previous algorithm i.e. *one hit per cluster* is used to reconstruct hits. It is worth mentioning that local maxima could also be caused by the inherent fluctuation in the charge generation (due to fluctuation in the ionization), thus few *fake* hits could also be created [31].

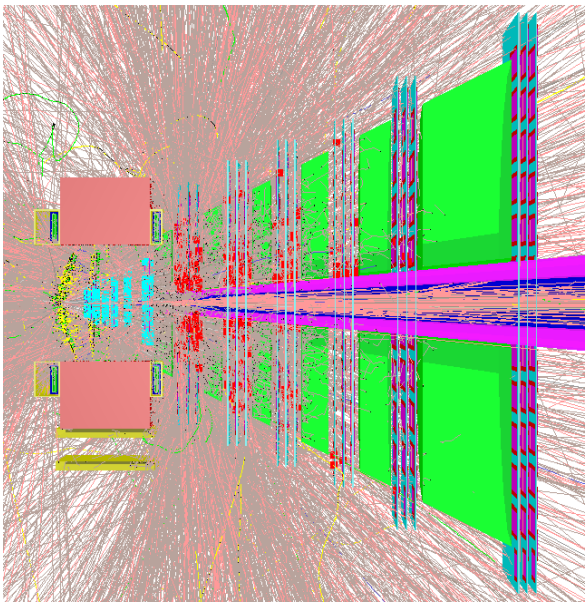

Fig. 2.12 A typical event display of a central $Au+Au$ collision at 25A GeV using UrQMD and GEANT3.

2.3.7 Track reconstruction in MUCH

The track reconstruction in MUCH is the most challenging task owing to the following reasons: (a) very high-density environment: near about 800 charged particles will be produced per collision, (b) high event rate of the order of 10 MHz. A typical event display of a central $Au+Au$ collision at 25A GeV using UrQMD and GEANT3 is shown in Fig. 2.12.

The tracking procedure employed in MUCH is rest on the track following algorithm using the already reconstructed STS tracks as seeds. Cellular automaton [127] is the method used to reconstruct the tracks in STS (Silicon Tracking System) [93]. Cellular automation provides the initial track parameters to MUCH as the starting point for its track following algorithm [128, 129]. The standard Kalman filter technique [130, 31] is the heart of track following algorithm which is used in MUCH for the calculation of track parameters and trajectory recognition. The track reconstruction in MUCH is based on the following components: (a) track propagation, (b) track finding and fitting, and (c) track selection.

Track Propagation

Track propagation is the heart of the track reconstruction method. In this algorithm, the average particle trajectory and its error are calculated [128, 129]. Further, the algorithm also takes care of the following physical processes which can alter the trajectory (1) energy loss which affects both the mean value and errors, (2) multiple Coulomb scattering which

influences error calculation only and (3) magnetic field which effects the average trajectory only [128, 129]. The track propagation algorithm can be subdivided into three components: the track extrapolator, the material effect calculator, and geometry navigator. *The track extrapolation* is governed by the equation of motion which in the absence of any magnetic field is assumed to be a straight line. In the presence of a magnetic field, the equation of motion of a charged particle can be solved by 4^{th} order Runga-Kutta method. *The material effect calculator* calculates and updates the momentum on regular basis due to the energy loss by the particle when passing through the medium. The physical process involved in the energy loss are - electromagnetic processes (i) ionization (Bethe-Bloch formula), (ii) bremsstrahlung (Bethe-Heitler formula) and pair production. Being a random process, multiple scattering effects only the covariance matrix. To estimate the average scattering angle the Highland formula with Gaussian approximation is considered. *The geometry navigator* uses the `TGeoManager` class of ROOT package [99] in order to take care of the material falling on its way and try to find the intersection point with the detector elements along a straight line [128].

Track Finding and fitting

The track finding algorithm is based on the method where the reconstructed hits at each detector plane are being attached with the propagated track. The above exercise can be performed in two different ways – *nearest neighbor* and *branching* algorithms [128, 129]. The *nearest neighbor* procedure picks up the closest hit and attach it with the track, whereas the *branching* algorithm attaches all the hits having a similar environment with the tracks. For both the methods Kamlan filter is used for the track following. Kamlan filter [130] basically updates the track parameter when the track reaches in the next detector layer where new hits are being attached to the track. Only those hits are considered for the *hit-to-track* assignment which falls on the *validation gate* [128, 129]. The *validation gate* is the region which is calculated about $\pm 3\sigma$ around the predicted position by assuming a Gaussian distribution of errors. The procedure is repeated until the last station is reached. The algorithm also takes cares of the missing hit in a detector plane due to detector inefficiencies [128, 129].

Track selection and performance

After track finding and fitting, the next step is to select the good tracks out of all the tracks formed. The track selection algorithm rejects the so-called *ghost* and *clone* tracks and selects only the good tracks. The *ghost* tracks are defined as the tracks which might be created out

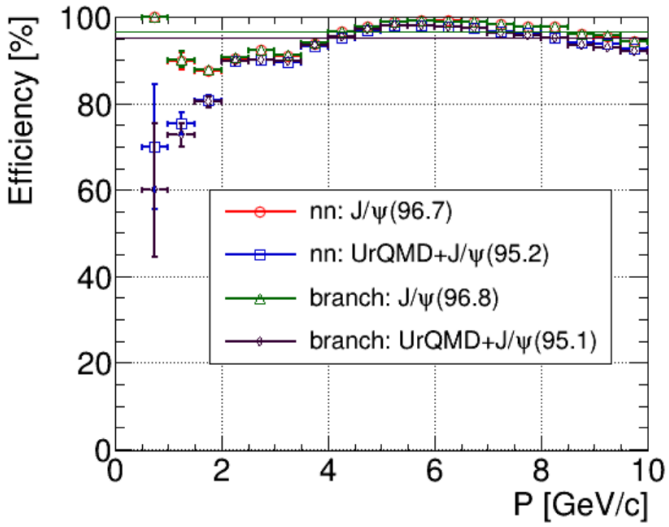

Fig. 2.13 The momentum dependent tracking efficiency using MUCH for central $Au+Au$ collisions at 25A GeV for SIS300 configuration.

of the random set of hits, whereas, *clone* tracks are the set of tracks having the similar set of hits. Good quality tracks are selected on the basis of χ^2 and track length [31].

A simulation has been performed for central $Au+Au$ collisions at 25A GeV using SIS300 geometry. UrQMD has been used to generate the background whereas signal ($J/\psi \rightarrow \mu^+\mu^-$) is generated using PLUTO event generator. In the simulation, as discussed above, 1 J/ψ decaying into dimuon i.e $\mu^+\mu^-$ is embedded in each UrQMD event. From Fig. 2.13, it has been observed that the average tracking efficiency for the J/ψ muons is almost independent of the type of tracking algorithm. Both *nearest neighbor* and *branching* show similar tracking efficiencies. Also, the efficiencies does not change much when UrQMD backgrounds are embedded with signal muons.

Out of the two, the *nearest neighbor* (nn) tracking algorithm is faster, simpler and easier from the implementation point of view. Therefore, for the subsequent simulation, the *nearest neighbor* method will be used.

2.3.8 Identification of muon track candidates

The previous section describes the reconstruction of the MUCH tracks. For the detection of muons, the information of momentum is essential. The momentum can be calculated in the STS detector. As discussed earlier, cellular automaton has been used for the track reconstruction in STS. The tracks reconstructed in STS are matched with the MUCH counterparts and the resulting track when extrapolated to the interaction vertex are known as global tracks [31].

For the identification of true muon tracks, a set of cuts has been applied on the global tracks. The cuts are - (i) number of hits in STS (ii) number of MUCH hits, (iii) the χ^2 of the MUCH track and finally (iv) χ^2 of the event vertex. The global tracks satisfying the above cuts are used for the invariant mass analysis for the reconstruction of J/ψ and will be discussed later.

2.4 Results and discussion

2.4.1 Optimization of detector geometry

Optimization of detector components generally consisted of two parts – optimization of
(a) **Passive components**: comprises of absorbers and support structures.

(b) **Active components**: includes the detector where the signal is generated.

In the present simulation, the support structures like electric cables, cooling system etc. have not been implemented.

In typical muon detection experiments, a thick absorber made of high Z material is generally used. In high energy heavy ion collisions hundreds and thousands of particles are being produced and most of which are hadrons like pions, kaons, and protons. The idea is to stop those huge hadronic backgrounds, so that only signal muons of interest can pass through and fall onto the detector. The amount of hadron absorption is directly proportional to the thickness of the absorber used. But the thickness of the hadron absorber can not be increased indefinitely since beyond a certain limit there is a finite absorption probability of signal muons as well. It is, therefore, necessary to optimize (a) the material and (b) the total thickness of the absorber so as to make a compromise between detection efficiency and signal to background ratio. CBM will be the unique experiment in the sense that it will be designed to detect both the high as well as low momentum muons coming from the decay of J/ψ and low mass vector mesons (LMVM) respectively. Conventional muon detectors use thick absorber to stop the hadronic background and place the detector behind it as shown in the left panel of Fig. 2.14. But the uses of thick absorbers put a limit to the experiments to detect only the high momentum muons. Thus, a novel approach has been adopted to design a Muon Chamber (MUCH) for the CBM experiment. In this approach, the thick absorber has been sliced into thinner ones and tracking detector layers have been placed in between to detect both high as well as low momentum muons (see the right panel of Fig. 2.14). In the following section, an attempt has been made to perform a simulation for the optimization of the thickness and material of individual absorber.

Further, in high energy heavy ion collision experiments, so many particles are produced in a single collision and to get a comprehensive information about the dynamics of the collisions,

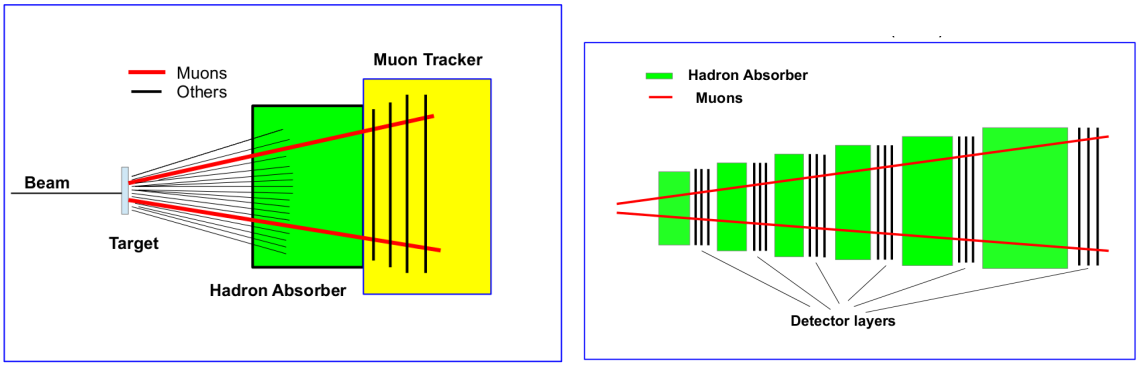

Fig. 2.14 (*Left:*) A conventional muon detecting system in the fixed target mode and (*Right:*) The present design of muon detecting system (MUCH) layout.

it is generally necessary to detect all of them. To meet this need, it is necessary either to use an array of identical detectors or to segment the whole detector in a number of pads for obtaining the final detectable response. The position resolution is an important parameter in heavy ion collision experiments as thousands of particles are produced. The position resolution of the detector can be increased simply by choosing smaller pad size. For data acquisition, each pad needs to be connected electronically via a spectroscopic amplifier, and preamplifier etc. Thus, as the pad size decreases, the cost increases exponentially. Further, there is a practical limit on the size of the pads. It is, therefore, necessary to optimize the granularity of the detector so as to compromise between the position resolution and cost.

Optimization of passive components

Total absorber thickness optimization

Fig. 2.15 shows the absorption of various particles as a function of total absorber thickness. A simulation has been performed with protons and pions as hadronic background and signal muons coming from the decay of J/ψ and ω and transported them through the hadron absorber. The material of the hadron absorber is chosen as iron (Fe) from its radiation length, cost etc. point of view and also since it is commonly used as absorber material in most of the muon detection experiments. In the simulation, equal number of each particle species were transported through the set-up. UrQMD-3.3 generator at E_{lab}=25A GeV was used to produce pions and protons, while PLUTO event generator was used to generate J/ψ and ω which immediately decay into muons [97, 94].

In the above simulation, the respective particles were identified from their monte carlo PDG codes. It is seen from Fig. 2.15 that as expected, the high momentum muons coming from the J/ψ decay are stopped less strongly than the softer ones coming from the LMVM

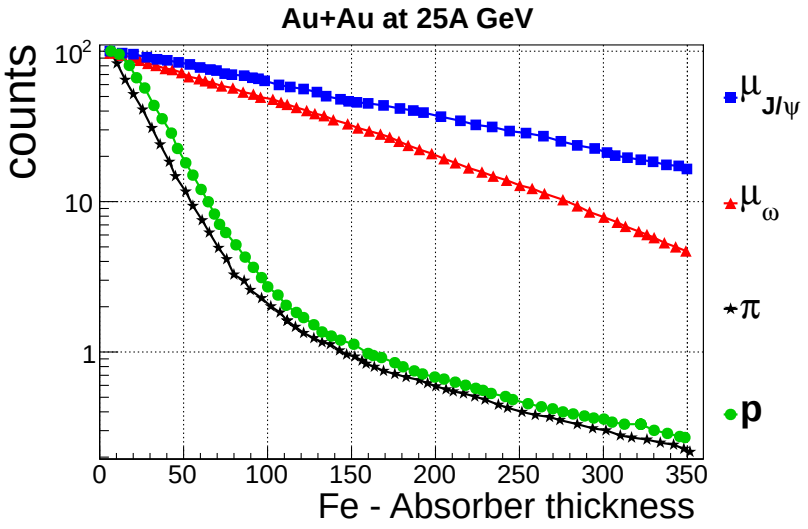

Fig. 2.15 Multiplicity of different particles (pions, protons and muons decayed from J/ψ and ω) as a function of thickness of the Fe-absorber [97, 94].

(ω) decay. Further, beyond 150 cm, slopes of the reduction of intensity of pions and protons are similar to that of the muons from ω which means that the S/B ratio will not improve further if additional absorbers are included. Thus, for efficient detection of LMVM, the optimized value of total absorber thickness is about 150 cm. But in case of muons coming from the decay of J/ψ, the background can be reduced further by an order of magnitude if an additional iron absorber of thickness 100 cm is added (Fig. 2.15) [97, 94].

Optimization of individual absorber thickness and its material

Apart from the total absorber thickness, the optimization of individual absorber thickness also plays an important role. In this front, the selection of thickness and choice of material for the first absorber is the most important task as it has to withstand in the highest hit density environment. The material and the thickness of the first absorber should be so chosen that the number of particles falling on the detector layers is reduced while the tracking chambers could operate efficiently. On the other hand, an increase in the thickness of the absorber will cause enhanced small angle multiple scattering. The deflection of the particle tracks due to enhanced multiple scattering can reduce the matching efficiency between the MUCH track segment and the STS counterparts. The process might cause an enhancement of the reconstructed background tracks. Thus, during optimization one has to compromise between the hadron absorption and multiple scattering [97, 94]. Thus, in the simulation, the selection of material and the thickness of the first absorber is made on the basis of two parameters - (a)

multiplicity of secondaries at the end of the first absorber, and (b) the number of background tracks reconstructed at the end of first absorber [97, 94].

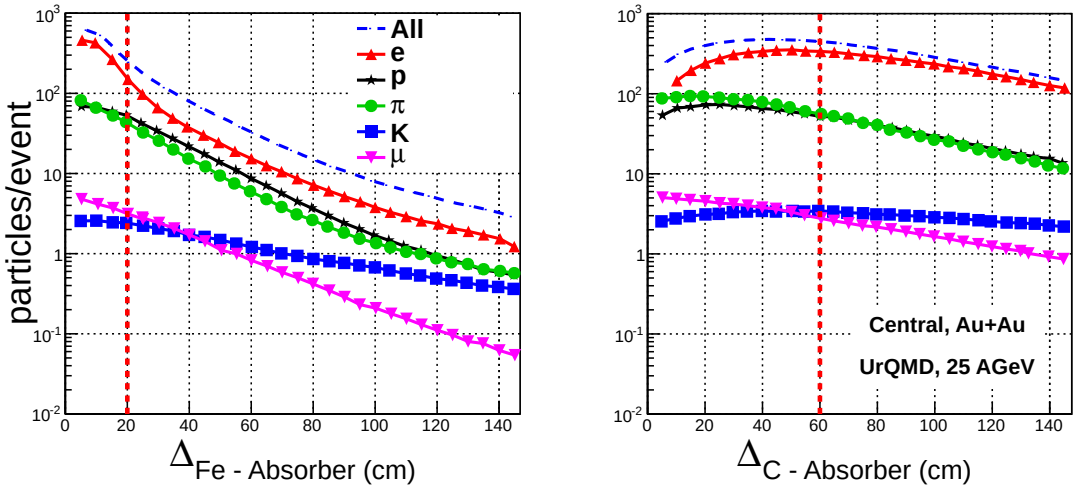

Fig. 2.16 Particle multiplicity as a function of 1st absorber thickness for *Left:* Iron (Fe) and *Right:* carbon (C) [97, 94].

The simulation has been performed for central $Au+Au$ collision at 25A GeV. In Fig. 2.16, the variation of particle multiplicity is plotted as a function of first absorber thickness. The study has been performed for two types of first absorber materials viz. iron (*left*) and carbon (*right*). From simulation, it has been observed that for both types of materials, the secondary electrons (δ-electrons) dominate, which rise initially and then fall with increasing absorber thickness. The red vertical dashed lines indicate the proposed thickness of the first absorber for both iron (Fe) and carbon (C) of similar interaction lengths. The (secondary) particle multiplicity behind the absorber of those thicknesses is within the detectable limit of tracking chambers (discussed in details in the section 2.4.1). It is clearly seen from Fig. 2.16 that the iron (Fe) absorber absorbs the secondary particle more strongly than that of carbon (C). Thus, as far as the absorption of secondary particles is concerned, iron (Fe) absorbers seem to be the better choice.

As discussed earlier, the multiple scattering is an important criterion when optimizing the first absorber material and its thickness. With the increase in the thickness of the hadron absorber, the probability of multiple scattering is also increased which in turn increases the probability of background reconstruction. In Fig. 2.17, the ratio of the number of reconstructed track [4] to the number of MC tracks has been plotted as a function of first absorber thickness. The reconstructed track might include some wrong combinations: the

[4]Track selection criteria: 4 STS hits and 2 MUCH hits

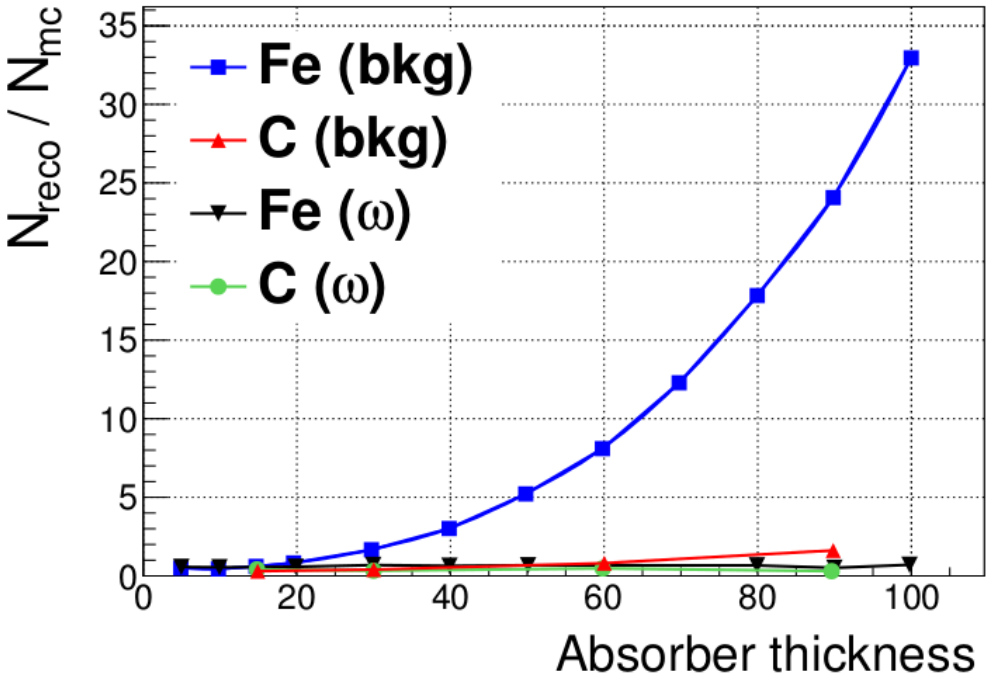

Fig. 2.17 The ratio of the number of reconstructed track to the number of MC tracks has been plotted as a function of first absorber thickness.

track consisting of 4 STS hits might stop in the first MUCH absorber and an electron produced in that absorber may create MUCH hits. Here, although the number of reconstructed tracks amounts to 1, yet the number of MC track detected by MUCH is zero. Thus, this mismatch probability increases with the thickness of the absorber as illustrated in Fig. 2.17. In this figure, the above-said ratio has been plotted both for carbon as well as iron absorbers. It is clearly seen from the figure that the ratio or equivalently the mismatch probability for background increases exponentially for the iron absorber, whereas for carbon a weak dependence of the ratio with thickness has been observed. Thus, carbon absorber seems to be the better choice as far as the number of reconstructed background track is concerned.

Further, in the present design of CBM detector set-up, a part of the first MUCH absorber needs to be placed inside the dipole magnet. Thus, as far as the mechanical integration of the set-up is concerned, the carbon absorber have the added advantage over iron. Hence, for the subsequent simulation, 60 cm of carbon (as depicted by the right hand side of Fig. 2.16) will be used as first absorber while the other absorbers are made of iron in order to make the system compact which reduces the muon background (from the weak decays of pions and kaons) considerably.

Optimization of active components

Choice of detector technology on the basis of hit-density

The angular coverage of MUCH detector is from 5^0 to 25^0. Such huge acceptance demands the manufacturing of large area detectors. Since MUCH will be placed nearly 1.5 m downstream the target, in the SIS-300 mode with 18 detector layers, the total active detector area needed will be approximately 160 m^2. Looking at the requirement of the large area detector, the gaseous detector will be the obvious choice. Further, as discussed above, the interaction rate in CBM experiment will be of the order of 10 MHz i.e., there will be 10^7 collisions per second. Furthermore, at FAIR energies a single $Au+Au$ collision is capable of producing around 1000 particles and hence nearly 10^{10} particles will be produced per second. To detect such huge amount of particles within a very short time, the detector needs to be both fast and radiation hard. In this respect also gaseous detectors will be the best choice. Considering the above facts, the best-suited detector for this environment will be GEM (Gas Electron Multiplier). Further, in order to select the detector technology to be used in this high radiation environment, we estimated the data rate behind the hadron absorber placed at 1.5m downstream the target. The particle density (number of particles per unit area per event) has been calculated and plotted as a function of radius as shown in figure 2.18. As expected, the particle density is peaked near beam pipe and falls rapidly with radius. The peak density per central $Au+Au$ collisions at 10A, 25A and 35A GeV is found to be 0.1, 0.4 and 0.5 particles/cm^2 respectively. Thus, for the reaction rate of 10 MHz, this the peak data rate corresponding to 10A, 25A, and 35A GeV will be (10 MHz $\times$ 0.1 =) 1 MHz, (10 MHz $\times$ 0.4 =) 4 MHz, and (10 MHz $\times$ 0.5 =) 5 MHz per cm^2 respectively. For minimum bias collisions, the particle densities are expected to decrease by a factor of 4. These data rates observed for 1 cm^2 pad size will be reduced according to the size of the pad. It is to be noted that the prototype detectors has been made and tested using GEM technology which has been operated successfully at the reaction rate of 1.4 MHz/cm^2 [93].

Segmentation optimization

The muon tracking chambers designed to identify muons will be under the conditions of high hit density and large event rates (10 MHz). The detector thus need to be position sensitive and the readout planes of the modules are required to be segmented into pads for obtaining final detectable response [94, 122]. The aim of the segmentation study is to get a realistic and optimized detector layout with respect to the physics measurements. As mentioned earlier, projective segmentation scheme has been considered here, according to which the size of the pads increases radially. Ideally, although the projective segmentation demands the shape of

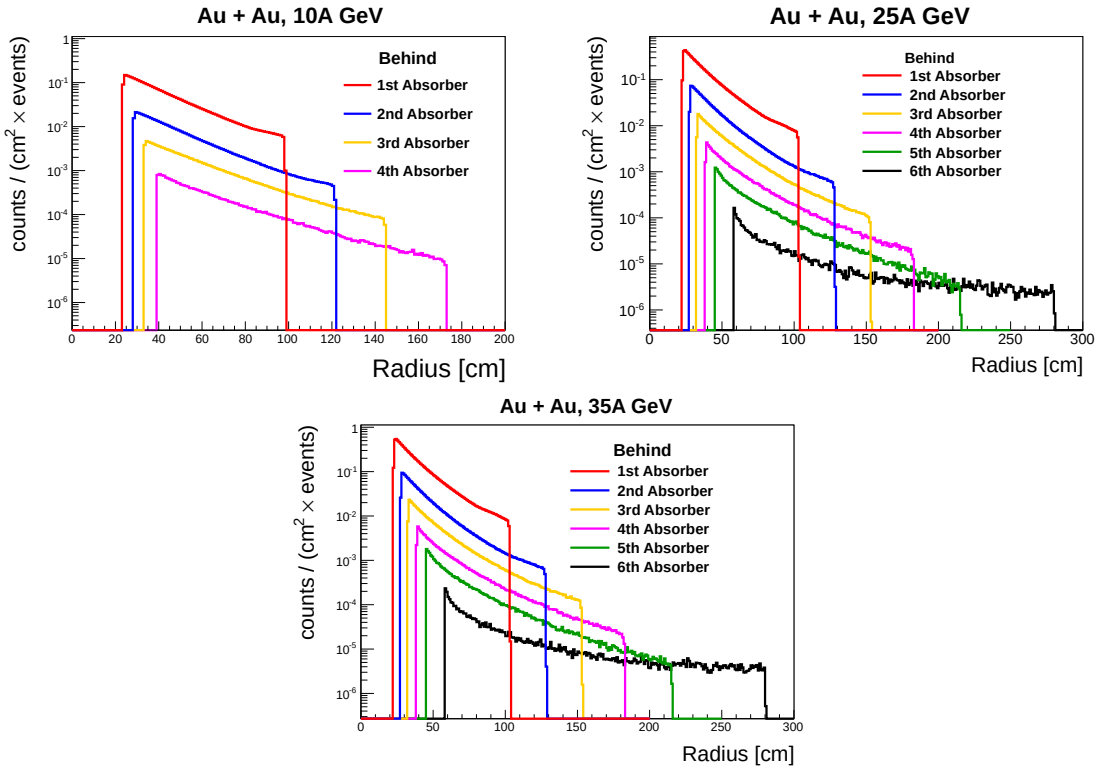

Fig. 2.18 Particle density as a function of radius for central $Au+Au$ collision at 10A, 25A, 35A GeV respectively.

the pads to be of trapezoidal, yet, for the simulation purpose square pad approximation have been considered. The parameter known as *pad angle* in the square pad approximation will determine the size of the smallest acceptable pad. For example, 1^0 *pad angle* corresponds to the minimum and maximum pad size of 0.26 cm^2 and 1.33 cm^2 respectively for the first station. The minimum and maximum pad size for 1^0 segmentation scheme for the SIS-300 configuration along with the total number of pads is shown in the Table 2.2.

The large acceptance detectors of MUCH will give it access to almost the entire forward phase space depending on the particle type. As discussed earlier, the angular acceptance of the detector spans from 5^0 to 25^0 which corresponds to the pseudorapidity (η) range from 3.18 to 1.5. It is expected that particle density would be largely varied over the detector acceptance. Such variation of particle density might result in the variation of hit and track efficiencies of the detector at different pseudorapidity region. Hence a study on pseudorapidity dependent hit-efficiency of the detector is of considerable significance.
Hit-efficiency is defined as the ratio of number of reconstructed hit to the number of MC point.

$$\text{Hit-efficiency} = \frac{\text{Number of reconstructed hits}}{\text{Number of MC points}} \tag{2.8}$$

Station	Minimum pad size (c.m)	Maximum Pad size (c.m)
1	0.26×0.26	1.33×1.33
2	0.35×0.35	1.75×1.75
3	0.43×0.43	2.20×2.20
4	0.54×0.54	2.71×2.71
5	0.65×0.65	3.27×3.27
6	0.88×0.88	4.40×4.40
		Total number of pads = 6,15,600

Table 2.2 Station wise details of the segmentation scheme employed

For this study, the simulation has been performed at $E_{lab} = 10AGeV\ Au+Au$ collision where background particles and signal muons (from J/ψ decay) have been generated using UrQMD [100–102] and PLUTO [103] event generators respectively.

Fig. 2.19 shows the hit-efficiency for different segmentation scheme as well as for different cluster deconvolution algorithm (discussed above) as a function of pseudorapidity. It is readily seen from the figure that the hit-efficiency decreases towards mid-rapidity where the particle density is maximum. Further, hit-efficiency is found to be more for pad angle of 0.5^0 due to the decrease of multi-hit probability. Also, for both the segmentation scheme i.e., 0.5^0 and 1^0, the algorithm 'local maxima finder' (LMF) seems to be better as far as hit-efficiency is concerned [122].

Pad angle	Algorithm	efficiency (embedded)
0.5^0	OHPC	14.0 %
	DCT	14.2 %
	LMF	14.3 %
1^0	OHPC	14.2 %
	DCT	14.2 %
	LMF	14.3 %

Table 2.3 J/ψ reconstruction efficiency for different cluster deconvolution algorithm and segmentation scheme [122].

The J/ψ reconstruction efficiency has been calculated for different segmentation scheme as well as for different cluster deconvolution algorithm. It is seen from Table 2.3 that the J/ψ reconstruction efficiency is almost independent of the segmentation scheme considered. Thus, as far as cost is concerned, the pad angle of 1^0 seems to be the better choice. Also,

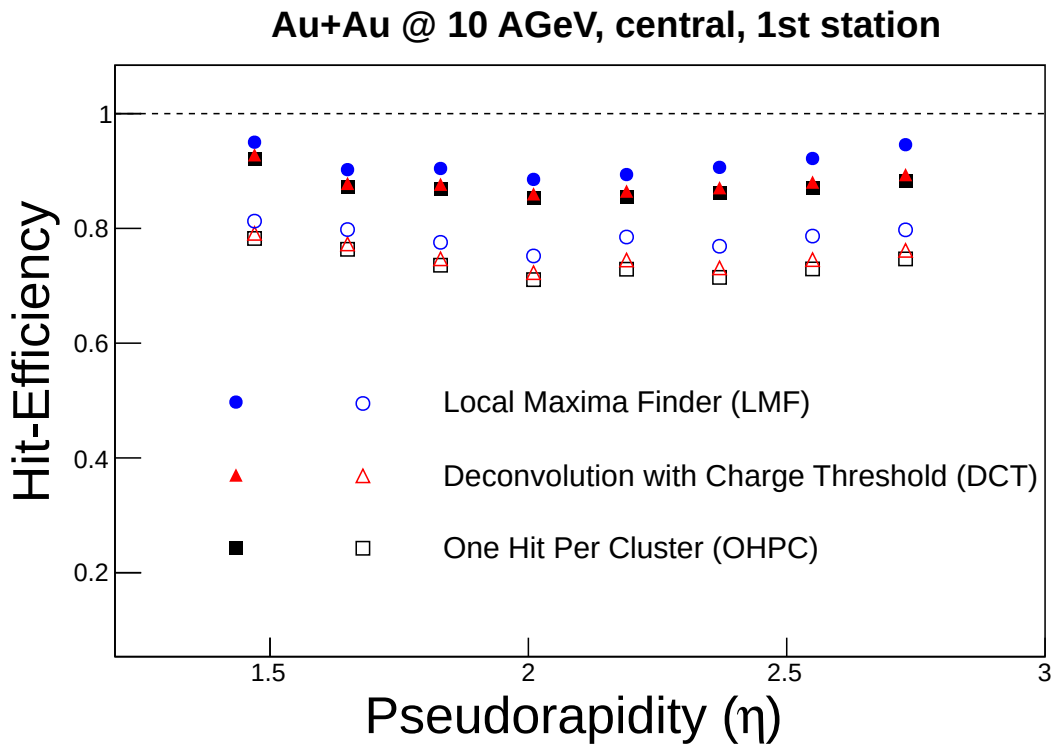

Fig. 2.19 Hit-efficiency as function of pseudo-rapidity for the 1st station for different cluster deconvolution algorithm. The solid symbols corresponds to pad angle 0.5^0 while open symbols are for pad angle 1^0 [122].

for both the segmentation scheme, the LFM algorithm gives the maximum signal efficiency. Thus, 1^0 pad angle and LMF algorithm are found to be the optimum choice [122].

Further, the invariant mass distribution of combinatorial background (will be discussed later) has been plotted in Fig. 2.20 for different segmentation angle (or pad angle). It is clearly seen from the figure that although the combinatorial background beyond the invariant mass 1 GeV/c^2 is similar for all segmentation angles yet, 1^0 segmentation angle gives little lesser background near the J/ψ mass region (See the zoomed version of the figure corresponding to the invariant mass range from 2.4 to 4 GeV/c^2). It is, therefore, concluded that 1^0 segmentation is the optimum choice and the rest of the simulation has been performed by setting the segmentation angle to 1^0.

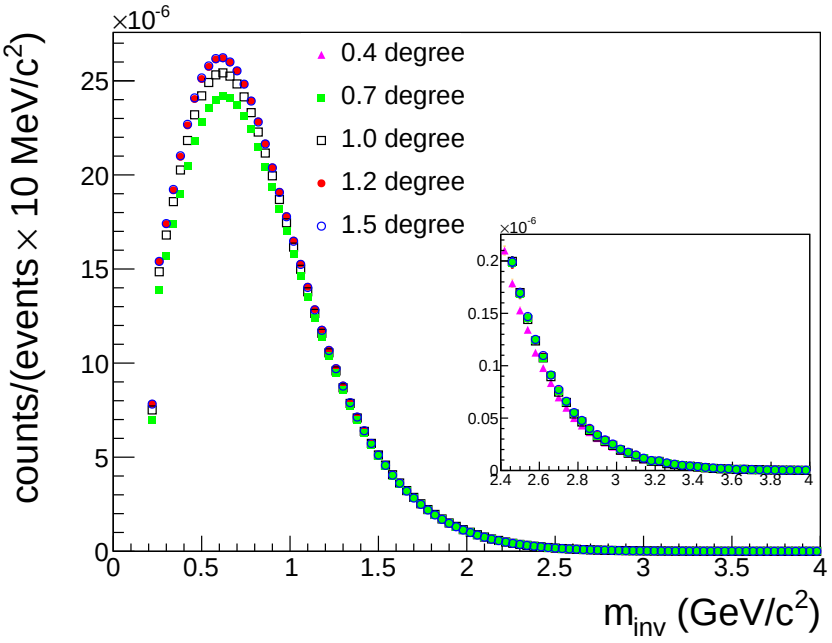

Fig. 2.20 The combinatorial background invariant mass distribution for various segmentation angle.

2.4.2 Performance study using optimized MUCH set-up

Input of the simulation

As already discussed in the section 2.3.1, for the generation of J/ψ, a thermal model has been used. The thermal model assumes a Gaussian rapidity (eq. 2.2) and exponential p_t/m_t (eq. 2.1) distribution as shown in Fig. 2.21

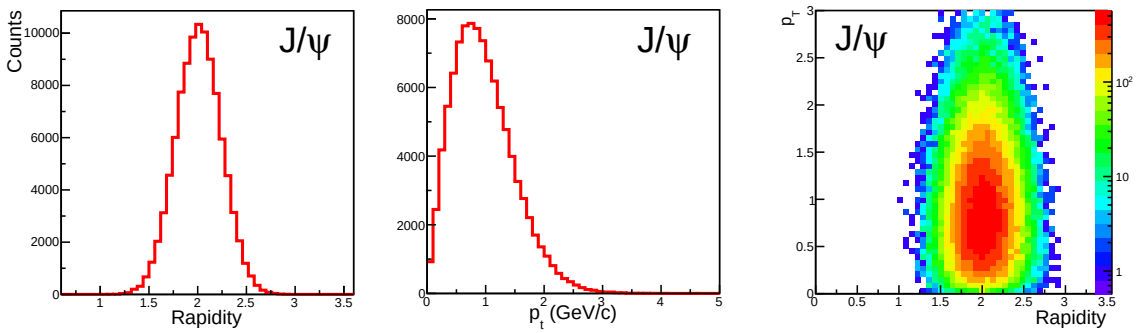

Fig. 2.21 *Left:* Rapidity distribution, *Middle:* transverse momentum distribution and *Right:* y-p_t distribution of the input J/ψ at 25*A*GeV used in the simulation.

Optimized MUCH geometry for J/ψ detection

In the SIS-300 mode, for the detection of J/ψ, the following geometry as shown in Fig. 2.22 has been proposed. The detector comprises of six absorber layers and six detector triplets. The first absorber is made of carbon whose thickness is considered to be 60 cm. For compactness, the rest of the absorbers are made of iron and their thicknesses are 20+20+30+35+100 cm. The distance between the absorber and the layers is fixed to 5 cm, while the separation of the tracking layers in a triplet is taken to be 10 cm. As mentioned earlier, in the present MUCH set-up a part of the first absorber (i.e., 40 cm in this case) lies inside the dipole magnet, whereas the remaining part i.e., 20 cm of the absorber lies outside of the dipole magnet.

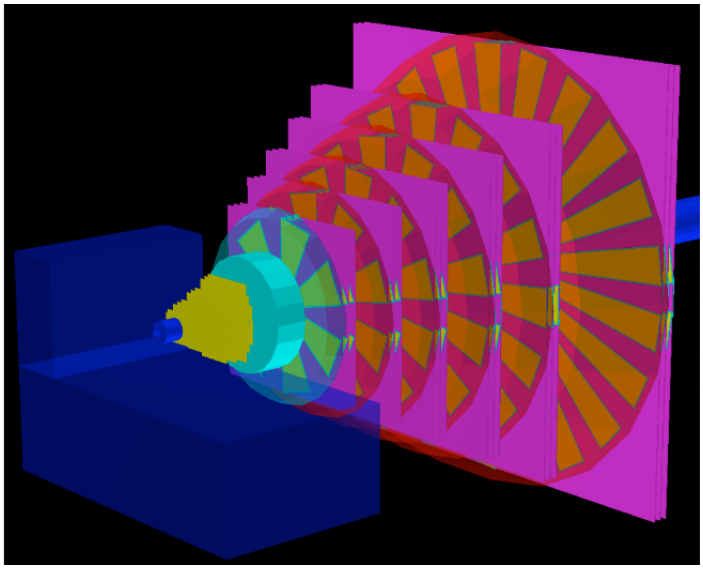

Fig. 2.22 Proposed MUCH geometry for SIS300 configuration (18 GEM stations, 1st absorber = 60cm C).

Invariant mass analysis for J/ψ Reconstruction

As discussed in the section 2.3.8, the true muon candidates are selected from globally reconstructed tracks after applying a set of cuts discussed in that section. The muon candidates are then handpicked for dimuon analysis. In the dimuon analysis, 4-momentum of the oppositely charged particles are added from the same event.

The 4-momentum of μ^+ and μ^- in terms of energy and 3-momentum can be written as:

$$P_{\mu^+} = (p^0_{\mu^+}, \vec{p}_{\mu^+}) = (E_{\mu^+}, \vec{p}_{\mu^+}) \tag{2.9}$$

$$P_{\mu^-} = (p^0_{\mu^-}, \vec{p}_{\mu^-}) = (E_{\mu^-}, \vec{p}_{\mu^-}) \tag{2.10}$$

The 4-momentum of dimuon can be calculated by adding the 4-momentum of the oppositely charged particles.

$$P_{J/\psi} = P_{\mu^+\mu^-} = P_{\mu^+} + P_{\mu^-} \tag{2.11}$$

$$= (E_{\mu^+} + E_{\mu^-}, \vec{p}_{\mu^+} + \vec{p}_{\mu^-}) \tag{2.12}$$

The invariant square of $P_{J/\psi}$ can be written as

$$P^2_{J/\psi} = P^\mu P_\mu = E^2 - \vec{p}^2 = m^2_{J/\psi} \tag{2.13}$$

Where μ is the *dummy* index and $m_{J/\psi}$ is the invariant mass of J/ψ. Also $E = E_{\mu^+} + E_{\mu^-}$ and $\vec{p} = \vec{p}_{\mu^+} + \vec{p}_{\mu^-}$. Thus the numerical formula for invariant mass of the mother particle (J/ψ) in terms of its daughter particles (μ^+ and μ^-) can be written as -

$$m_{J/\psi} = \sqrt{(E_{\mu^+} + E_{\mu^-})^2 + (\vec{p}_{\mu^+} + \vec{p}_{\mu^-})^2} \tag{2.14}$$

Background estimation via Superevent analysis

As already discussed, for a 100% efficient detector, nearly 10^8 events needed to be generated to detect a single J/ψ. In the simulation, the kind of situation as that of a real experiment can not be mimicked from the point of view of computing resource and time. Thus to reduce the CPU time, in this work, an event mixing technique has been employed for the generation of background. In this method, the track of a positively charged particle is combined with the tracks of all negatively charged particles. But during combination, the oppositely charged particles are selected from different events only i.e., the combinations of same events are excluded.

Estimation of S/B ratio

As discussed above, the invariant mass technique has been employed for the reconstruction of both the signal (J/ψ) and the background. For the reconstruction of the signal, the oppositely charged particles are combined from the same event, whereas, for the reconstruction of background the combinations are made from different events. The signal and background invariant mass distributions have been fitted using a Gaussian and an exponential function respectively (see Fig. 2.23). The S/B ratio has been calculated by extracting both signal and background around $\pm 2\sigma$ window of the signal peak.

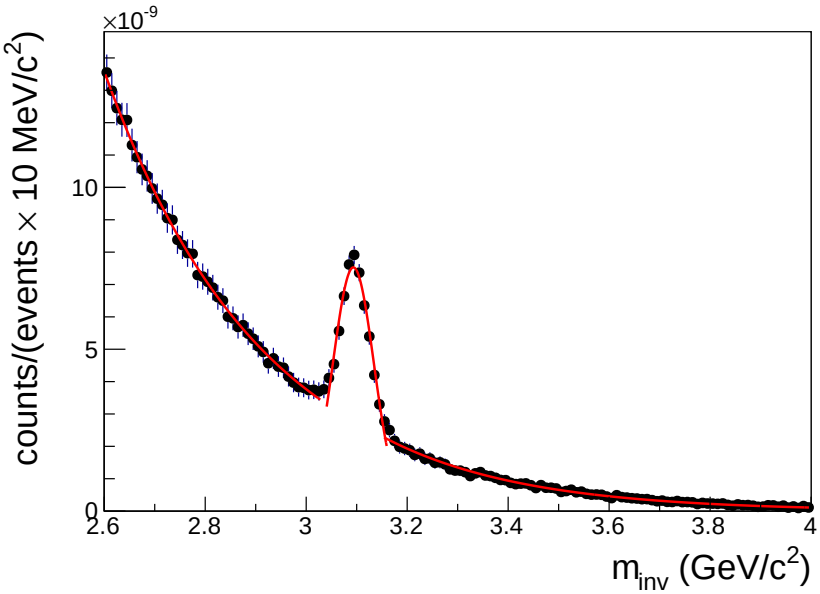

Fig. 2.23 Multi-component fitting of the signal and background. The signal is fitted with a Gaussian whereas, the background is fitted with an exponential function.

Efficiency and S/B ratio optimization

Table. 2.4 shows the values of various cuts used for present optimization study such as the number of MUCH hits, the number of STS hits, the χ^2 of the event vertex and the χ^2 of the MUCH tracks etc. The cuts can be optimized on the basis of two important parameters,

(i) S/B ratio,

(ii) signal (J/ψ) reconstruction efficiency.

The actual figure of merit of any experiment depends on the S/B ratio. The signal reconstruction efficiency is,

$$J/\psi\text{reconstruction eff.} = \frac{\text{Number of reconstructed}J/\psi}{\text{Number of input}J/\psi}. \tag{2.15}$$

If this factor is higher, larger data sample (J/ψ) can be obtained over a given beam time. It is clearly seen from the Table. 2.4 that as efficiency increases the S/B ratio decreases. On the other hand, for stringent cuts, although S/B ratio increases, corresponding efficiency decreases. Thus, one has to compromise between J/ψ reconstruction efficiency and S/B ratio. For central $Au+Au$ collisions at 25A GeV, the optimized cut value corresponding to S/B = 0.84 and J/ψ reconstruction eff. = 16.20% are: No. of MUCH hits $\geq$ 16; No. of STS hits $\geq$ 7; χ^2 of the vertex $\leq$ 2.0; χ^2 of the MUCH tracks $\leq$ 2.0 (See Fig. 2.24).

MUCH-hits	STS-hits	χ^2 (Vertex)	χ^2 (MUCH)	Efficiency (%)	S/B ratio
	8			1.87	1.17
	7			2.09	0.78
18	6	1.5	1.5	2.10	0.67
	5			2.11	0.61
	4			2.11	0.59
	7	1.5	1.5	3.10	0.78
	7	2.0	2.0	13.35	0.84
	7	2.0	2.5	19.14	0.81
	7	2.0	3.0	20.50	0.70
17	7	2.5	2.0	13.48	0.68
	7	2.5	2.5	19.33	0.65
	7	2.5	3.0	20.70	0.54
	7	3.0	2.0	13.52	0.58
	7	3.0	2.5	19.38	0.55
	7	3.0	3.0	20.76	0.46
	7	1.5	1.5	3.49	0.81
	7	**2.0**	**2.0**	**16.20**	**0.84**
	7	2.0	2.5	22.90	0.79
	7	2.0	3.0	24.61	0.66
16	7	2.5	2.0	16.20	0.68
	7	2.5	2.5	23.14	0.62
	7	2.5	3.0	24.85	0.50
	7	3.0	2.0	16.25	0.59
	7	3.0	2.5	23.20	0.55
	7	3.0	3.0	24.93	0.44
	7	1.5	1.5	4.73	0.19
	7	2.0	2.0	21.18	0.20
	7	2.0	2.5	30.32	0.17
	7	2.0	3.0	32.73	0.15
15	7	2.5	2.0	21.40	0.16
	7	2.5	2.5	30.61	0.13
	7	2.5	3.0	33.03	0.11
	7	3.0	2.0	21.46	0.14
	7	3.0	2.5	30.70	0.12
	7	3.0	3.0	33.12	0.10

Table 2.4 Optimization of various parameters for the reconstruction of J/ψ.

Along with central collisions, a study has also been performed for minimum biased $Au+Au$ collisions at 25A GeV. The normalized invariant mass spectra of both signal and background are shown in Fig. 2.25. By applying the optimized set of cuts, the S/B ratio and J/ψ reconstruction efficiency are found to be 16.93 and 15.3 % respectively.

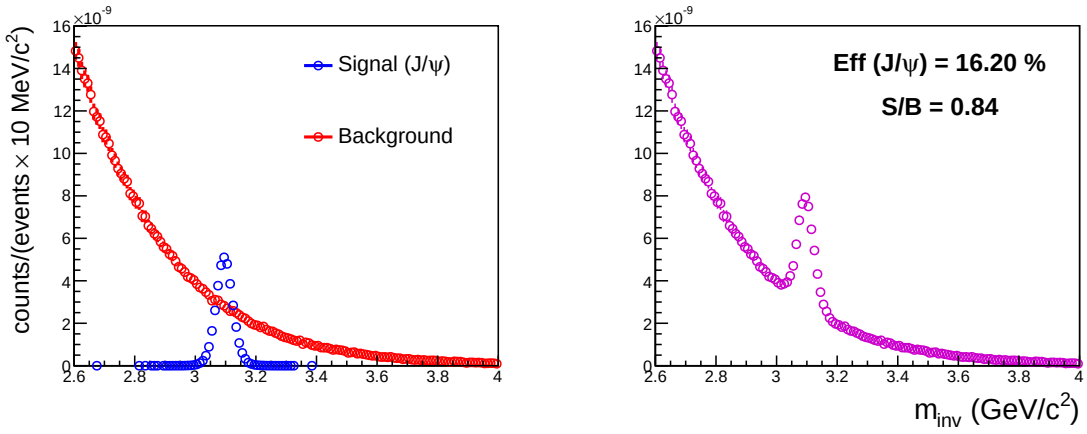

Fig. 2.24 For central collisions, Left: Signal (J/ψ) and combinatorial background. Right: Signal superimposed upon the background.

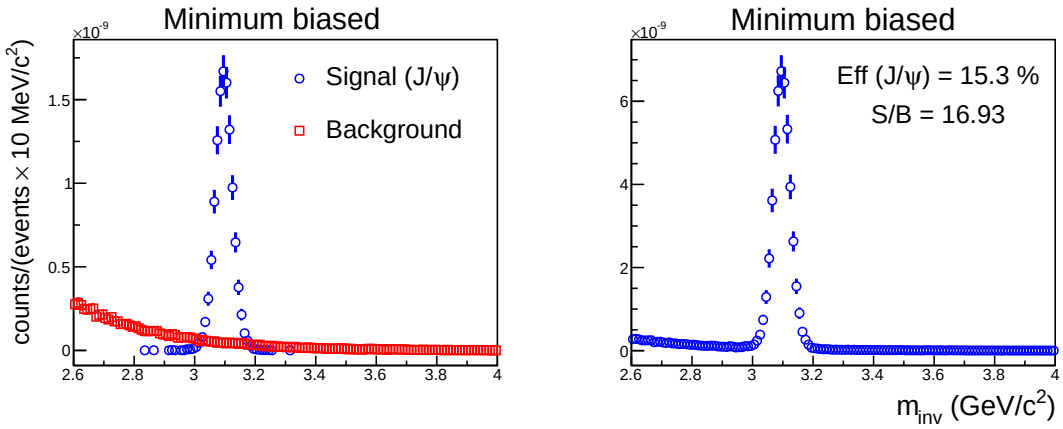

Fig. 2.25 For minimum biased collisions, Left: Signal (J/ψ) and combinatorial background. Right: Signal superimposed upon the background.

Further, the mass resolution of J/ψ which comes out to be 28.7 MeV/c^2, is far better than the previous muon detection experiments like NA50 and NA60. Moreover, it is even better than the muon spectrometers of the ongoing CMS and ALICE experiment (Pb+Pb collision at $\sqrt{s} = 2.76$ TeV) whose J/ψ mass resolution in the di-muon channel are found to be 39 MeV/c^2 [131] 78 MeV/c^2 [132] respectively. Thus, the MUCH detector with the mass

resolution mentioned above can easily measure the ψ(2s) as well, since the mass difference between J/ψ and its higher excited state ψ(2s) is 589.7 ± 1.2 MeV [96].

Fig. 2.26 illustrates the acceptance plot of both input (4π) and reconstructed J/ψ. From the right panel of Fig. 2.26 it is clearly seen that most of the phase space of J/ψ (including mid-rapidity) can be reconstructed with the proposed MUCH set-up. Thus, the proposed set-up can be used to perform the rapidity dependent study which was earlier impossible due to the absence of large acceptance detector.

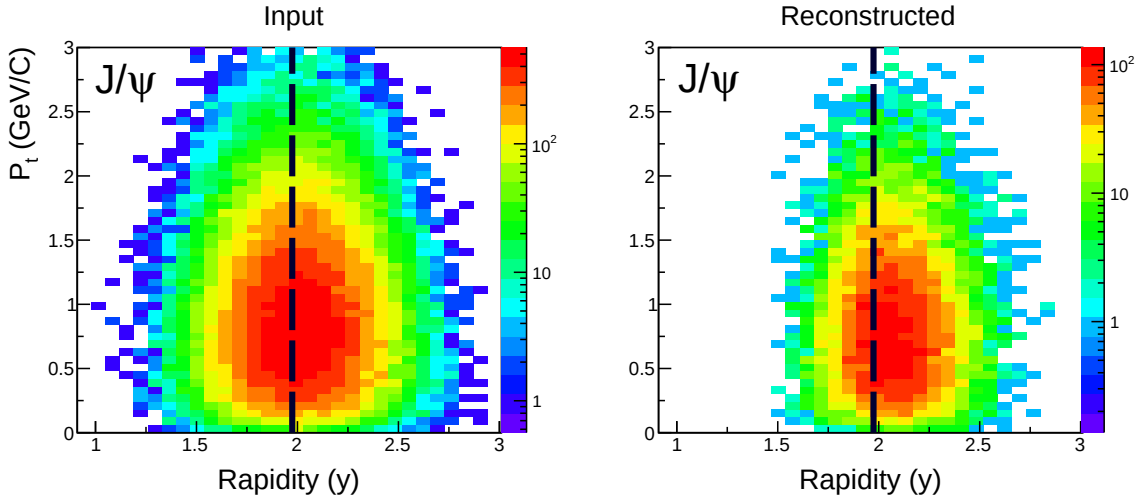

Fig. 2.26 y-pt distribution of both input and reconstructed J/ψ for central $Au+Au$ collision at 25A GeV. The vertical dashed line indicates the mid-rapidity at 25A GeV.

S/B ratio estimation using Time-of-Flight (TOF) detector

The S/B ratio can further be improved by using the additional information from the time-of-flight (TOF) along with MUCH. The punched through hadrons e.g. pions, kaons and protons can easily be identified by using TOF detector.

If L denotes the distance of the TOF wall from the target, then the velocity β of a particle of mass m can be calculated if the time t to reach the TOF detector can be precisely measured

-

$$\beta = \frac{L}{c \times t} \tag{2.16}$$

Once velocity β and momentum p is known, the mass can be calculated using the usual relativistic mechanics.

$$\beta = \frac{p}{\sqrt{p^2+m^2}} \tag{2.17}$$

$$\therefore m^2 = p^2(\frac{1}{\beta^2} - 1) \tag{2.18}$$

By identifying the punched through pions, kaons, protons etc. and by applying a cut on the mass, significant amount of background can be removed which might finally yield a better S/B ratio.

Keeping this in mind, a simulation has been performed where TOF detector is placed downstream the muon detector (MUCH) as shown in Fig. 2.27. The usual m^2 vs momentum plots, both for signal muons and backgrounds using TOF detector, are shown in Fig. 2.28 and 2.29 respectively. It is clearly seen from the left panel of both the figures that the background is mostly dominated by secondary decayed muons and very small traces of other hadrons like kaons, pions and protons are there. A cut of quadratic nature of the form ax^2+bx+c has been given to remove the background from the signal as shown in Fig. 2.28 and 2.29. The only difference between the figures is in the magnitudes of the cut value. The details of the cut value along with the reconstruction efficiency and S/B ratio is illustrated in the Table. 2.5. It is readily seen from the table that, due to the inclusion of TOF although a slight reduction of signal efficiency is there, yet, the S/B ratio increases considerably.

Cut	Functional form of the cut	efficiency (%)	S/B
No TOF cut	...	16.20	0.84
TOF cut 1	$0.014\mathrm{p}^2 - 0.076\mathrm{p} + 0.123$	15.96	0.97
TOF cut 2	$0.006\mathrm{p}^2 - 0.017\mathrm{p} + 0.021$	16.0	0.96

Table 2.5 Details of various TOF cuts applied for the background reduction. Here, p represents the longitudinal momentum.

2.5 Summary

One of the objectives of CBM experiment is to detect both J/ψ and Low mass Vector Mesons (LMVM) from their decay through the di-muon channel. It is, therefore, necessary to design a detector which is capable of measuring both high and low momentum muons. Thus a

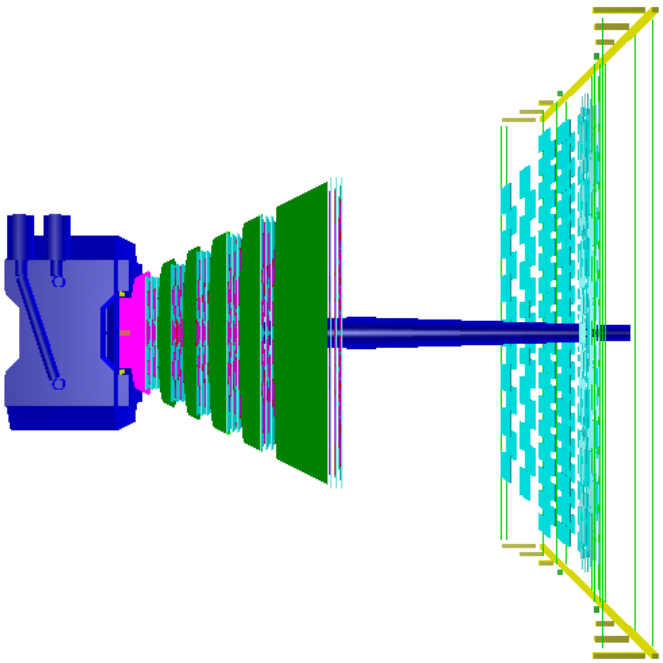

Fig. 2.27 The schematic illustration of the detector set-up needed for the measurement of J/ψ in the SIS-300 configuration. The set-up consists of dipole magnet, STS (not shown), MUCH (6 stations + 18 tracking chambers) and TOF.

study on the feasibility of J/ψ measurement in the di-muon channel by designing a muon detector for the FAIR-CBM experiment is essential. The design of the proposed MUon CHamber (MUCH) is unique in the sense that unlike other previous and ongoing heavy ion experiments (NA50, NA60, CMS etc.), here in case of CBM experiment, the absorber is sliced and tracking chambers are placed in between so that both softer and harder muons can be measured.

A detailed simulation has been performed using a realistic detector set-up. FairRoot and CbmRoot are the tools used extensively for the simulation. A thermal model has been used for the generation of signal (J/ψ), while the background generation is realized using UrQMD event generator. The generated particles have been transported through the detector set-up with the help of GEANT3 transport engine. The optimized detector set-up comprises of 6 absorbers and $6 \times 3 = 18$ detector layers. The first absorber is 60 cm thick and is made of carbon while the rest of the absorbers are made of iron with thicknesses 20 cm, 20 cm, 30 cm, 35 cm, and 100 cm each. As far as the detector technology is concerned, which need to be both fast and radiation hard due to the unprecedented interaction rate of CBM experiment, the Gas Electron Multiplier (GEM) is chosen. In order to have a realistic detector response, segmentation and digitization have been performed by taking the GEM as the active detector

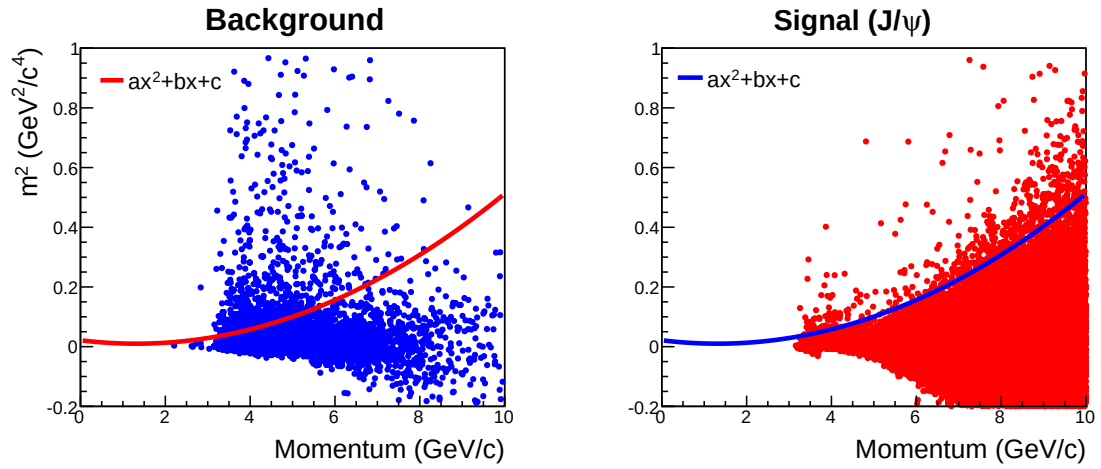

Fig. 2.28 m^2 vs momentum plot both for signal muons and backgrounds. The solid line is the proposed cut (see TOF cut 1 in Table. 2.5) for the reduction of background.

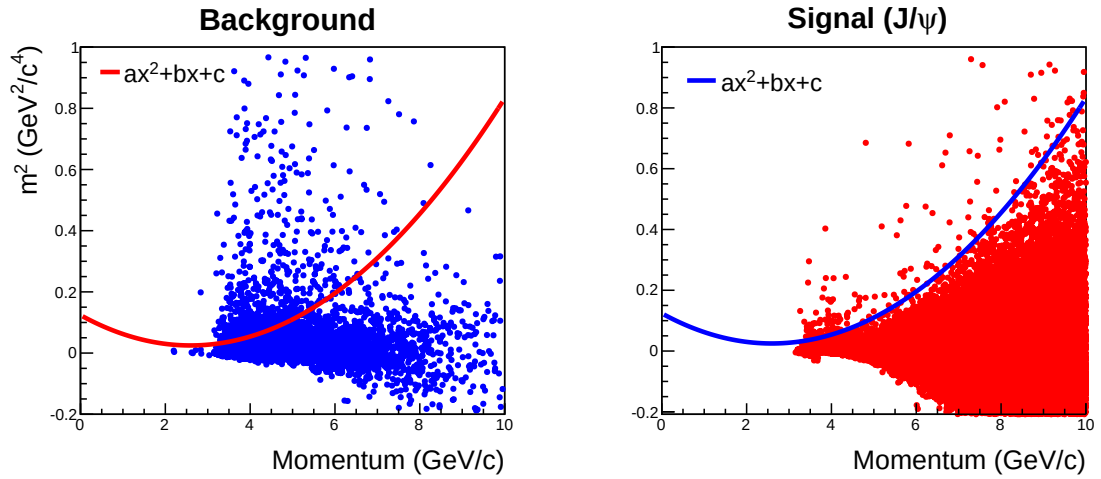

Fig. 2.29 m^2 vs momentum plot both for signal muons and backgrounds. The solid line is the proposed cut (see TOF cut 2 in Table. 2.5) for the reduction of background.

consisting of Argon gas. 1^0 segmentation angle and LMF deconvolution algorithm are found to be the better choice for maximum signal efficiency. Track reconstruction algorithm in MUCH is based on Kalman filter technique which uses the already reconstructed STS tracks (by Cellular automation) as input. The single track efficiency in case of MUCH is observed to be more than 95%. The global tracks are finally reconstructed by matching the STS and MUCH track segments and extrapolated the resulted track to the interaction vertex. The global track thus formed undergoes several quality checks based on (a) the number of STS hits, (b) the number of MUCH hits, (c) the χ^2 of MUCH track and (d) the χ^2 vertex. Those tracks which pass the aforesaid criteria are considered as muon candidates for di-muon analysis. Dimuon analysis is based on invariant mass technique. Signal has been reconstructed by combining oppositely charged muon candidates from the same event. The superevent technique has been used to reconstruct background, where the oppositely charged uncorrelated muon candidates (from different events) have been combined. The S/B ratio is calculated by extracting both signal and background around the $\pm 2\sigma$ window of the signal peak. The cuts have been optimized in terms of signal reconstruction efficiency and S/B ratio. The S/B ratio and J/ψ reconstruction efficiency for central Au + Au collisions are observed to be 0.84 and 16.20% respectively. The same for the minimum biased collisions are respectively found to be 16.92 and 15.2%. For both the cases, the J/ψ peak is clearly visible and is above the exponential background. The inclusion of TOF significantly improves the S/B ratio. The results obtained from the present simulation study is thus conclusive enough to state that the measurement of J/ψ is possible using the proposed MUCH detector for the FAIR-CBM experiment.

3

Extraction of fireball temperature from dilepton spectra

3.1 Introduction

One of the main objectives of the Compressed Baryonic Matter (CBM) experiment to be held at GSI, Germany is to realize the QGP-hadron phase transition by colliding heavy ions [32–35]. To realize this phase of strongly interacting matter i.e. QGP, a comprehensive set of observables will be measured with utmost precession over the wide range of beam energies [32–35]. In addition to other observables, the dilepton measurement is also one prime objective of the CBM experiment [133]. The dileptons decayed from J/ψ and other intermediate mass vector mesons are believed to be the cleanest diagnostic probe to characterize the fireball created in heavy-ion collisions [14, 134]. Being color singlet (having no color charge), dileptons do not participate in strong interaction and hence refrain themselves from interacting with the strongly interacting medium created in heavy-ion collisions. Thus, dileptons provide undistorted information of the interior of the fireball. It is suggested that due to the partial restoration of chiral symmetry at the QGP phase, in-medium modification of inherent properties such as mass modification and collisional broadening of vector mesons may take place [135–138]. Out of all low mass vector mesons (LMVM), ρ^0 is believed to

be the best candidate for measuring any sizable effect if the chiral symmetry is restored by some means. The life-time of ρ^0 is very small ($\tau_\rho \sim 1.3$ fm/c) [139] and hence decay within the fireball. Thus, properties of ρ^0 will bound to modify, if QGP is produced at the early stage of heavy-ion collision and the effect will be visible if one measures and study their spectra in greater details. On the other hand, in the intermediate mass region, the thermal electromagnetic radiation decaying into dilepton pair reflects the temperature of the fireball. Hence, its study can provide the thermodynamic condition of the interior of the fireball [139]. Moreover, the study of dileptons decaying from J/ψ can provide all important information regarding the suppression of the later which was suggested to be one of the smoking-gun signature for the formation of QGP [66].

The CBM experiment at FAIR is expected to address all of the above issues by scanning dilepton spectra starting from LMVM upto charmonia both in SIS100 and SIS300 configuration [133]. In CBM experiment, the RICH (Ring Imaging Cherenkov Detector) and the MUCH (Muon Chamber) detectors will be used for the detection of dielectrons and dimuons respectively decayed from these LMVM and J/ψ. Even though the prime objective of measurement of these dileptons is to realize QGP looking at the J/ψ suppression, an attempt will also be made to estimate temperature of the fireball from invariant m_T spectrum of the reconstructed J/ψ using these dimuons. A feasibility study of precise determination of temperature of the fireball with the MUCH setup (by detecting the J/ψ and other LMVM decayed muons) is of utmost importance. In this chapter, an attempt has therefore been made to study the sensitivity of MUCH for measuring temperature of the fireball from the transverse mass distribution of dimuons.

3.2 Transverse mass distribution and effective temperature

Transverse mass (or momentum) distribution is one of the usual prescription for studying high energy collisions or multiparticle production. Since the transverse motion is believed to be generated only during collisions and hence transverse mass is sensitive to the dynamics of heavy-ion collisions [140]. Transverse mass (m_t) is defined as,

$$m_t = \sqrt{p_t^2 + m^2}, \tag{3.1}$$

where, p_t and m respectively represents the transverse momentum and rest mass of the particle considered.

The multi-particle production in high energy collisions can be explained with the help of statistical mechanics [141]. Hagedron, in his seminal work showed that, single particle

energy distribution in the local rest frame of hadronizing matter follows Boltzmann form [141, 142],

$$\frac{dN}{dp} \sim \exp\left(-\frac{E}{T}\right), \tag{3.2}$$

where, $E = \sqrt{m_t^2 + p_z^2} = m_t \cosh y$ is the hadron energy and T is common (for all particles) temperature and y represents the rapidity of the particle. In the approximation $m_t \gg T$, the above equation in terms of transverse mass can be written as,

$$\frac{1}{m_t}\frac{dN}{dm_t} \sim \exp\left(-\frac{m_t}{T}\right). \tag{3.3}$$

For a dynamically evolving system, as time elapses, the temperature of the system generally begins to fall. A part of the thermal energy of the system is spent for the development of collective flow [143]. The collective flow in heavy-ion collision is believed to be generated due to the secondary collisions or rescattering among the produced particles [140]. Thus, for a dynamically evolving system or for an expanding fireball the above equation (3.3) is modified to the following form,

$$\frac{1}{m_t}\frac{dN}{dm_t} \sim \exp\left(-\frac{m_t}{T_{eff}}\right), \tag{3.4}$$

where, T_{eff} is known as effective temperature (or slope parameter). The effective temperature contains the information of both freeze-out temperature and collective flow. The effective temperature (T_{eff}) is related to the actual kinetic freeze-out (T_{fo}) temperature by the following relation [140],

$$T_{eff} = T_{fo} + m\langle v_T\rangle^2, \tag{3.5}$$

where, $\langle v_T\rangle$ represents the average collective velocity. This is to be emphasized that below the kinetic or thermal freeze-out temperature (T_{fo}), the elastic scattering between the produced particles ceases.

The dileptons play the central role in this chapter. In this context, a brief discussion on the possible sources of dileptons in heavy-ion collisions is put forward.

3.3 Sources of dilepton

Along with photons, the dileptons are emitted from different stages of heavy-ion collisions [144]. Dileptons with an additional degree of freedom i.e. invariant mass M, over the photons, can be used to disentangle their different production sources [144]. A typical dilepton invariant mass distribution is shown in Fig. 3.1. Dileptons appear both in hadronic and QGP phase. A brief description of various dilepton sources are shown as in the following.

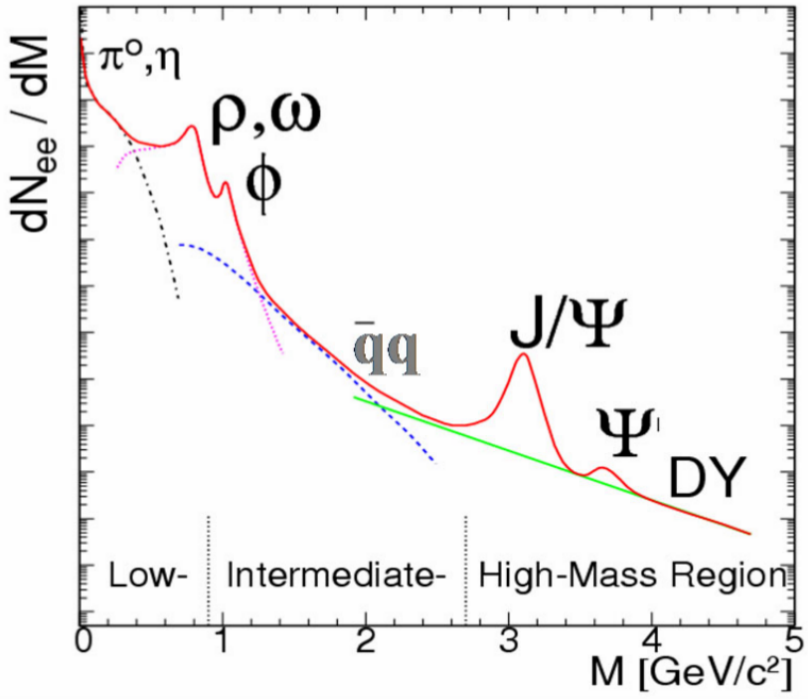

Fig. 3.1 A typical invariant mass spectrum of the dilepton. As seen from the figure, the low mass region is contributed by η, π^0, ρ, ω and ϕ, while the intermediate mass region dominated by the $D\bar{D}$ and $q\bar{q}$ annihilation, and the high mass region is due to J/ψ, and ψ' [145].

3.3.1 Partonic source

The dileptons created from the partonic interactions in the QGP phase are termed as thermal dileptons. These dileptons provide its contribution to the intermediate mass region (IMR) ($1 < M < 3$ GeV/c^2) of the dilepton invariant mass spectra. Thermal dilepton production mechanisms correspond to a combination of two and three-body processes viz. $q\bar{q}$ annihilation: (i) $q+\bar{q} \rightarrow l^+ + l^-$, (ii) $q+\bar{q} \rightarrow g+l^+ + l^-$ and Compton scattering: (i) $q+g \rightarrow q+l^+ + l^-$, (ii) $\bar{q}+g \rightarrow \bar{q}+l^+ + l^-$ [144]. The contribution of dileptons to the IMR of the dilepton

invariant mass spectra is therefore believed to be continuous. The Feynman diagrams of dilepton production processes are shown below [144],

Fig. 3.2 Feynman diagrams showing different dilepton sources in the QGP scenario [146].

3.3.2 Hadronic sources

At the low invariant mass regime (M $<$ 1 GeV/c^2), there exists two possible sources of dileptons: (a) the direct decay of LMVM (ρ, ω and ϕ), and (b) Dalitz decay of various mesons and baryons (π^0, η, Δ, ..) [144]. The direct decay of a low mass vector meson into dileptons is a two-body process and thus the invariant mass distribution exhibits distinct peaks. On the other hand, the contribution of Dalitz decay, which is a three-body decay, to the dilepton invariant mass distribution is continuous. The study of low mass dilepton is important in the sense that it can be used to investigate the hadronic in-medium properties - such as mass modification and collisional broadening of the LMVM, which are considered as the unambiguous signatures of Quark Gluon Plasma phase [135–138, 147].

At the intermediate mass regime (1 $<$ M $<$ 3 GeV/c^2), the contribution to the dilepton invariant mass spectra is coming both from (a) the dilepton decay of the correlated $D\bar{D}$ pairs, and (b) the multi-meson reaction channels ($\pi+\pi$, $\pi+\rho$, $\rho+\rho$, ..) [144].

On the other hand, the high invariant mass region (M $>$ 3 GeV/c^2) which corresponds to the early stage emission, is subjected to two major sources of dileptons which are: (a) direct decay of high mass vector mesons (J/ψ, ψ', ..), and (b) the hard Drell-Yan processes ($q+\bar{q} \rightarrow l^+ + l$), where $l = e, \mu$ [144]. The Drell-Yan process is an electromagnetic process which refers to the creation of dilepton pair from the initial hard collisions between a quark and an anti-quark arising from a pair of interacting hadrons.

3.4 Experimental measurement of dilepton

The dilepton spectra was measured by various heavy-ion experiments [45]. The first measurement was done at the BEVALAC [148] ($E_{lab} \simeq$ 1-5A GeV) by the DLS collaboration. They measured the dilepton spectra at the low-mass region (M $\leq$ 1 GeV) for various combination of light, medium and heavy nuclei (from p+p to Ca+Ca) [149, 150]. HADES experiment

measured dileptons for C+C collisions at 2A GeV [151]. At comparatively higher energies (ultra-relativistic energies), dilepton spectra was also measured by the HELIOS-3 [152], NA50 [153], CERS/NA45 [154, 155] and NA60 [156] collaborations at CERN-SPS. Out of many, the most remarkable results obtained by NA60 collaboration are summarized below.

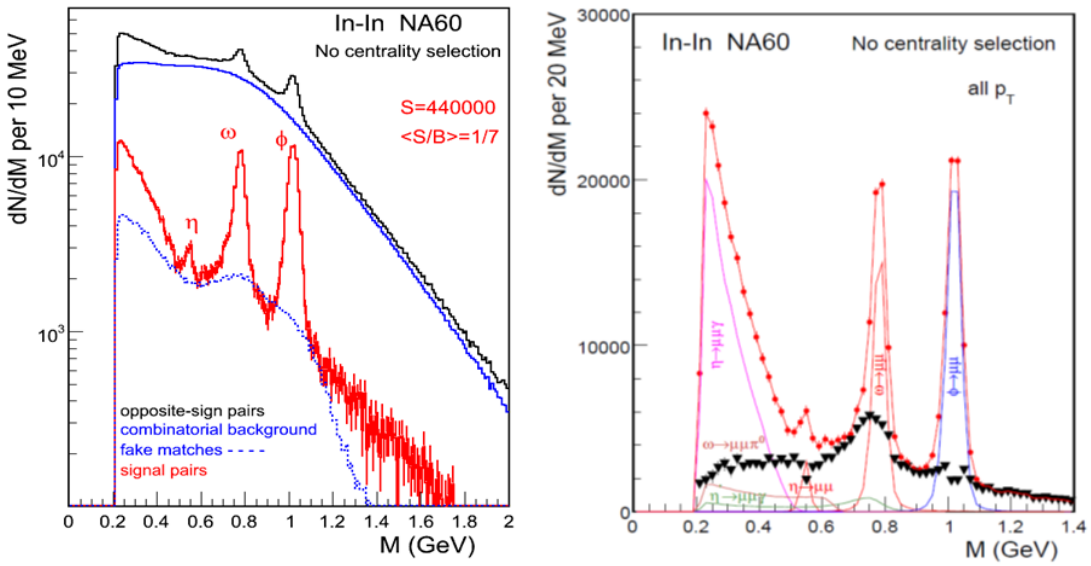

Fig. 3.3 Invariant mass distribution of dimuon measured by NA60 collaboration for In + In collisions ate 158A GeV. Left: The opposite sign dimuons along with the combinatorial background (black solid line), like-sign dimuon pairs (blue solid line), the fake matches (blue dashed line), signal pairs (red solid line). Right: the magnified version of the same diagram: signal pair (red dots), the black lower triangles represents the excess yield i.e having unknown origin [139].

NA60 collaboration reported an excess of muon pairs with respect to the predicted yield both at low as well as at the intermediate mass region ($1 < M < 2.5$ GeV/c^2) at 158A GeV In+In collisions [139]. Fig. 3.3 shows the invariant mass distribution calculated from the dimuons in In+In collision at 158A GeV. The upper black solid line represents the opposite-sign dimuons along with the combinatorial background. The blue solid and dashed line represents the like-sign muon pairs and fake matches respectively. The red solid line, on the other hand, represents the signal muon pairs obtained on subtraction of the fake matches and like-sign muon pairs (combinatorial background). The right panel of Fig. 3.3 shows the same diagram in linear scale where the red dots represents the signal pairs. The black lower triangles in that figure represents the residual spectra (or excess dimuons) after subtraction of the cocktail of known dimuon sources (e.g. ϕ, ω, η and the Dalitz decays) from the signal muon pairs. Thus, the black lower triangles represents the unknown excess yield and its study

becomes an important task. It is to be noted that since ρ contribution was not subtracted from the signal pairs, the excess yield contains the contamination of ρ mesons [139].

The above form of excess dimuon yield (the black lower triangles in the right pannel of Fig. 3.3) can only be explained by taking care of the in-medium modification of ρ meson along with the other contributions [94]. The theoretical calculation was performed by Rapp *et al.* [137, 138, 147] in an expanding fireball model with an inbuilt phase transition. Further, it has been argued that the effect of the coupling of ρ mesons with baryons will be more at the FAIR energy domain, where the baryon density could be something of the order of 5-7 times the normal nuclear matter density [45]. Due to the exceptional mass resolution of MUCH (as discussed in Chapter 2), the CBM is the best suited experiment to pin-down the aspect of chiral symmetry restoration by measuring the ρ meson from the dimuon channel.

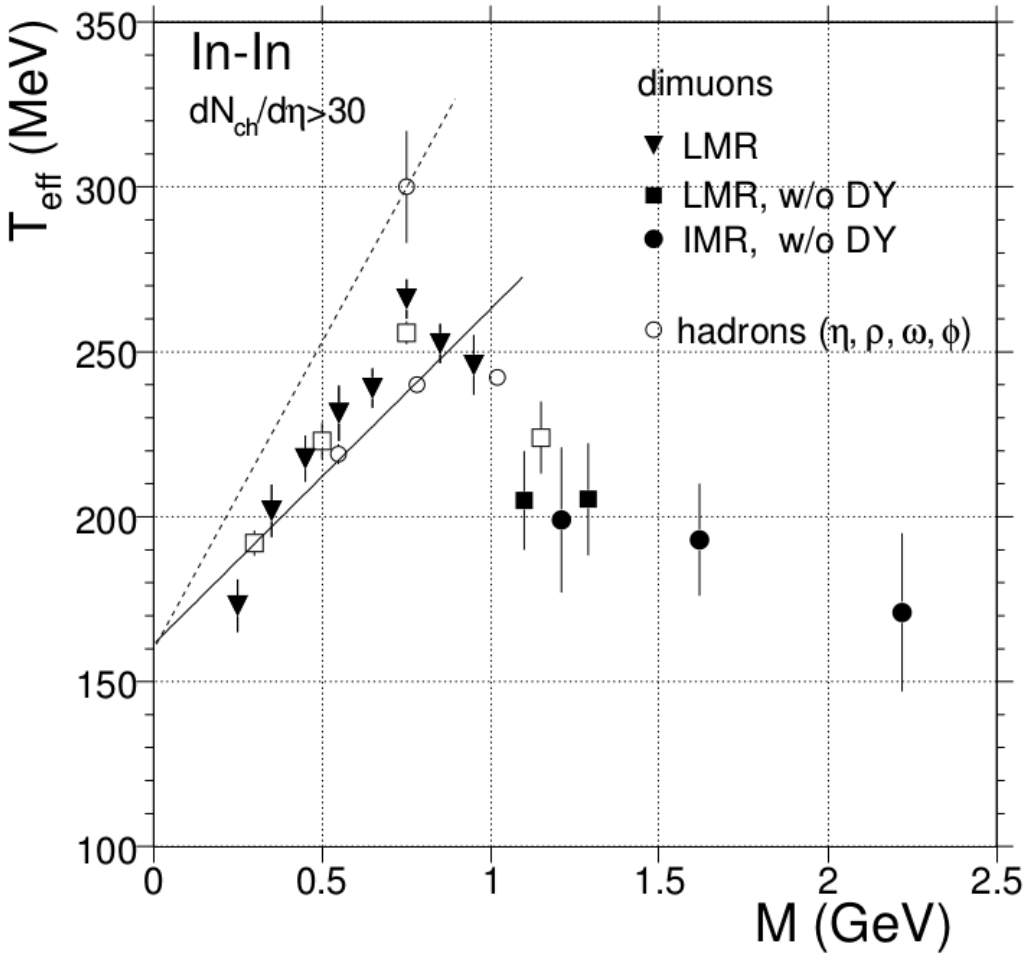

Fig. 3.4 The inverse slope parameter or effective temperature of the excess dimuons as a function of dimuon mass for In + In collisions at 158A GeV [139].

NA60 collaboration also measured the transverse mass distribution of those excess dimuons (without Drell-Yan processes) [139]. They reported that the transverse mass distribution of these excess dimuons can be well-described by exponential function (i.e. Boltzmann distribution) and thus they might have a thermal origin [157]. The effective temperature calculated from an exponential fit of the excess dimuon transverse mass spectra has been plotted as a function of invariant mass as shown in Fig. 3.4.

In low mass region, the effective temperature increases with dimuon invariant mass. The increase of effective temperature with dimuon mass could be due to the development of strong radial flow in the late phase of the collision [139]. On the other hand, at the intermediate mass range, the effective temperature drops quite significantly with dimuon mass. This remarkable observation suggests that above 1 $\mathrm{GeV/c^2}$, the emission source of thermal dimuons is largely partonic in origin, when radial flow has not yet built up [139]. The above finding of the NA60 collaboration could be verified at lower energies with much more precession with the help of the forthcoming CBM experiment.

3.5 Results and discussion

3.5.1 Details of present analysis

The present work has been carried out at the laboratory beam energy of 10*A* GeV central $Au+Au$ collisions within the `CBMROOT` framework. The `JAN12` and `JULY14` versions of the external package and `CBMROOT` respectively are used for the present investigation. As usual, UrQMD-3.4 is chosen for the generation of background, while for the signal generation PLUTO event generator is used. A brief description of `CBMROOT`, external package, UrQMD and PLUTO have already been provided in Chapter 2. Although in `CBMROOT` framework both `GEANT3` and `GEANT4` transport engines are available, in the present work `GEANT3` is explicitly used for the transportation of generated particles through the detector set-up. The standard SIS-100b geometry (with 5-absorbers) is employed for the present study. In the standard SIS-100b geometry, the first absorber is made of carbon and the rest are made of iron. The carbon absorber is 40 cm thick and partly lies within the dipole magnet while the remaining four iron absorbers are of 20 cm, 20 cm, 30 cm and 135 cm thick respectively. The detector triplets are inserted in between the absorber layers to facilitate momentum dependent muon identification. The distance between the successive absorber and the detector layers are fixed to 5 cm, while the distance between the individual detector layers are fixed to 10 cm. The schematic view of the SIS-100b geometry is illustrated in Fig. 3.5. An important ingredient of the geometry is the beam pipe and its shielding. Beam pipe shielding is generally necessary

in order to suppress the unwanted background particles (mostly δ or knock-out electrons) that might be created due to the interaction of beam particles with the beam pipe. The newly optimized beam pipe and its shielding [158] are used for the present course of simulation. The salient feature of the present design of the beam pipe and its shielding are as follows: the entire beam pipe is made of Aluminum (Al), except for the region z = 120 - 180 cm, where beam pipe itself is made of lead and might act like a shielding. It is to be mentioned that the entire beam pipe is made conical in shape and thus for obvious reason its shielding also requires a conical geometry. In the present scenario, the angle of Pb-shielding is made 2.9^0 - 5.7^0. For the second station onwards, the shielding is made up of iron only. It is to be noted that, by virtue of segmented hadron absorber, the present detector set-up can be used both for the measurement of soft and hard muons. This feature contrasts this detector from the other existing muon detectors, which uses a single thick hadron absorber in order to stop the hadronic background. This is to be emphasized that, in the present scenario, the momentum of the charged particles will be measured at STS which lies upstream MUCH and thus ensures better momentum resolution.

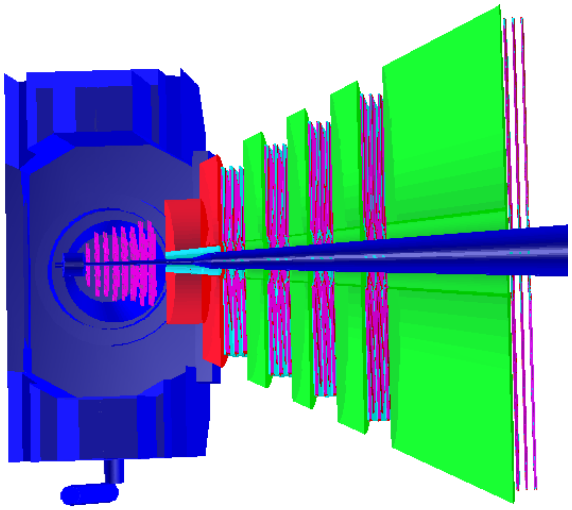

Fig. 3.5 Schematic view of MUCH (SIS-100b) with STS and dipole magnet. The first absorber is made of carbon (60cm) and the rest are iron (20+20+30+135).

As far as the active component of the MUCH is concerned, to account for realistic detector geometry, the readout modules are segmented in pads for obtaining final detectable response [122, 45]. It has already been shown in Chapter 2 as well as in the Ref. [122] that 1^0 segmentation scheme with local maxima finder as the cluster deconvolution algorithm results better hit-finding efficiency and lesser background reconstruction and thus 1^0 segmentation scheme and local maxima finder are chosen for the present study. The hits generated in the

above sets of conditions are used for the *tracking*. Suitable *tracking* algorithm (as mentioned in Chapter 2) is used to reconstruct the particle tracks. The reconstructed tracks are called muon candidates if they follow a set of criteria: number of MUCH hits $\geq$ 16, number of STS hits $\geq$ 7, χ^2 of the vertex $\leq$ 2.0, and χ^2 of the MUCH tracks $\leq$ 2.0. These muon candidates are then selected for *dimuon analysis* where invariant mass technique (described in Chapter 2) is applied to reconstruct J/ψ. The combinatorial backgrounds are reconstructed in the present analysis with the help of *super event* analysis technique (as discussed in Chapter 2). The reconstructed J/ψ along with the combinatorial background are shown in Fig. 3.6 (left). Figure 3.6 (right) represents the y-p_T acceptance plot of both input and reconstructed signal. It is clearly understood from the figure that the entire forward rapidity hemisphere along with the mid-rapidity of J/ψ can be reconstructed with present MUCH detector set-up. Thus, the present MUCH detector set-up can also be used for rapidity dependent studies.

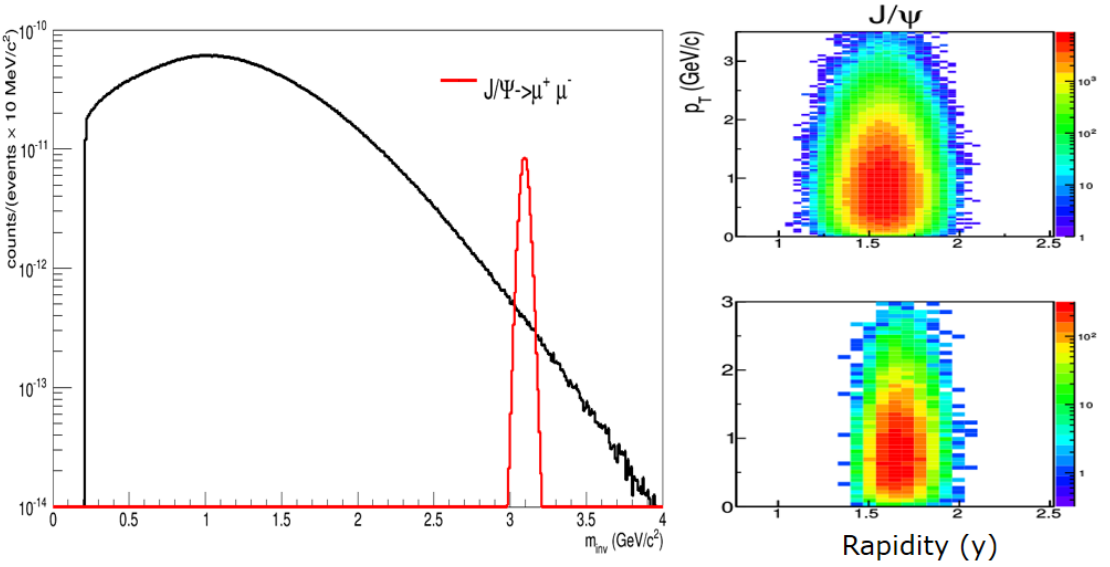

Fig. 3.6 **Left:** The reconstructed invariant mass distribution of J/ψ from the dimuon ($\mu^+\mu^-$) channel and the corresponding combinatorial background (black solid line) at 10A GeV. **Right:** A two dimensional y vs p_T plot corresponding to input (upper panel) and reconstructed (lower panel) J/ψ meson using the aforesaid MUCH detector (SIS-100b) set-up.

3.5.2 Extraction of fireball temperature

The transverse mass spectra of both input and reconstructed J/ψ are fitted by an exponential function (see eqn. 3.4) where, T_{eff} represents the slope of the transverse mass distribution. From the fitting, the slope or effective temperature T_{eff} is calculated. As expected, the fitting

parameters are found to be a function of both the fitting range and the histogram binning. The effect of both fitting range and histogram binning on the effective temperature (T_{eff}) is investigated in the following study.

Analysis of dimuon spectra ($J/\psi \rightarrow \mu^+\mu^-$)

As discussed, the high-mass region of the dilepton spectra is mainly contributed by the resonances like J/ψ, ψ' etc. But, for the present study, the dimuons coming from the decay of J/ψ is only considered. For J/ψ, three different bin widths viz. 500, 160 and 100 MeV are considered. Further, in order to see the effect of fitting range, for each case (except 500 MeV bin width) the transverse mass spectra is fitted for different range of transverse mass (m_t). The above exercise is performed for input as well as reconstructed J/ψ and is shown in Figs. 3.7, 3.8, 3.9, 3.10, 3.11, 3.12. The resulting fitting parameters with χ^2/NDF are summarized in Table 3.1. The best fitted values of T_{eff} in accordance with the best χ^2/NDF are tabulated in Table 3.2. It is clearly visible from the Table 3.2 that the effect of hadron absorber is minimum as far as the effective temperature of the fireball is concerned. The m_t spectra of J/ψ is comparatively harder and thus the presence of thick absorbers have relatively negligible effect on the transverse mass spectra and hence the value of effective temperature (T_{eff}) seems to be unaffected.

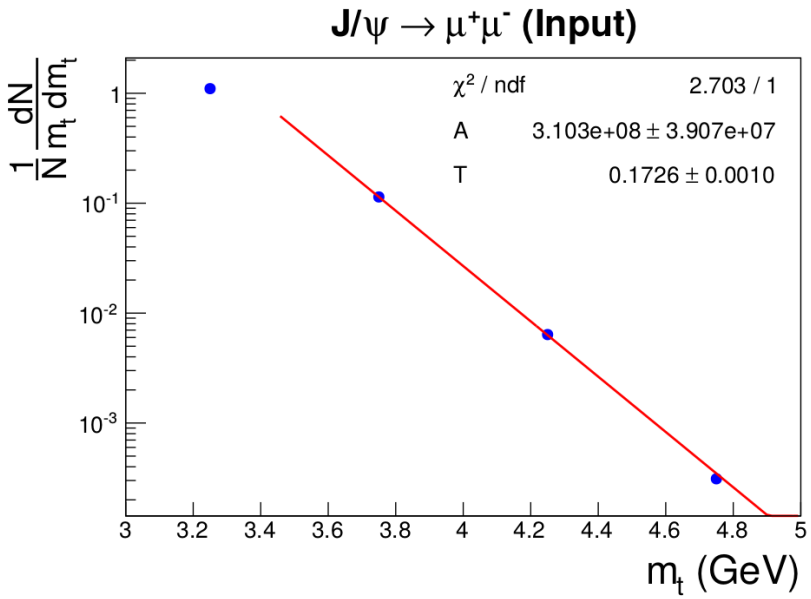

Fig. 3.7 m_t of input J/ψ at 10A GeV (from PLUTO). The solid line represents the fitting by an exponential function with bin size of 500 MeV.

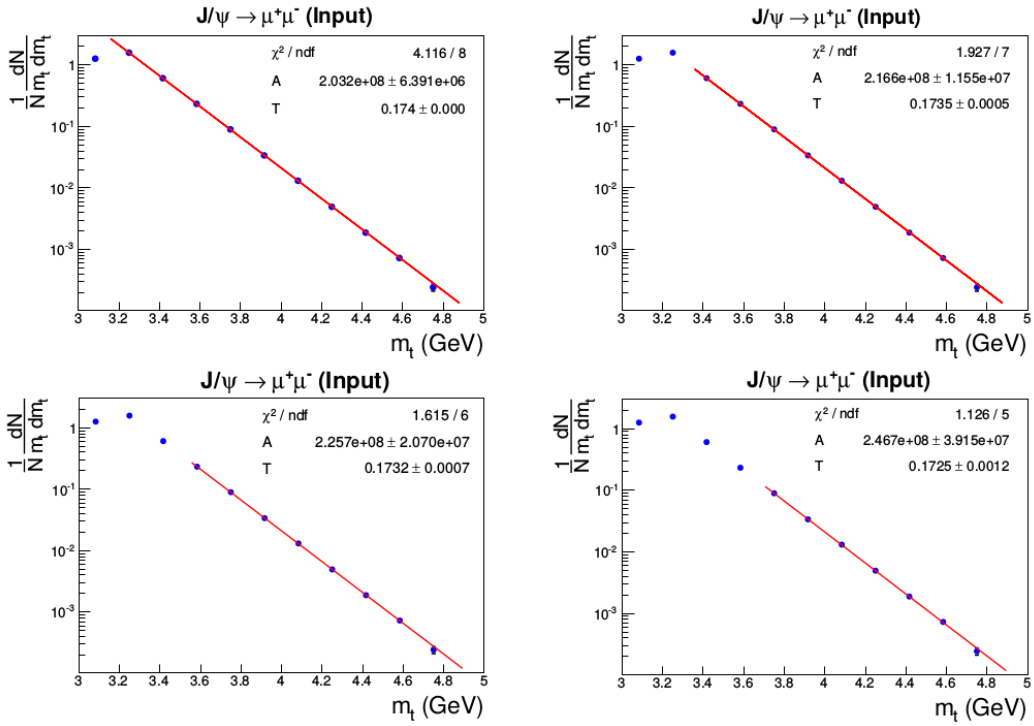

Fig. 3.8 Transverse mass spectra of input J/ψ at 10A GeV (from PLUTO). The solid line represents the fitting by an exponential function with bin size of 160 MeV for different fitting range.

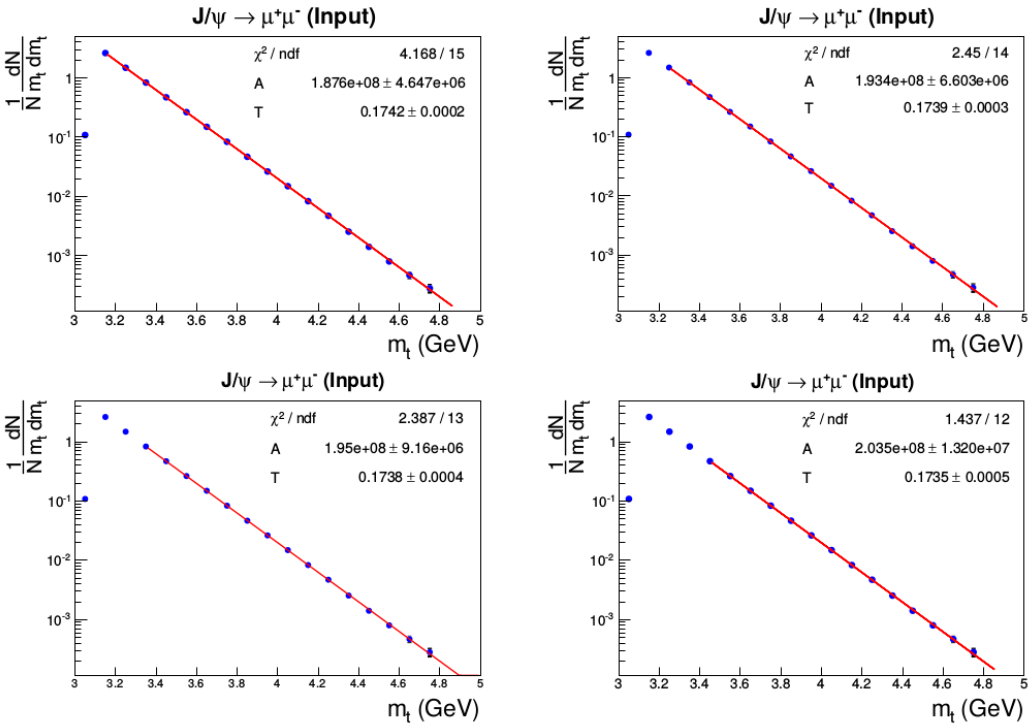

Fig. 3.9 Transverse mass spectra of input J/ψ at 10A GeV (from PLUTO). The solid line represents the fitting by an exponential function with bin size of 100 MeV for different fitting range.

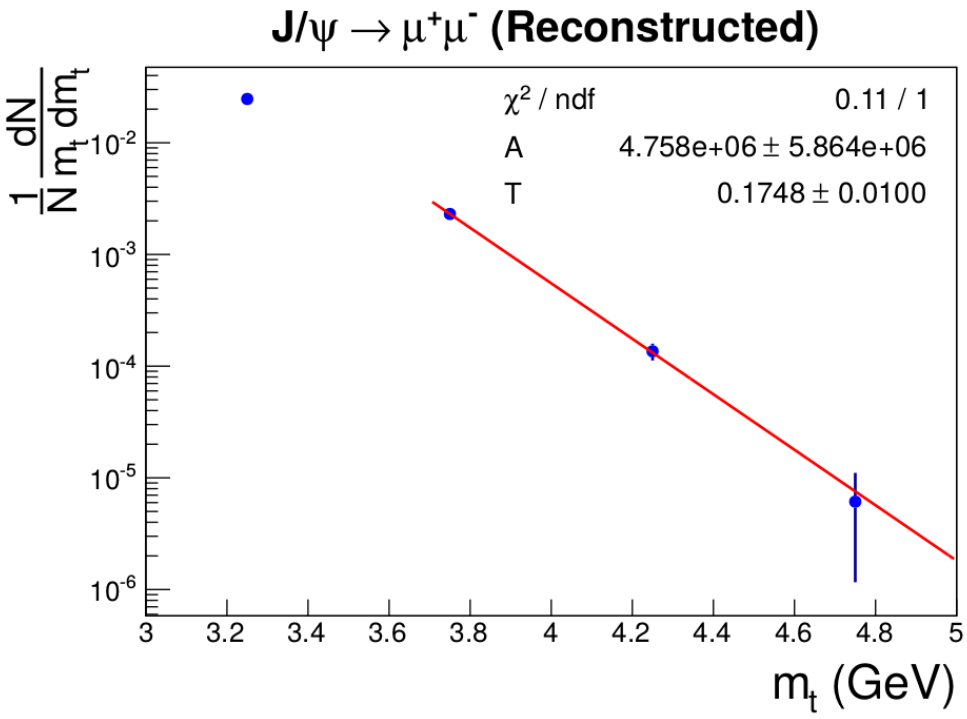

Fig. 3.10 Transverse mass spectra of reconstructed J/ψ at 10A GeV. The solid line represents the fitting by an exponential function with bin size of 500 MeV.

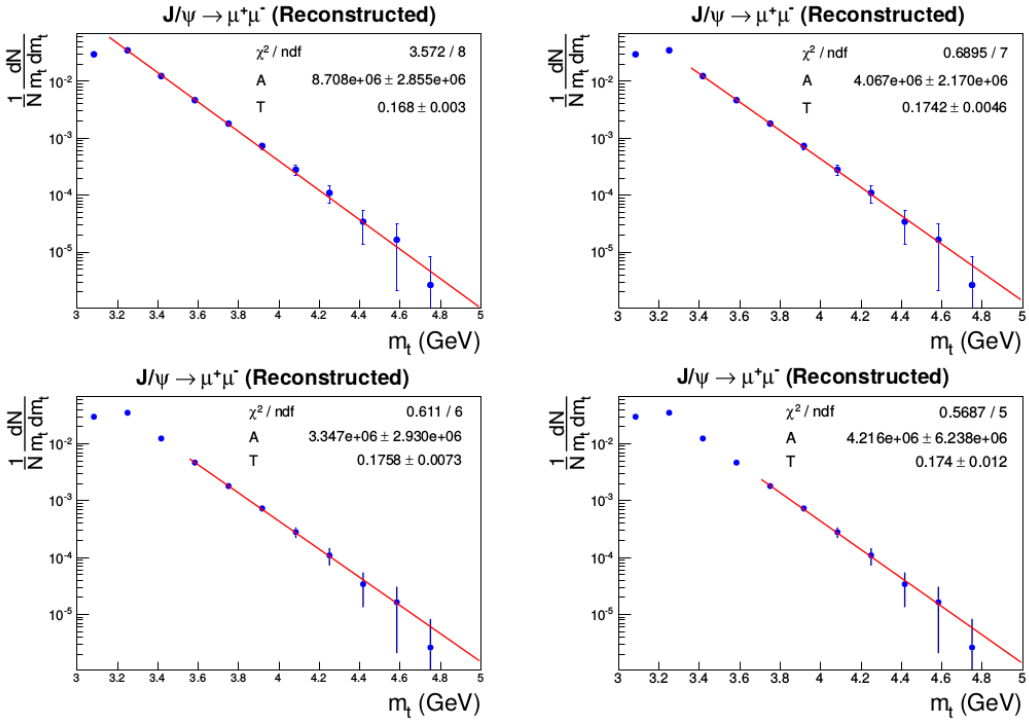

Fig. 3.11 Transverse mass spectra of reconstructed J/ψ at 10A GeV. The solid line represents the fitting by an exponential function with bin size of 160 MeV.

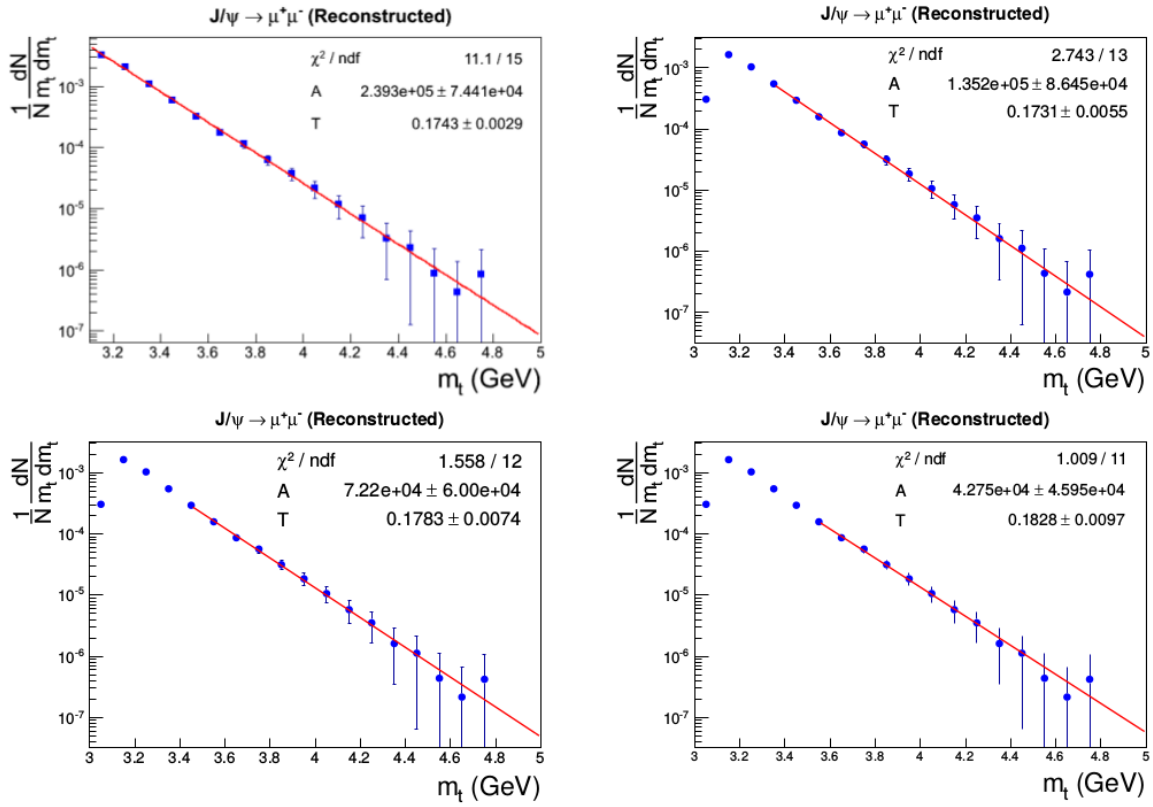

Fig. 3.12 Transverse mass spectra of reconstructed J/ψ at 10A GeV. The solid line represents the fitting by an exponential function with bin size of 100 MeV.

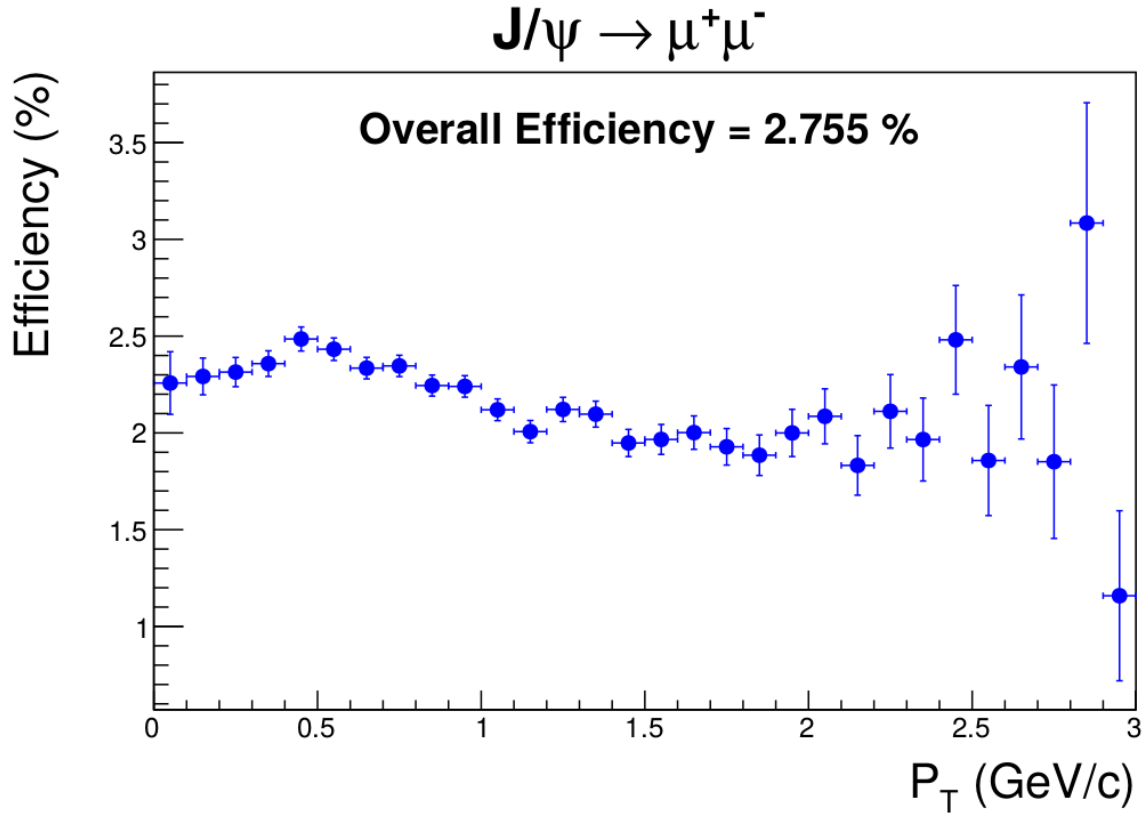

Fig. 3.13 Transverse momentum dependence of efficiency for J/ψ.

J/ψ		**Input**		**Reconstructed**	
Bin width	m_T range	T_{eff}	χ^2/NDF	T_{eff}	χ^2/NDF
500 MeV	3.43 – 4.9	172.6 ± 1.0	2.703/1	174.8 ± 10	0.11/1
160 MeV	3.10 – 4.9	174.0 ± 0.0	4.116/8	168.0 ± 3.0	3.572/8
	3.37 – 4.9	173.5 ± 0.5	1.927/7	174.2 ± 4.6	0.689/7
	3.58 – 4.9	173.2 ± 0.7	1.615/6	175.8 ± 7.3	0.611/6
	3.72 – 4.9	172.5 ± 1.2	1.126/5	174.0 ± 12.0	0.568/5
100 MeV	3.17 – 4.9	174.2 ± 0.2	4.168/15	174.3 ± 2.9	11.1/15
	3.22 – 4.9	173.9 ± 0.3	2.450/14	173.1 ± 5.5	2.743/13
	3.32 – 4.9	173.8 ± 0.4	2.380/13	178.3 ± 7.4	1.558/12
	3.42 – 4.9	172.5 ± 1.5	1.437/12	182.8 ± 9.7	1.009/11

Table 3.1 The summary of the extracted fitting parameter T_{eff} along with the goodness of the fit indicated by χ^2/NDF for J/ψ meson both for the input (from PLUTO) and the reconstructed signal at MUCH.

$J/\psi \rightarrow \mu^+\mu^-$		**Bin width (MeV)**		
		500	160	100
Input	T_{eff} (MeV)	172.6 ± 1.30	173.5 ± 0.5	173.6 ± 1.30
Reconstructed	T_{eff} (MeV)	174.8 ± 10.06	174.2 ± 4.6	182.8 ± 9.7

Table 3.2 The extracted fitting parameter i.e. temperature (T_{eff}) selected on the basis of χ^2/NDF for J/ψ meson with different m_t bin width (both for input and reconstructed signal).

Further, J/ψ reconstruction efficiency is estimated and is plotted as a function of transverse momentum. It can be clearly seen from the plot that the efficiency is independent of the transverse momentum over the entire studied range. This is because of the fact that the harder muons coming out of the decay of J/ψ are hardly absorbed by the hadron absorbers.

3.6 Summary

The dilepton spectra of J/ψ have been studied using the proposed Muon Chamber (MUCH) detector of CBM experiment. The study is performed within the `CBMROOT` framework. The signal and background are generated with the help of PLUTO and UrQMD-3.4 event generators respectively. The standard SIS-100b geometry with the newly optimized beam pipe is used for the present investigation. The optimized values of the simulation parameters with respect to efficiency and S/B ratio (as optimized in Chapter 2) are taken into consideration. In order to extract the slope parameter (T_{eff}), an exponential function (eqn. 3.4) is fitted to the input as well as reconstructed signal. To see the variation of bin width and fitting m_t-range,

for each bin width of the transverse mass spectra, different fitting ranges are chosen. The results of the fitting with the indicator of goodness of the fit i.e. χ^2/NDF are tabulated in Table 3.1. For each bin width, the best fitted T_{eff} values (i.e. with best χ^2/NDF) are tabulated in Table 3.2. The value of T_{eff} for reconstructed J/ψ is found to be in agreement with that of the input within the uncertainty indicating the usefulness of MUCH design for the CBM experiment. Moreover, from the present investigation, the observed dependence of the fireball temperature on the bin width of transverse mass is found to be well within the estimated error. Further, J/ψ reconstruction efficiency is seen to be independent of the transverse momentum over the entire studied range.

4

Separate mass scaling of the rapidity width at FAIR energies

Evolution of the width of the rapidity distribution on beam rapidity has been studied for a number of produced particles with UrQMD-3.3p1 generated events at various FAIR (Facility for Antiproton and Ion Research) energies. The results for the width of the rapidity distribution with beam rapidity, obtained with UrQMD generated events, are compared with the existing experimental data (E802, E877, E896, E917, NA49). For both UrQMD and experimental data, the width of the rapidity distribution is found to bear scaling behavior with beam rapidity for all the hadrons. Such scaling behavior is found to follow separate mass ordering for the studied mesons and baryons.

4.1 Introduction

Lattice QCD [17, 15] predicted that at high temperature and/or baryon density, the ordinary hadronic matter undergoes a phase transition to form a new state of matter known as Quark-Gluon Plasma (QGP). Relativistic heavy-ion collision is the only possible way to produce and study QGP in the laboratory. This transient phase of matter can only be realized by studying several signatures [159–161] that have been proposed in the past few decades.

Unlike the kind of experiments performed at RHIC and LHC, the upcoming Compressed Baryonic Matter (CBM) experiment at the future Facility for Antiproton and Ion Research (FAIR) is going to be a dedicated fixed target heavy-ion experiment (Au+Au collisions up to 35*A* GeV) planned to explore the properties of nuclear matter at moderate temperature and high baryon density [32–35]. In heavy-ion collisions at FAIR energies, the baryon density is expected to be extremely high, something of the order of 5-10 times the normal nuclear matter density[1] [162]. Under such a high baryon density environment, the dynamical properties of hadrons are expected to be modified [45]. As a result, effects which couple with baryon density are expected to be very prominent in the FAIR energy domain [163]. Using the large acceptance[2] state-of-the-art detectors of the upcoming CBM experiment, produced particles can be measured almost in the entire forward rapidity hemisphere with utmost precision. Thus, in the upcoming CBM experiment, there will be a possibility for the measurement of evolution of rapidity width with beam energy and centrality. In this work, an attempt has therefore been made, with UrQMD-3.3p1 (without taking into account the hydro part) [100, 101] generated $Au+Au$ events at 10, 20, 30, and 40*A* GeV, to investigate the evolution of the rapidity width with beam rapidity (y_b) for a few mesons and baryons and to compare the values thus obtained with the existing experimental data.

4.2 Rapidity and its significance

Rapidity: Unlike scattering angle, the *Rapidity*, a Lorentz invariant quantity, is a useful variable to study the dynamics of heavy-ion collision. Rapidity is denoted by y and is defined as,

$$y = \tanh^{-1}\beta = \frac{1}{2}\ln\frac{1+\beta}{1-\beta}, \tag{4.1}$$

where, $\beta = v/c$, is the velocity of the particle in units of the velocity of light.

The dependence of rapidity (y) as a function of β is shown in Fig. 4.1. It is seen from the figure that $y \sim \beta$ in the limit $\beta \to 0$; while for large velocities (i.e. $\beta \to 1$) the value of rapidity is very large i.e. $y \to \infty$. Thus, the dimensionless variable rapidity can be used as a measure of longitudinal velocity. In other words, for a particle that losses less energy in the collision will be emitted along the forward direction with a large velocity and therefore possess larger rapidity. On the other hand, the particle which practically stops during the collisions (and whose kinetic energy is being utilized for the production of particles) will

[1]Normal nuclear matter density i.e. $\rho_0 = 0.17/\text{fm}^3$

[2]Geometrical acceptance is from 5^0 to 25^0 which translates into the η range from 1.5 to 3.18

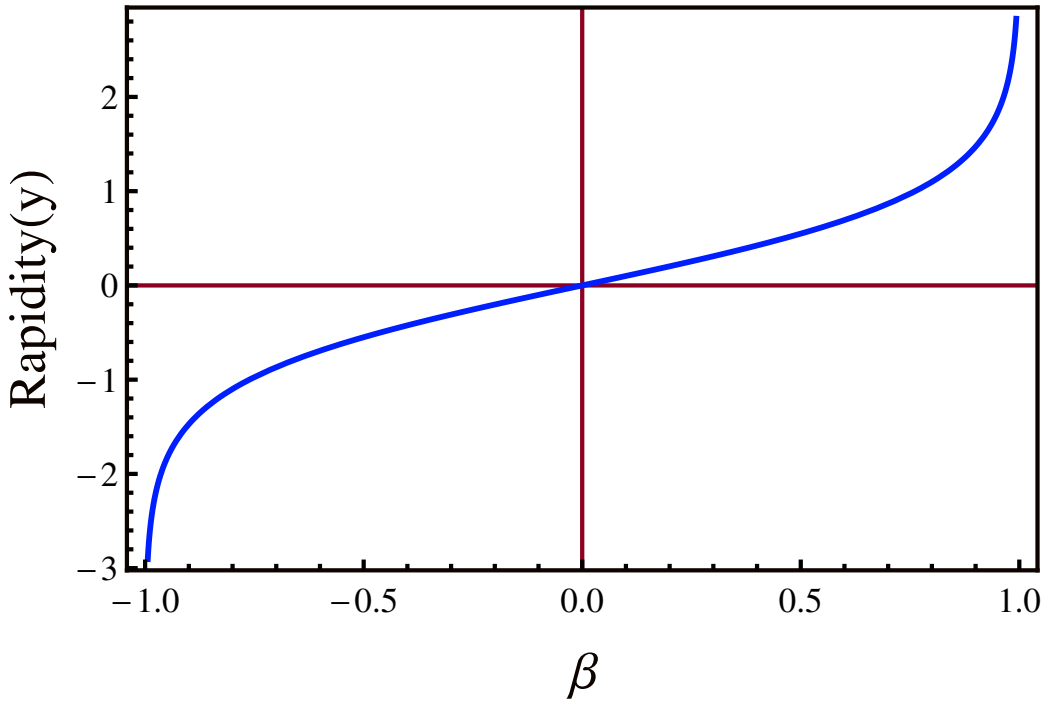

Fig. 4.1 Rapidity (y) as a function of β (see eq. 4.1).

have almost zero rapidity. Equation 4.1 can also be written as,

$$y = \frac{1}{2}\ln\left(\frac{\mathrm{E}+\mathrm{P_z}}{\mathrm{E}-\mathrm{P_z}}\right), \tag{4.2}$$

where, E and P_z represents the energy and longitudinal momentum of the particle.

Beam rapidity (y_b): Beam rapidity is another important variable which represents the maximum velocity. From equation 4.2, one can write,

$$e^{y} = \sqrt{\frac{E+P_z}{E-P_z}} \qquad \text{and} \qquad e^{-y} = \sqrt{\frac{E-P_z}{E+P_z}}. \tag{4.3}$$

Hence, the above equations translate into[3],

$$E = m_T \cosh y \qquad \text{and} \qquad P_z = m_T \sinh y, \tag{4.4}$$

where, $m_T = \sqrt{m^2 + P_T^2}$ represents the transverse mass of the particle.

[3]Using the definitions: $\sinh x = \frac{1}{2}(e^x - e^{-x})$; $\cosh x = \frac{1}{2}(e^x + e^{-x})$

For beam particles, the transverse momentum is zero ($P_T = 0$). Thus, equation 4.4 can be written as,

$$E = m_b \cosh y_b \qquad \text{and} \qquad P_z = m_b \sinh y_b, \tag{4.5}$$

where, m_b and y_b are the rest mass and the rapidity of the beam particles respectively. The parameter, y_b, is also termed as *beam rapidity*. Thus, the expression for beam rapidity can be written as,

$$y_b = \cosh^{-1}\left(\frac{E}{m_b}\right). \tag{4.6}$$

In terms of center of mass energy i.e. $\sqrt{s}$, the above equation can also be written as,

$$y_b = \cosh^{-1}\left(\frac{\sqrt{s}}{2m_n}\right). \tag{4.7}$$

Also, in terms of longitudinal momentum (P_z), the expression for beam rapidity can be written as,

$$y_b = \sinh^{-1}\left(\frac{P_z}{m_b}\right). \tag{4.8}$$

Using the above formulas, the values of beam rapidity (y_b) and mid-rapidity for $Au+Au$ collisions at 10, 20, 30 and 40A GeV in the laboratory frame are calculated and tabulated below.

Lab. energy (A GeV)	beam rapidity (y_b)	mid-rapidity
10	3.082	1.541
20	3.730	1.865
30	4.120	2.060
40	4.310	2.155

Table 4.1 The values of beam rapidity and mid-rapidity in the laboratory frame of reference or $Au+Au$ collisions at 10, 20, 30 and 40A GeV.

In heavy-ion collisions, rapidity distribution of the produced particle is sensitive to several physics phenomena. For instance, rapidity density i.e. the number of emitted particles per unit rapidity (dN/dy) is a measure of initial entropy production [164, 165] which can further be related to the energy density produced in the collision. Similarly, the differences in the rapidity distribution of protons and anti-protons can be interpreted as a consequence of

nuclear *stopping* [165, 166]. The *stopping* basically determines the energy available[4] to excite the overlapping region between the nuclei. On the other hand, the *width* of rapidity distribution is sensitive to the longitudinal collective flow [167]. Further, the rapidity width for a given freeze-out temperature in Landau hydrodynamical model is sensitive to the velocity of sound in the medium [168, 169]. In the following discussion, various aspects of rapidity distribution have been summarized in the light of different fixed target heavy ion experiments like Alternating Gradient Synchrotron or AGS (E866, E877, E802, E891, E896, E917) [170–176] at BNL (Brookhaven National Laboratory) and Super Proton Synchrotron or SPS (NA49) [177–183] at CERN.

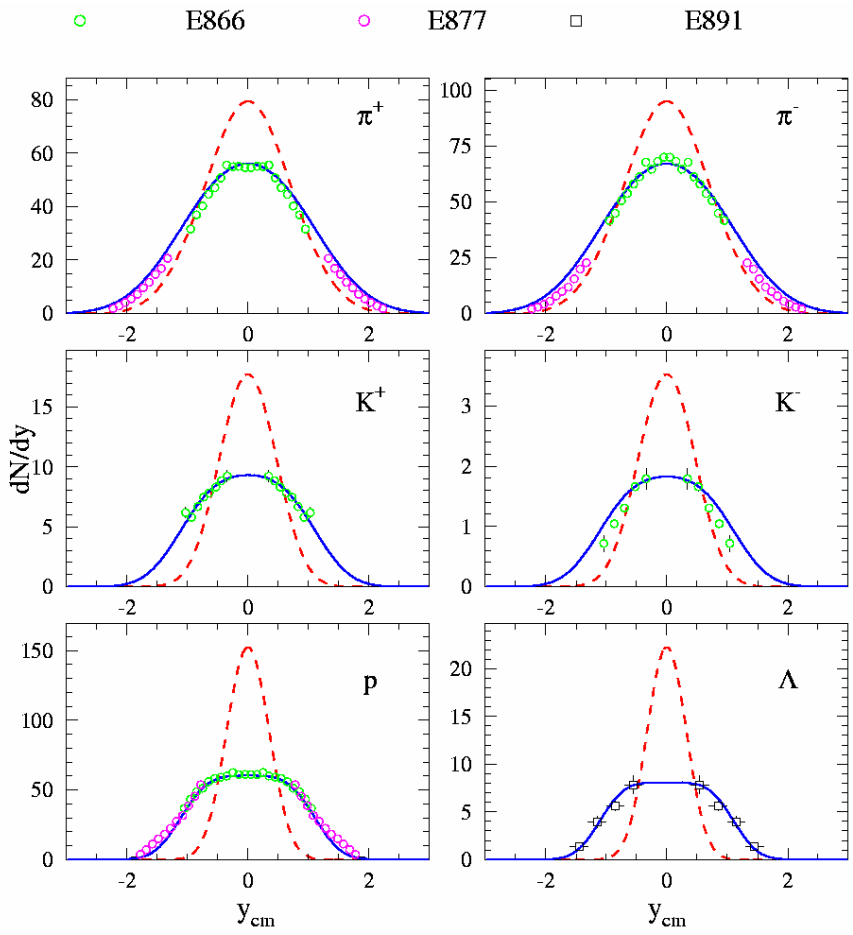

Fig. 4.2 The rapidity distribution of π, k, Λ and protons in central $Au+Au$ collisions at 10.7A GeV measured by different experiments in AGS [170–176].

The rapidity distributions of various identified particles such as $\pi^{\pm}$, $k^{\pm}$, Λ and proton have already been measured by several experiments at AGS (E866, E877, E891) [170–176]

[4] these available excitation energy is utilized for the particle production

as shown in Fig. 4.2. The rapidity distributions of different particles measured at AGS were fitted with the help of a static thermal fireball model as given by,

$$\frac{dN}{dy} = AT^3 \left[\frac{m^2}{T^2} + \frac{m}{T}\frac{2}{\cosh y} + \frac{2}{\cosh^2 y}\right] \times e^{-(\frac{m}{T})\cosh y}, \tag{4.9}$$

where, A is the normalization constant and T is the temperature of the static fireball. The red dashed line in Fig. 4.2 corresponds to a static isotropic thermal source ($T = 130$ MeV). It is clearly seen from the figure that the above model cannot explain the experimental data at all. The experimental data can only be explained by incorporating longitudinal collective velocity in the above model. The solid line as shown in Fig. 4.2 resembles a longitudinally expanding source with $T = 130$ MeV and $\beta = 0.5$. It can therefore be concluded from this study that the width of the rapidity distribution is sensitive to the longitudinal collective flow.

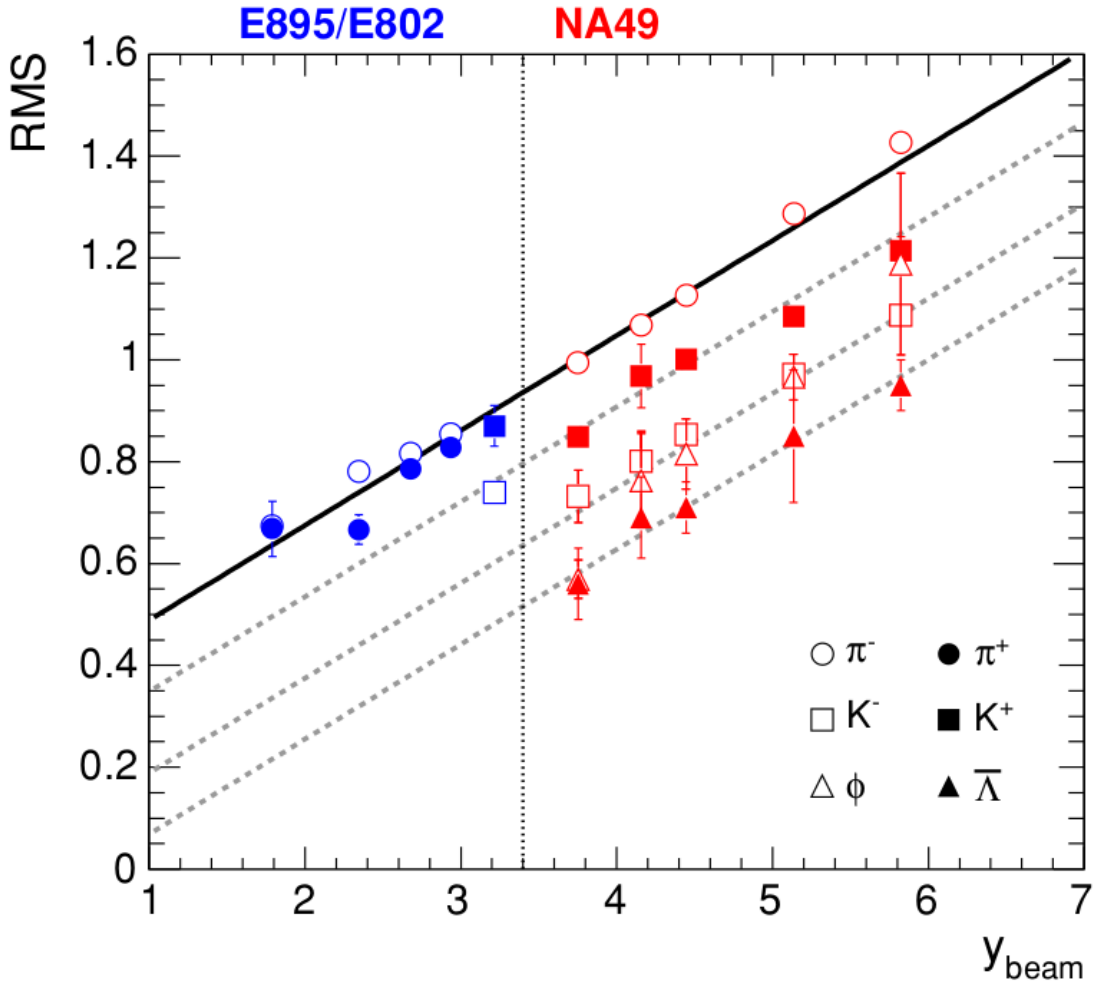

Fig. 4.3 Rapidity width (RMS) as a function of beam rapidity (y_b). The figure has been taken from the Ref. [182]

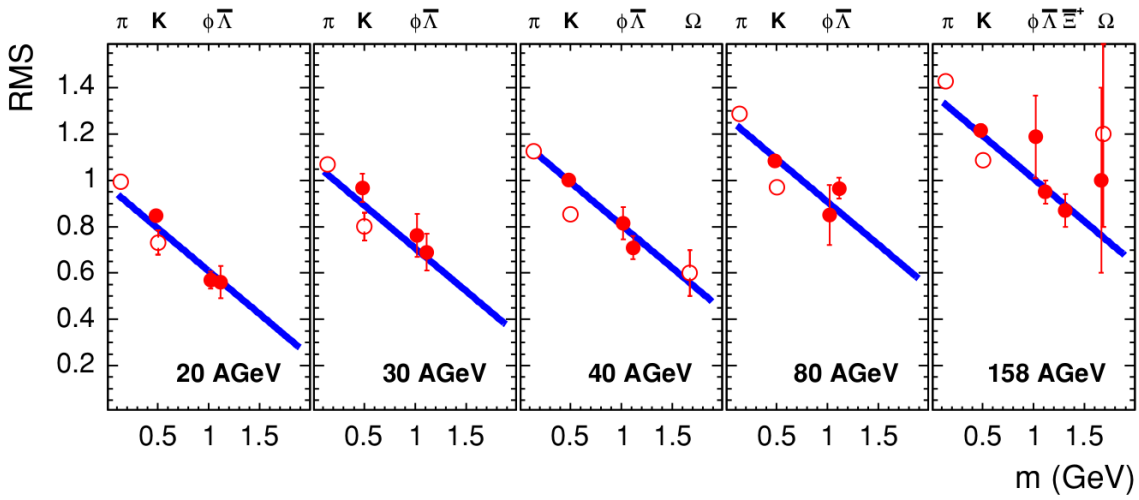

Fig. 4.4 Rapidity width (RMS) as a function of the mass of the identified particles. The figure has been taken from the Ref. [182]

On the other hand, using SPS data for the Pb+Pb system, Friese *at al.* reported a scaling behavior of the rapidity width with beam rapidity [182, 183]. The widths of the rapidity distributions were seen to follow an inverse relationship with the masses of the produced particles (See Fig. 4.3 and 4.4). The mass dependence of rapidity width has been interpreted as a result of thermal spectrum of hadrons superimposed on the longitudinal collective expansion [182]. In other words, the mass dependence comes into the picture by virtue of contribution of longitudinal collective flow velocity (which is mass dependent) to the uniform velocity acquired by all the particles due to a stationary thermal source. It is worth mentioning that although the above results are inclusive of $\bar{\Lambda}$, no result has been reported including the Λ baryon. Even though, Λ and $\overline{\Lambda}$ have same mass, which is in close proximity to the mass of ϕ meson, a distinctive feature of Λ (uds) and $\overline{\Lambda}$ ($\bar{u}\bar{d}\bar{s}$) is that while the former contains both leading and produced quarks, the latter contains produced quarks only.

4.3 Computing facility for event generation

UrQMD is a complex model where a large set of coupled (Boltzmann-type) partial integro-differential equations are solved using Monte Carlo method in order to describe the time evolution of various phase space densities of over 85 number of mesons and baryons species [184]. A detailed discussion regarding the physics assumption incorporated in UrQMD model is presented in the following section. At FAIR energy domain, the production probabilities of the multi-strange hadrons are very low. Thus, in order to gather sufficient statistics, huge number of events are required to be generated. Further, a complex code like UrQMD requires

Fig. 4.5 The HPCC (High Performance Computing Cluster) facility along with the old server and other accessories situated at the Nuclear and Radiation Physics Laboratory, Department of Physics, Gauhati University.

an enormous computational resource as well as huge run time. Although, ordinary PC can be used to generate UrQMD events, due to the time and computational resource constraint, the entire event generation for the present work is performed in the HPCC facility of the Nuclear and Radiation Physics Laboratory, at the department of Physics, Gauhati University (Fig. 4.5).

In the HPCC facility, the Rocks Cluster Distribution (also known as NPACI Rocks) version 6.1.1 is implemented with the CentOS (version 6.5) operating system. Parallel jobs can be submitted to the HPCC via the scheduler known as Sun Grid Engine[5] (SGE). A block diagram of the HPCC is illustrated in Fig. 4.6. The HPCC facility contains the following parts: (i) One Master Blade server, and (ii) two slave servers viz. Compute 1 and Compute 2. The Master blade server consisted of 24 nodes, whereas the Compute 1 and Compute 2 server contain 24 and 12 nodes respectively. For the Master server, 14 nodes out of 24 are kept reserved. Thus, total 92 number of *threads* are available for job submission and hence 92 jobs can be submitted in parallel for execution.

The event statistics of our generated data (for central collisions only) are presented in Table 4.2.

[5]SGE is a distributed resource management software and it allows the resources within the cluster (cpu time, software, licenses etc.) to be utilized effectively.

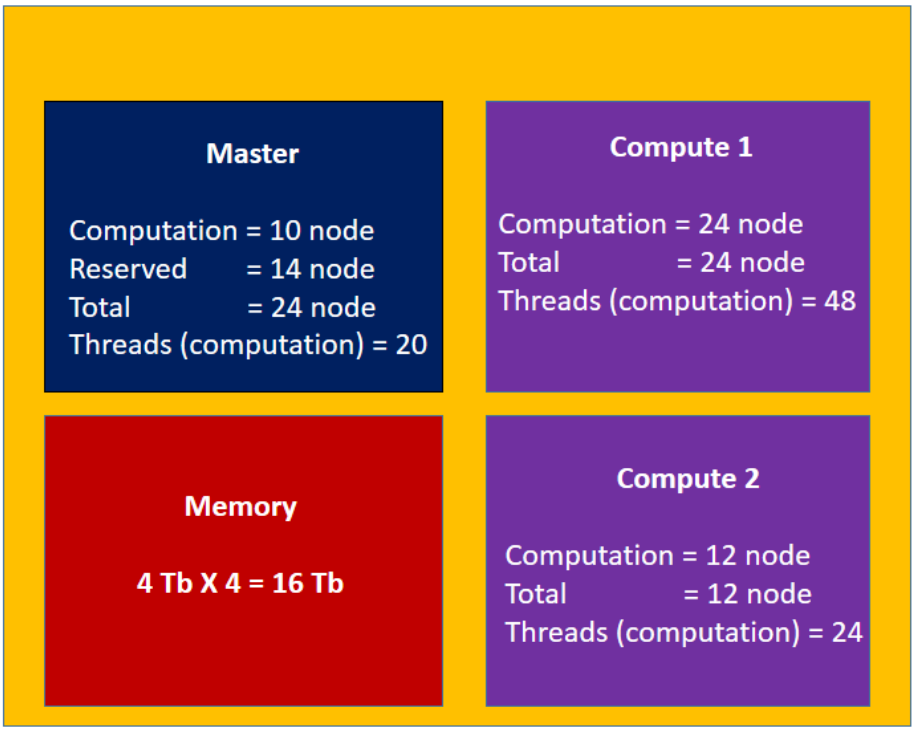

Fig. 4.6 Block diagram of the new HPCC (High Performance Computing Cluster) facility situated at the Nuclear and Radiation Physics Laboratory, Department of Physics, Gauhati University.

4.4 Results and discussion

The UrQMD model

Ultra relativistic Quantum Molecular Dynamics (UrQMD) [100, 101] is a microscopic transport model based on a phase space description of hadron-hadron, hadron-nucleus and nucleus-nucleus collisions that remains successful in describing the observables of heavy-ion collisions over an wide range of beam energies i.e. right from E_{lab} = 100 AMeV to $\sqrt{s}$ = 200 GeV [102, 185–187]. This model is based on Boltzmann equations in which the collision term includes various hadron species. At low and intermediate energies ($\sqrt{s} < 5$ GeV), it describes the phenomenology of heavy ion collisions in terms of the interactions between known hadrons and their resonances. 55 baryon species up to an invariant mass of 2.25 GeV which includes nucleons, deltas, hyperons and their resonances and 32 mesons up to 2 GeV along with their anti-particles are incorporated in the model. At higher energies ($\sqrt{s} > 5$ GeV), the excitation of color strings and their subsequent fragmentation into hadrons are taken into account. The hadron formation time in this model is taken to be of the order of 1-2 fm/c depending upon the energy of the created hadrons. The collisions between two closely

Table 4.2 Event statistics of the present investigation (for central collisions only).

Energy (A GeV)	Events (Million)	$\pi^- \times 10^8$	$K^- \times 10^7$	$\Lambda \times 10^7$	$\phi \times 10^5$	$\Xi^- \times 10^5$	$\Omega^- \times 10^4$
10	4.6	7.37	1.74	6.70	9.76	7.68	2.73
20	3.1	7.66	2.72	6.40	17.81	11.80	6.30
30	4.9	14.28	6.55	15.15	42.36	24.20	20.07
40	1.1	3.47	1.82	3.51	11.02	6.31	6.12

propagating hadrons will occur in this model, if the relative distance d between them in three dimensional configuration space satisfies the following relation,

$$d \leq \sqrt{\sigma_{tot}/\pi}, \tag{4.10}$$

where, σ_{tot} represents the total cross-section between the two hadrons which depends on the isospin, flavor and center of mass energy between the colliding particles. The elastic and total proton-proton cross-section are used in the model from the Ref. [188]. Following the isospin symmetry, neutron-neutron cross-section is taken to be same as that of proton-proton cross-section. In UrQMD, for the estimation of the Meson-Meson (MM), Meson-Baryon (MB) and Baryon-Baryon (BB) cross-sections an effective parametrization is employed in which the free parameters are tuned in accordance with the experimental measurements. The detailed prescription regarding the calculation of various cross-sections is reported in the Ref. [100]. For higher incident energies the proton-proton, MM, MB, baryon-antibaryon cross-sections are modeled based on the CERN-HERA parametrization [188],

$$\sigma(p) = \mathrm{A} + \mathrm{B}p^n + \mathrm{C}\ln^2(p) + \mathrm{D}\ln(p), \tag{4.11}$$

The various fit parameters i.e. A, n, B, C and D for different reactions are provided in the Table II of the Ref. [101]. For $p_{lab} < 5$ GeV/c, the following sets of parametrization are considered to obtain a good fit with the experimental data [101, 184].

$$\sigma_{el} = \begin{cases} 31.6 + 18.3p^{-1} - 1.1p^{-2} - 3.8p, & : \quad 0.3 < p < 5; \\ 78.6, & : \quad p < 0.3 \end{cases}$$

$$\sigma_{tot} = \begin{cases} 75.0 + 43.1p^{-1} + 2.6p^{-2} - 3.9p, & : \quad 0.3 < p < 5; \\ 271.6\exp(-1.1p^2), & : \quad p < 0.3 \end{cases}$$

Furthermore, Additive Quark Model (AQM) [189] is used to calculate the cross-sections for those interactions (e.g. hyperon baryon interaction) for which no experimental data is available.

As discussed earlier, beyond incident beam energy of 8-10A GeV, the particle production mechanism is mainly dominated by string excitation and fragmentation. At high energies, the interaction between two hadrons may lead to the creation of new objects - *color tubes* or *strings*. As time elapses and the energy deposition in the string increases, at some point of time, it will be energetically favorable to break the string by creating quark-antiquark ($q\bar{q}$) pair from the vacuum and thereby producing hadrons. This process is known as string fragmentation. Fig. 4.7 illustrates the fragmentation of a baryon-string, where two quark-antiquark pair namely, $s\bar{s}$ and $u\bar{u}$ are popped-up from the Dirac-sea. Here, the newly produced $\bar{s}$ quark combines with the newly produced u quark to form a kaon, the leading diquark together with a s quark forms a hyperon, while a newly produced $\bar{u}$ quark combines with the leading quark to produce a pion. Further, diquark-antidiquark instead of $q\bar{q}$ production from the Dirac-sea is necessary for the production of baryon-antibaryon pair in the string fragmentation scheme [100]. As expected, the production of heavier quarks are suppressed in UrQMD model. The suppression of different flavors of quark-antiquark pairs are estimated using the standard Schwinger formula [190],

$$|\mathscr{M}|^2 \sim \exp\left(-\frac{\pi m^2}{\kappa}\right), \tag{4.12}$$

where, $\mathscr{M}$ represents the matrix element for the production of $q\bar{q}$ pairs. κ is the string tension, whose value in UrQMD by default is considered to be 1 GeV/fm. Suppression factor for different flavors of quark-antiquark pairs in UrQMD model are taken to be,

$$u : d : s : qq = 1 : 1 : 0.35 : 0.1 \tag{4.13}$$

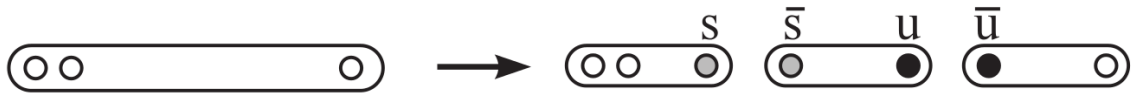

Fig. 4.7 Illustration of string fragmentation [100].

4.4.1 Rapidity distribution: UrQMD prediction and its comparison with the existing experimental data

As mentioned in section 4.2, in a heavy-ion collision, the rapidity (y) or pseudorapidity (η) distribution is found to be quite informative of the particle production mechanism [169, 191]. In Fig. 4.8, the rapidity distributions of a few hadrons such as π^-, k^-, ϕ, and Λ produced in UrQMD generated $Au+Au$ collisions at 10, 20, 30 and 40A GeV are plotted and compared with the existing SPS [177–183] and AGS (E802, E877, E896, E917) [170–176] data at the same energies. It is seen from this figure that, with UrQMD generated events, the rapidity distribution of (Λ + Σ^0) and not Λ alone gives a better agreement with the experimental data on Λ. This is because of the fact that Λ, resulting from the decay of Σ^0, cannot be separated from the directly produced ones via a secondary vertex measurement [192] and hence the experimentally measured value of Λ is an overestimation of the number of Λ actually produced in the collision.

From Fig. 4.8, it is also seen that lighter mesons like π^- and k^- show a fair agreement between experimental data [170–183] and UrQMD prediction at all energies. However, for heavier meson like ϕ, as the energy of collision increases, there is a considerable disagreement between the observed and UrQMD predicted values. This has been attributed to the fact that [179], at low energies, $E_{LAB} \leq 10A$ GeV, the ϕ production mechanism is predominantly via hadronic channels; at higher energies there might be significant contribution from nonhadronic processes as well. In UrQMD, with regard to the production of ϕ meson, the hadronic processes mostly refer to KK coalescence[6] whereas other nonhadronic contributions mostly come from string excitation and fragmentation.

4.4.2 Width of the rapidity distribution

The rapidity spectra of all the studied hadrons from UrQMD generated and experimental data [170–176] (AGS data) are parametrized by a sum of two Gaussian functions displaced symmetrically around midrapidity by a shift a,

$$\frac{dn}{dy} \propto \left[e^{-\frac{(y-a)^2}{2\sigma^2}} + e^{-\frac{(y+a)^2}{2\sigma^2}} \right]. \tag{4.14}$$

The rapidity distributions corresponding to 10, 20, 30 and 40A GeV are fitted with the double Gaussian function (see eqn. 4.14) and are shown in Figs. 4.9, 4.10, 4.11, 4.12.

The width of the distribution is characterized by root mean square RMS $= \sqrt{\sigma^2 + a^2}$ and the resulting values of RMS are listed in Table 4.3. Where σ is the standard deviation of the

[6] two-third of the ϕ meson is produced in UrQMD via kaon coalescence [193]

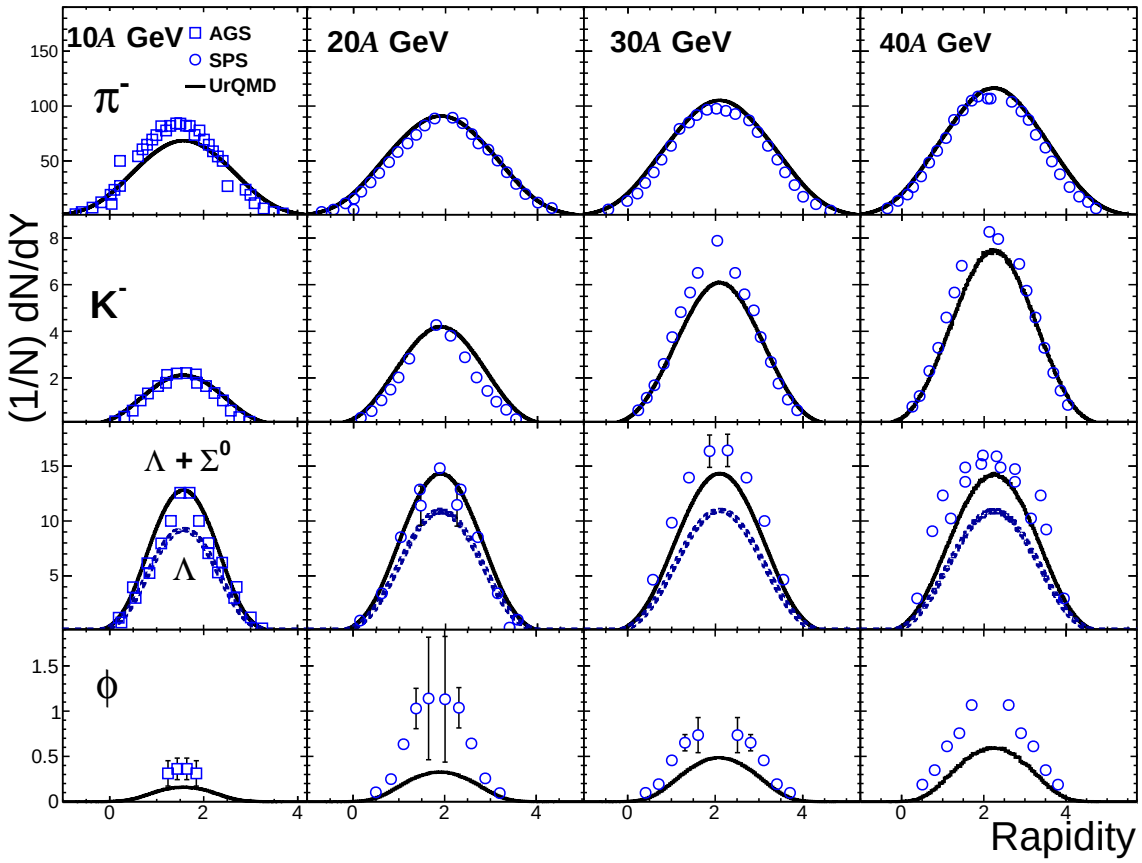

Fig. 4.8 Rapidity distribution of produced particles $(\pi^-, k^-, \Lambda, \phi)$ for four different beam energies E_{LAB}= 10, 20, 30 and 40A GeV is compared with the existing SPS (NA49) [177–183] (7.2% central) and AGS (E877, E802, E896, E917) [170–176] data (5% central). It is to be noted that the NA49 data (20-40A GeV) are for the $Pb+Pb$ system and the AGS data (10A GeV) are for the $Au+Au$ system, while the UrQMD calculation is done for the $Au+Au$ system with impact parameter 0-3 fm (5%) and 0-3.5 fm (7.2%).

distribution. The error of standard deviation can be calculated using the formula,

$$\sigma_{error} = \sqrt{\frac{\sigma}{2N}}, \tag{4.15}$$

Hence, the error in RMS of the rapidity distribution can be calculated using the following formula,

$$(RMS)_{error} = \frac{1}{RMS}\sqrt{\sigma^2\sigma^2_{error} + a^2 a^2_{error}}. \tag{4.16}$$

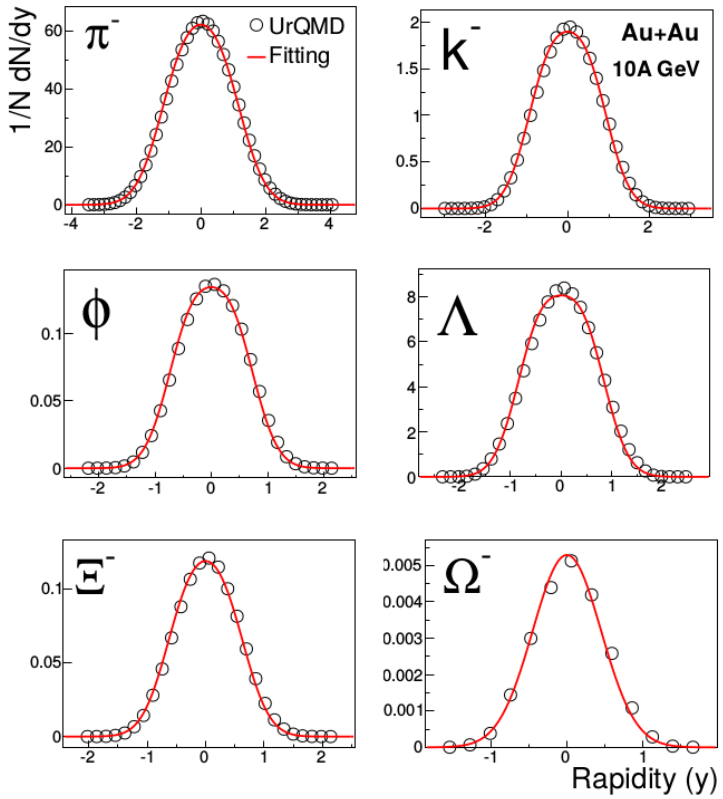

Fig. 4.9 The double Gaussian fitting as per eqn. (4.14) to the rapidity spectra of various produced particles at $Au+Au$ collision at 10A GeV.

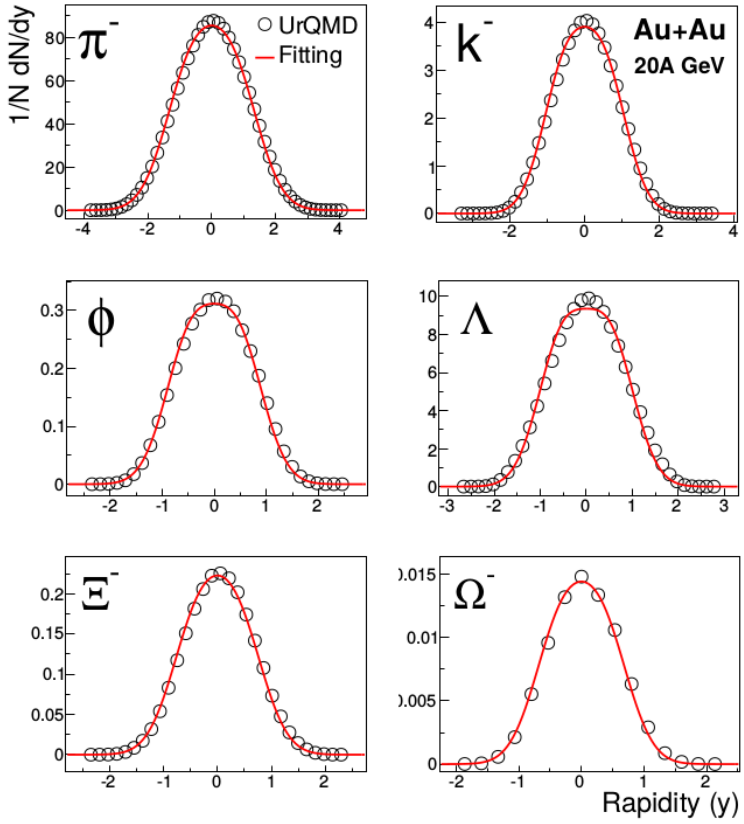

Fig. 4.10 The double Gaussian fitting as per eqn. (4.14) to the rapidity spectra of various produced particles at $Au+Au$ collision at 20A GeV.

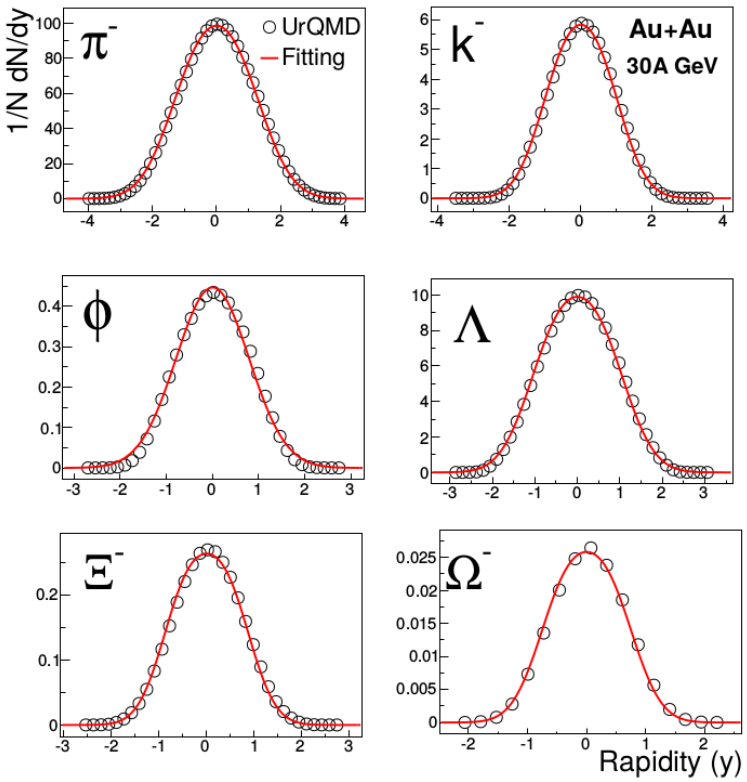

Fig. 4.11 The double Gaussian fitting as per eqn. (4.14) to the rapidity spectra of various produced particles at $Au+Au$ collision at 30A GeV.

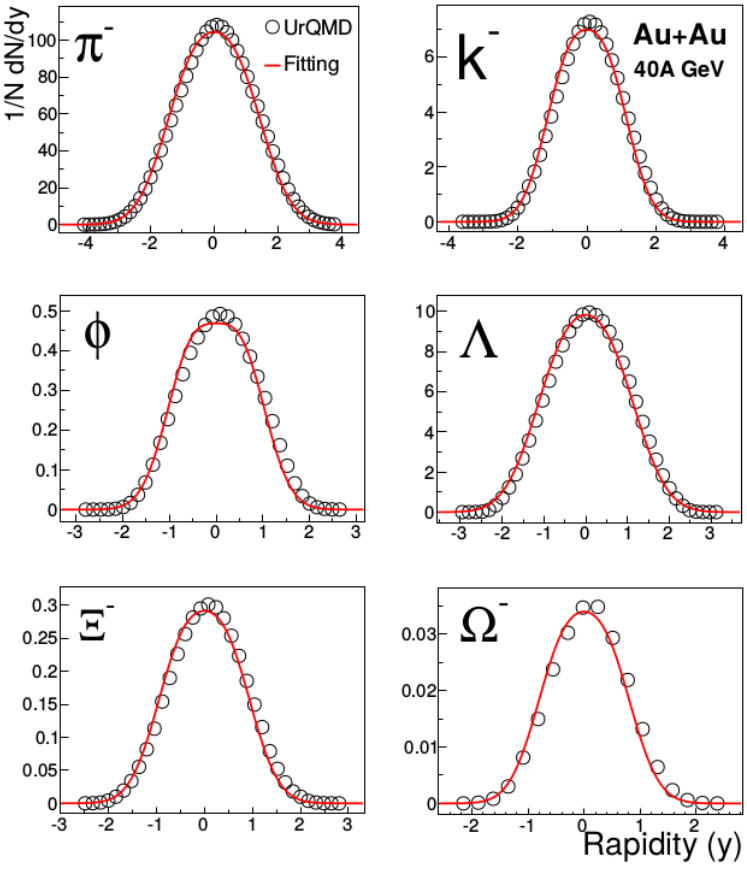

Fig. 4.12 The double Gaussian fitting as per eqn. (4.14) to the rapidity spectra of various produced particles at $Au+Au$ collision at 40A GeV.

Table 4.3 The parameter RMS resulting from the double Gaussian fits of the rapidity spectra of all the studied hadrons of UrQMD generated and experimental data (within parentheses). The RMS values of NA49 data are taken from refs. [194, 179, 180].

RMS	10*A* GeV	20*A* GeV	30*A* GeV	40*A* GeV
π^-	0.959 ± 0.00004 (0.844± 0.08)	1.050 ± 0.00005 (0.991 ± 0.01) [194]	1.111 ± 0.00003 (1.068 ± 0.01) [194]	1.149 ± 0.00007 (1.123 ± 0.01) [194]
K^-	0.716 ± 0.0002 (0.628 ± 0.02)	0.803 ± 0.0001 (0.727 ± 0.034) [194]	0.854 ± 0.0001 (0.798 ± 0.009) [194]	0.887 ± 0.0002 (0.852 ± 0.069) [194]
ϕ	0.560 ± 0.0006 (0.511 ± 0.301)	0.664 ± 0.0005 (0.582 ± 0.031) [179]	0.724 ± 0.0003 (0.769± 0.030) [179]	0.761 ± 0.0006 (0.852±0.015) [179]
Λ	0.630 ± 0.00007 (0.648 ± 0.05)	0.741 ± 0.0003 (0.70 ± 0.01) [180]	0.814 ± 0.0006 (0.89±0.02) [180]	0.864 ± 0.0006 (1.11±0.08) [180]
Ξ^-	0.519 ± 0.0008	0.605 ± 0.0008 (0.64 ± 0.08) [180]	0.661 ± 0.0002 (0.73 ± 0.14) [180]	0.705 ± 0.0063 (0.94 ± 0.13) [180]
Ω^-	0.450 ± 0.0015	0.536 ± 0.0017	0.590 ± 0.0034	0.619 ± 0.004 (0.596 ± 0.09) [194]

4.4.3 Violation of universal mass scaling of the rapidity width: Separate mass scaling for mesons and baryons

Figure 4.13 represents the width of the rapidity distributions as a function of beam rapidity for studied mesons and baryons for UrQMD generated central $Au+Au$ collision. As expected from the kinematical point of view, the lighter particles are found to have larger rapidity width. From this plot, a scaling behavior of the width of the rapidity distribution with beam rapidity is readily evident. Friese *et al.* [182, 183] have reported similar results for Pb+Pb collision with NA49 data. It is interesting to note from Figs. 4.13(a) and 4.13(b) that although mesons and baryons separately follow mass ordering, such mass ordering is violated if the studied hadrons are taken together [Fig. 4.13(c)]. Figure 4.14 contains the same plots as Fig. 4.13, but with the experimental data (of refs. [170–183]) of Fig. 4.8 of this article. It can be readily seen from Fig. 4.14 that for the experimental data also the mass ordering exists only when mesons and baryons are taken separately. Mass ordering gets disturbed if these hadrons are taken together. To see the possible effect of underestimation of the yield of UrQMD generated ϕ mesons on the mass ordering of the width of the rapidity distribution, the widths of the rapidity distributions of the ϕ meson, from both UrQMD and experimental data, are plotted in Fig. 4.15 and compared with the result obtained for Λ with UrQMD generated data. Clearly, the rapidity width of Λ is larger than the rapidity width of UrQMD and experimental ϕ. Such an observation implies that, even though the experimental values of the rapidity distribution of ϕ differ from UrQMD prediction, such differences do not have

any significant effect on our result for the mass ordering violation of the width of the rapidity distribution with beam rapidity for the studied hadrons.

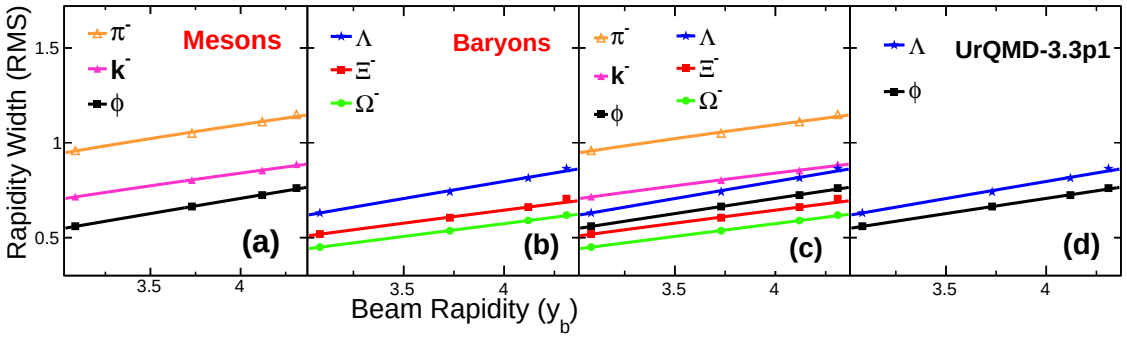

Fig. 4.13 Variation of width of the rapidity distribution with UrQMD generated data of (a) mesons, (b) baryons, and (c) all studied hadrons as a function of beam rapidity in the laboratory system. In the panel (d) the same has been plotted separately for Λ and ϕ. The solid lines correspond to linear fits. The errors are small and are within the symbol size.

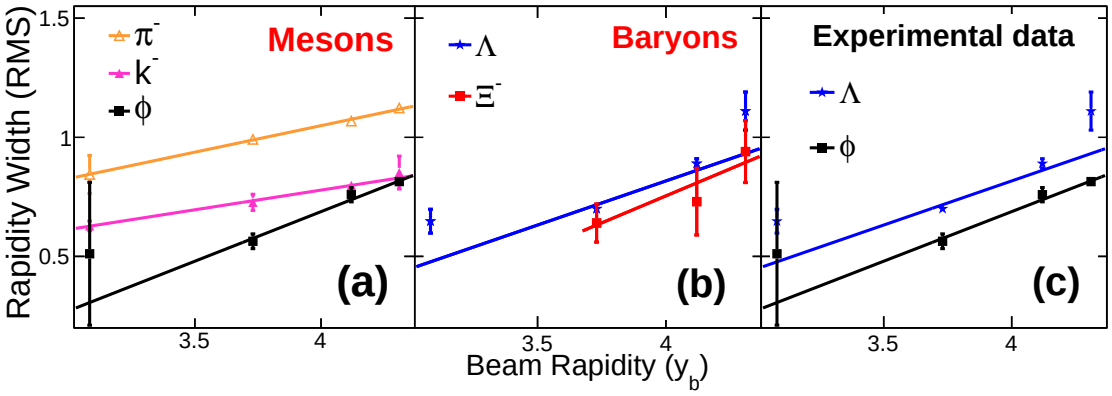

Fig. 4.14 Variation of width of the rapidity distribution (calculated from data [170–183]) of (a) mesons and (b) baryons as a function of beam rapidity in the laboratory system. (c) The same has been plotted separately for Λ and ϕ. The solid lines correspond to linear fits. The error bars shown here correspond to the statistical error. The large error at 10A GeV in ϕ data is due to large experimental error.

In order to have a clearer picture of the mass ordering violation, in Fig. 4.16, the width of the rapidity distribution at a particular energy is plotted as a function of the mass of the produced particles. It is readily seen from this figure that at each energy, for UrQMD generated data, the width of the rapidity distribution follows a separate mass ordering for the studied mesons and baryons. A similar behavior could be seen with the experimental data as well. To show that the observed violation of mass ordering is independent of the choice of a particular type of fitting of rapidity spectra, in Fig. 4.16(c) the widths of the

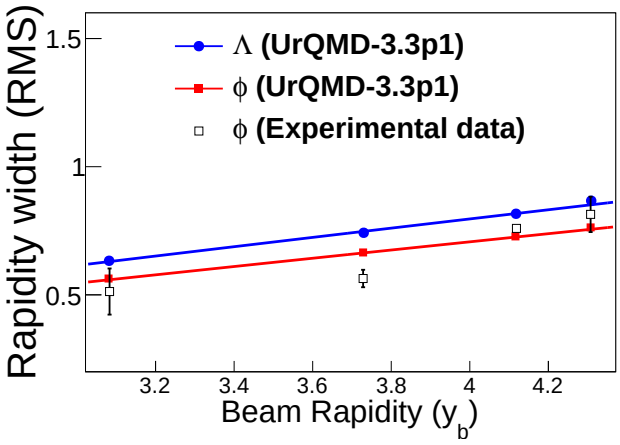

Fig. 4.15 The width of the rapidity distribution as a function of beam rapidity for ϕ from UrQMD, experimental data (AGS+SPS), and Λ(UrQMD).

rapidity distributions for single and double Gaussian fits are plotted as a function of mass of the produced particle. It is readily evident from this figure that the type of fitting of rapidity spectra has little effect on our observation of separate mass scaling for the studied mesons and baryons.

4.4.4 Role of net-baryon density on rapidity width: possible explanation for the observed separate mass scaling of rapidity width

The observed violation of mass ordering may be attributed to the fact that, at FAIR and SPS energies, due to “semitransparency", the net baryon density at midrapidity is expected to be intermediate between the SIS18/AGS and RHIC/LHC situations. That is, the net-baryon density is neither Gaussian peaked at mid-rapidity nor vanishingly small. The rapidity distribution of a particle, the production of which is sensitive to net baryon density, will tend to follow the distribution of net-baryon density i.e., it would be broader than that of a particle (mesons having no leading quark/antibaryons) the production of which does not depend on net-baryon density. The effect would be greater for the baryons that contains more light quarks. Earlier, Bleicher [195] and then Steinheimer and Bleicher [196] reported the dependence of the excitation function of the width of the rapidity distribution on the initial up- and down-quark content of hadrons. This coupling to net-baryon density comes on top of the kinematic behavior which makes the rapidity distribution narrower for heavy particles. In the case of Ξ^- and ϕ, the two effects seem to more or less compensate each other. To show the dependence of rapidity distribution of the particles containing light quarks on net-baryon density, in Fig. 4.17, the rapidity distribution of net-baryon number is compared with rapidity

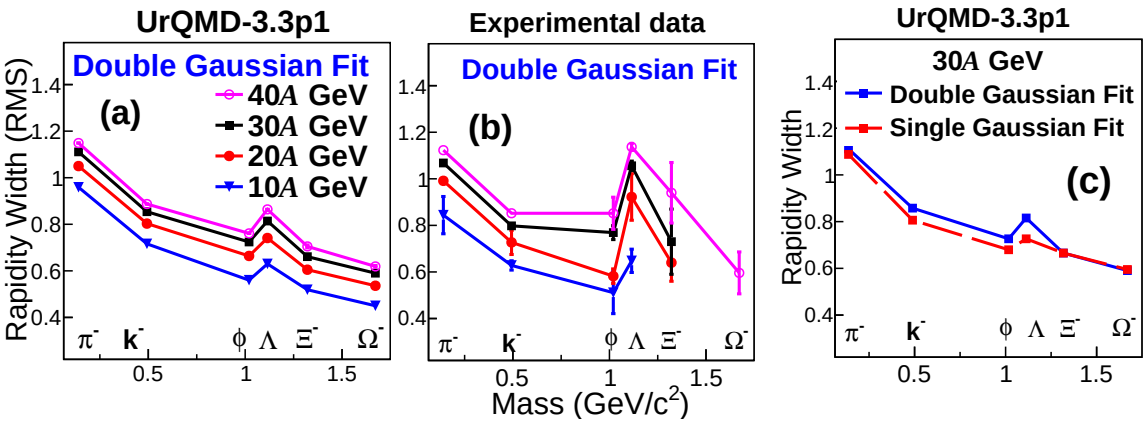

Fig. 4.16 Variation of rapidity width as a function of mass of the produced particles in central $Au+Au$ collision at FAIR energies for UrQMD and experimental data. The left and middle panels correspond to double Gaussian parametrization while the right panel corresponds to a comparison of single and double Gaussian fits for 30A GeV. The errors seen in the figure correspond to the statistical error.

distributions of Λ and $\bar{\Lambda}$. A clear dependence of the Λ rapidity distribution on net-baryon density is visible in Fig. 4.17.

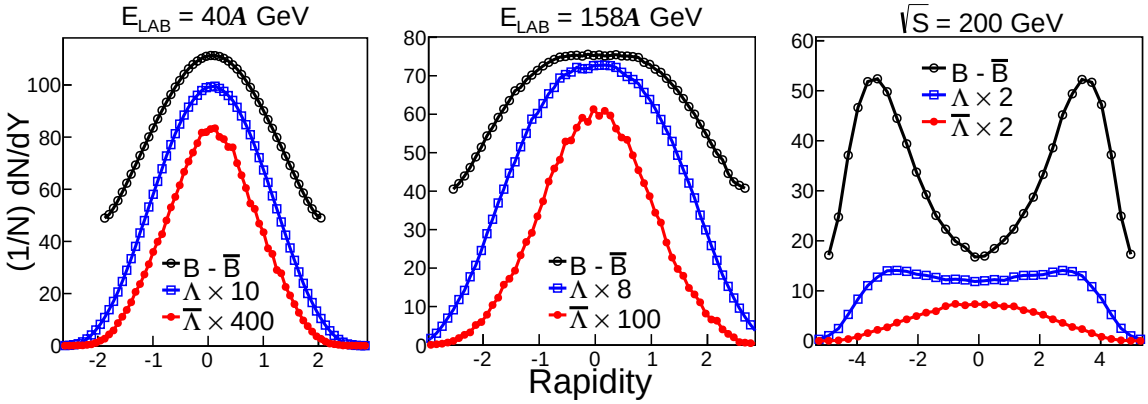

Fig. 4.17 Comparison of rapidity distribution of net-baryon number with that of Λ and $\bar{\Lambda}$ for $Au+Au$ at E_{LAB} = 40, 158A GeV and $\sqrt{s}$ = 200 GeV using UrQMD-3.3p1.

4.4.5 Role of resonance re-scattering on rapidity width

In order to ascertain the influence of resonance re-scattering on the width of the rapidity distribution, we regenerated our events at 30A GeV by switching off meson-meson (MM) and meson-baryon (MB) rescattering; that is, string excitation and fragmentation and baryon-baryon (BB) rescattering are the main mechanism of particle production. It is to be noted that,

in UrQMD, switching off MM and MB rescattering does not turn off all the MM and MB rescattering; it only turns off the processes that occur through an intermediate resonance state like $MM \rightarrow M^* \rightarrow MM$ or $MB \rightarrow B^* \rightarrow MB$. Even though these are the dominant channels of particle production, elastic and inelastic MM and MB processes are still allowed. This picture of collision implies that the early reactions that are dominated by string excitation and fragmentation still happens in a similar fashion as in the full calculation, but taking away resonance rescattering does indeed shorten the overall reaction time thus decreasing the overall thermalization of the system. Looking at Fig. 4.18 it can be seen that the resonance rescattering seems to have little influence on the width of the rapidity distribution.

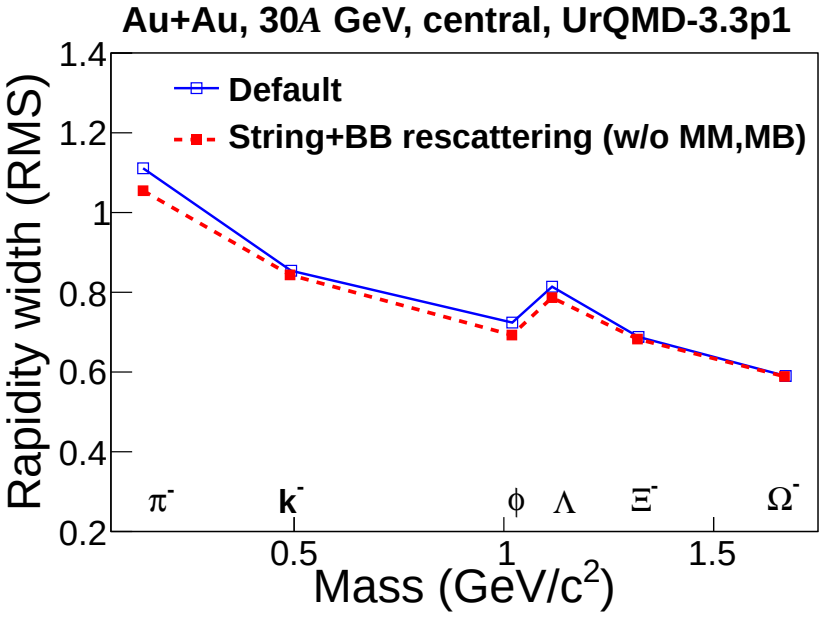

Fig. 4.18 Variation of rapidity width as a function of mass of the produced particles for two different scenarios: (a) default (string + BB,MM,MB rescattering), (b) string + BB scattering (without MM,MB rescattering) using UrQMD-3.3p1 at 30*A* GeV.

4.5 Summary

The present study of the width of the rapidity distribution of mesons and baryons produced in central $Au+Au$ collisions at 10, 20, 30, and 40 A GeV using both UrQMD generated and experimental data reveals scaling behavior of the width of the rapidity distribution with beam rapidity. Moreover, the variation of the width of the rapidity distribution with beam rapidity follows a mass ordering separately for mesons and baryons. If the studied hadrons are taken together, the mass ordering is violated. This separate mass ordering is attributed to

the fact that, unlike mesons, the width of the baryons' rapidity distribution is being influenced by kinematic consideration as well as the net-baryon density. In addition, it may be worth mentioning that the rapidity distribution of mesons containing leading quarks, e.g., K^+ ($u\bar{s}$), can also be effected by the net-baryon density. This is demonstrated in Fig. 4.19, where in spite of having the same mass, K^+ and K^- show different rapidity widths.

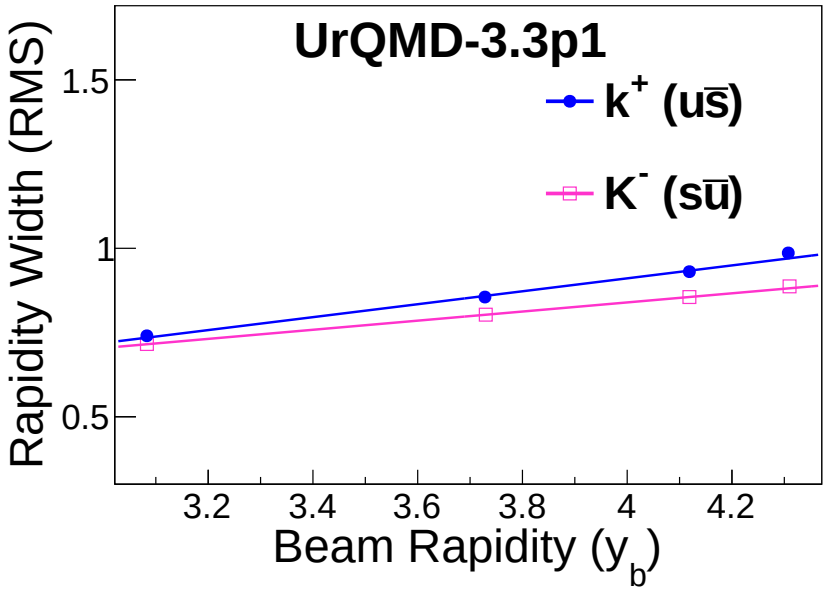

Fig. 4.19 Rapidity widths of K^+ and K^- as a function of beam rapidity for UrQMD-3.3p1 generated central Au+Au collision.

However, considering that the mass ordering of the width of the rapidity distribution could be due to the buildup of some collective flow, the possibility of different strengths of collective flow for mesons and baryons resulting in different mass ordering also cannot be ruled out completely, and needs further investigation.

5

Rapidity dependent strangeness enhancement at FAIR energies

Rapidity dependent strangeness enhancement factor for the identified particles have been studied with the help of a string based hadronic transport model UrQMD-3.3 (Ultra Relativistic Quantum Molecular Dynamics) at FAIR energies. A strong rapidity dependent strangeness enhancement could be observed with the generated data for $Au+Au$ collisions at the beam energy of 30A GeV. The strangeness enhancement is found to be maximum at mid-rapidity for the particles containing leading quarks while for particles consisting of produced quarks only, the situation is seen to be otherwise. Such rapidity dependent strangeness enhancement could be traced back to the dependence of rapidity width on centrality or otherwise on the distribution of net-baryon density.

5.1 Introduction

In heavy-ion collisions, the pattern of variation of net-baryon density (μ_B) in rapidity space is found to vary with beam energy. For example, at SIS18/AGS energies, the variation of net-baryon density with rapidity is found to be of Gaussian shape with its peak at mid-rapidity [197], whereas at top SPS and RHIC energies, such variation of μ_B shows bimodality with a

minimum at mid-rapidity [198–202, 43, 203]. At LHC energies, the net-baryon density is found to be close to zero at mid-rapidity [204]. It is therefore easily comprehensible that the rapidity distribution of a particle, the production of which is sensitive to net-baryon density, or otherwise, the particles containing leading quarks (such as k^+, Λ, Ξ^-), might tend to follow the net-baryon density. The rapidity dependence of other particles, whose none of the constituents are u or d quarks, might not exhibit any such dependencies on net-baryon density. The previous work as presented in Chapter 4 as well as in the ref. [205] on the variation of rapidity width of various produced particles on beam rapidity, with special reference to Λ and $\overline{\Lambda}$ has vindicated such prediction. It may therefore be not completely out of context to believe that a number of other kinematic and dynamical properties of heavy-ion collision might get coupled with this net-baryon density effect.

Strange particles are produced only at the time of collisions and thus expected to carry important information of collision dynamics. Strangeness enhancement is considered to be one of the traditional signatures [54, 55] of formation of Quark-Gluon Plasma (QGP). Due to the limitation of the detector acceptance, the past and ongoing heavy-ion experiments could measure the strangeness enhancement at mid-rapidity only. All such measurements assume a global conservation of strangeness. However, Steinheimer *et al.* [206] from UrQMD calculations predicted that strangeness is not uniformly distributed over rapidity space leading to a local violation of strangeness conservation. Thus, the study of rapidity dependent strangeness enhancement is of considerable significance.

Considering the fact that with the large acceptance detectors of the upcoming FAIR-CBM experiment [32–35], measurement of the rapidity dependent strangeness enhancement factor could be a possibility, strangeness enhancement factor at different rapidity bin has been estimated for various identified particles produced in $Au+Au$ collisions at 30A GeV using a string based hadronic transport model UrQMD-3.3 (Ultra Relativistic Quantum Molecular Dynamics). A total of 93 million minimum biased UrQMD events, generated using the HPCC facility of both Gauhati University and GSI, Germany are used for the present analysis.

Particle production in hadron-hadron collisions in string models like UrQMD results from the decay of color flux tubes or strings [100, 101]. The string models are very successful in describing various dynamical features of high energy heavy-ion collisions. One of the main ingredients of string models are the string fragmentation function. The fragmentation function in string models generally determines the kinematics of the produced particles. The fragmentation function $\mathrm{f(x)}$ represents the probability distribution for hadrons to acquire the longitudinal momentum fraction x from the fragmenting string. Over the years different types of fragmentation functions were proposed e.g. Lund-fragmentation [207], Field-Feynman fragmentation functions [208] etc. In the default setting of UrQMD, Field-Feynman [208]

fragmentation scheme is used for the produced particles (Eqn. 5.1), whereas, for the leading nucleons Gaussian fragmentation scheme is implemented (Eqn. 5.2). The values of the free parameters of the fragmentation function have been optimized in accordance with the experimental data. For the sake of completeness, the fragmentation functions are plotted as a function of longitudinal momentum fraction x as shown in Fig. 5.1,

$$f(x)_{prod} = (1-x)^2, \tag{5.1}$$

$$f(x)_{lead} = \exp\left(-\frac{(x-B)^2}{2A^2}\right). \tag{5.2}$$

where, $f(x)_{lead}$ and $f(x)_{prod}$ are the fragmentation function of leading nucleons and produced particles respectively.

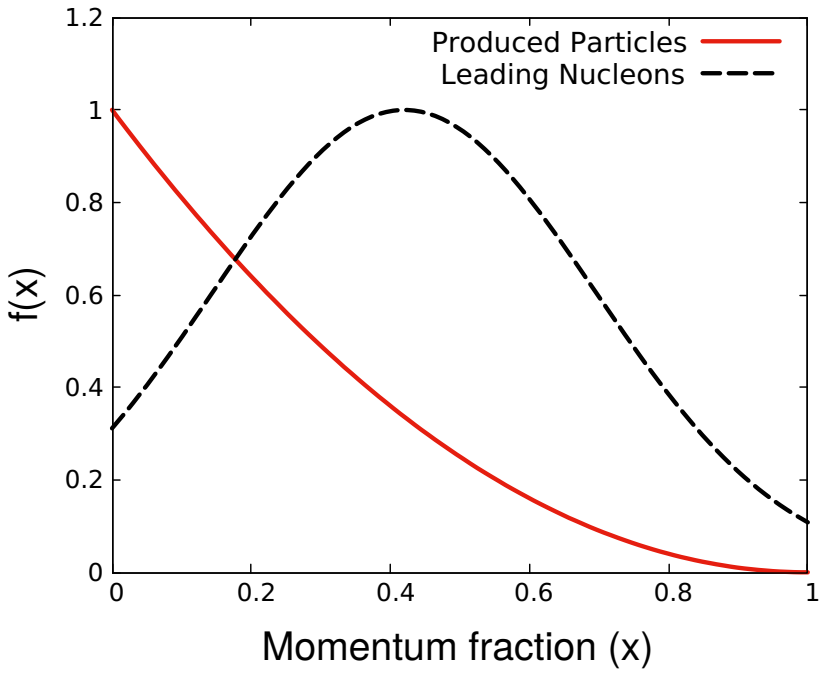

Fig. 5.1 The default string fragmentation scheme used in UrQMD [100, 101].

Strange particle production in UrQMD: As far as the production of strange hadrons are concerned, in heavy-ion collision, they may either be produced at the very early stage in the initial collisions among the incoming nucleons or in the later stage through secondary collisions among the produced particles [209]. In low energy domain i.e., close to threshold energy, strange particles can either be produced in NN reaction channel directly (also known as *associated strangeness production*) e.g., $p+p \rightarrow p+\Lambda+K^+$ or in two steps reactions such as $p+p \rightarrow N+N^*_{1710}$ and finally $N^*_{1710} \rightarrow Y+K^+$. As already discussed in section

4.4.1 of Chapter 4, at higher incident beam energies, strange particle production in general is dominated by string excitation and fragmentation [100, 101]. Other than string excitation and fragmentation, the multi-strange hyperons like Ω(sss) can also be produced via strangeness exchange reaction channel i.e. $\Xi K \rightarrow \Omega\pi$.

5.2 Strangeness enhancement

Strangeness enhancement factor E_S is quantified by measuring the ratio of yield of strange particles in $A+A$ collision and respective yield in $p+p$ collisions, where both the numerator and denominator are normalized by the average number of participating nucleons i.e. $\langle N_{part} \rangle$ calculated using Glauber model [210]. The conventional definition of strangeness enhancement factor is [57, 211],

$$E_s = \frac{(Yield)_{AA}}{\langle N_{part} \rangle} / \frac{(Yield)_{pp}}{2}. \tag{5.3}$$

In this report, using reference [212], an alternative definition of strangeness enhancement factor E_S is used where E_S is defined as,

$$E_S = \left[\frac{(Yield)_{AA}}{\langle N_{\pi^-} \rangle} \right]_{central} / \left[\frac{(Yield)_{AA}}{\langle N_{\pi^-} \rangle} \right]_{peripheral}, \tag{5.4}$$

where, the average number of produced pions i.e. $\langle N_{\pi^-} \rangle$, instead of $\langle N_{part} \rangle$, is chosen as a measure of centrality variable as the later exhibits a nonlinear behavior with the volume of the participant zone [161, 213].

5.3 Results and discussion

The strangeness enhancement factor (E_S) has been estimated using Eqn. 5.4 and plotted as a function of rapidity for various identified strange particles for $Au+Au$ collisions at 30A GeV and is shown in Fig. 5.2. The impact parameter window chosen for central and peripheral collisions are 0-3 fm and 9-13 fm respectively. $Au+Au$ collisions at 30A GeV are used for the present study as baryon density is reported to be maximum at this energy [214]. It is interesting to see from the figure that E_S depends strongly on rapidity and this dependence follow two distinctive patterns. While the enhancement factor at mid-rapidity is found to be maximum for the particles containing leading quarks (filled circle), the same is observed to be minimum at mid-rapidity for the particles containing produced quarks only (open circle). However, even though a rise and fall pattern is also visible for Ω^-, consisting

of three produced quarks only (sss), the existence of a slight dip at mid-rapidity can be clearly visible and is consistent with the general trend.

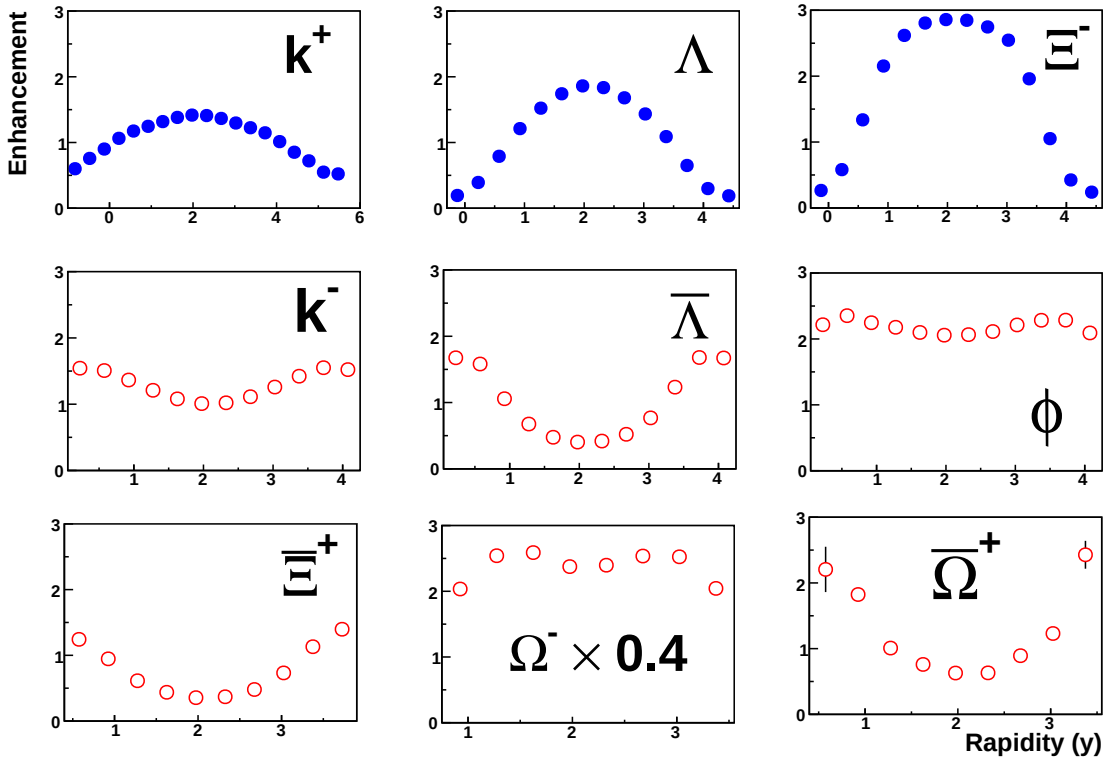

Fig. 5.2 Strangeness enhancement factor as a function of rapidity for particles containing at least one leading quark (filled circle) and particles containing only produced quarks (open circle) for $Au+Au$ collisions at 30A GeV with UrQMD model. The errors are small and are within the symbol size.

To understand the underlying dynamics of such rapidity dependent strangeness enhancement, the normalized rapidity distributions for central and peripheral collisions (Fig. 5.3) and the width of the rapidity distribution as a function of centrality (Fig. 5.4) are plotted for various produced particles. It is readily evident from Fig. 5.3 and Fig. 5.4 that the different patterns of rapidity dependence of strangeness enhancement factor for particles containing and not containing leading quarks lie on the dependence of rapidity distribution or otherwise the variation of the width of the rapidity distribution on centrality. The width of the rapidity distribution is more for central collisions than the peripheral collisions for the particles containing leading quarks, a feature that might be attributed to the variation of net-baryon density with impact parameter at the studied energy. In Fig. 5.5, $\bar{\Lambda}$ to Λ ratio is therefore plotted against rapidity for different centrality for the studied $Au+Au$ collisions at 30A GeV. It could be readily seen from this figure that as one go from central to peripheral collision, the width of the rapidity dependent $\bar{\Lambda}/\Lambda$ plot decreases. Thus, with increasing

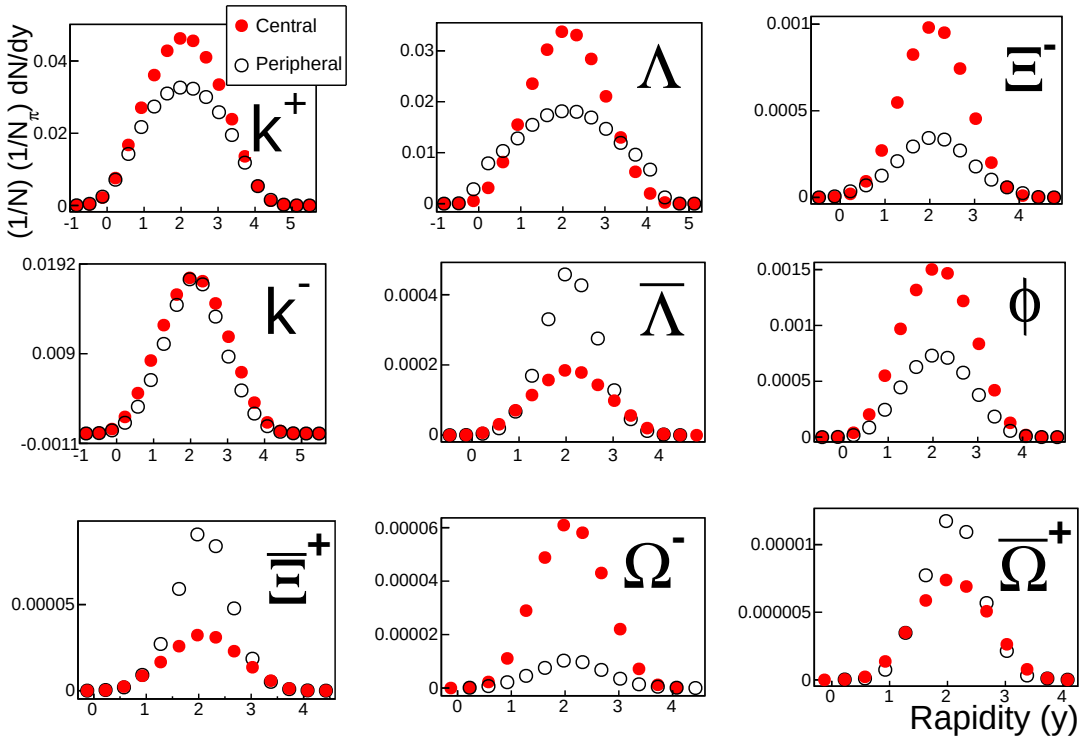

Fig. 5.3 Normalized rapidity distribution of particles containing leading and produced quarks for central as well as peripheral $Au+Au$ collisions at 30A GeV with UrQMD model. The errors are small and are within the symbol size.

impact parameter, as expected, the net-baryon number tends to populate the extreme rapidity spaces due to small overlap of the colliding partners. This increase in the population of baryon over anti-baryon at larger rapidities causes the broadening of the width of the rapidity distribution of the particles containing leading quarks (since their production is dependent on the distribution of u and d quarks). This may otherwise mean that at the studied energy, a large fraction of such particles are not pair produced.

Further, from Fig. 5.4 (right panel) it is also seen that for all but Ω^- particle, consisting of produced quarks only, the rapidity width decreases with decreasing centrality (or increasing impact parameter). Such decrease in the width of the rapidity distribution of these particles could be due to the decrease in the size of the central fireball with the increase of impact parameter. It is to be noted here that the observed behavior of centrality dependent rapidity width have already been seen for kaons and lambdas in the NA49 experimental data for 40A GeV Pb+Pb collisions [192, 215]. Moreover, Ω^-, whose all the constituent quarks are produced quarks only (sss), its production in UrQMD-3.3, in addition to string fragmentation, is also influenced by Ξ^- and Ξ^0 via $\Xi^- + K^- \rightarrow \Omega^- + \pi^-$, $\Xi^- + \bar{K^0} \rightarrow \Omega^- + \pi^0$, $\Xi^0 + K^- \rightarrow \Omega^- + \pi^0$, and $\Xi^0 + \bar{K^0} \rightarrow \Omega^- + \pi^+$. Both Ξ^- (dss) and Ξ^0 (uss) contain a leading quark as

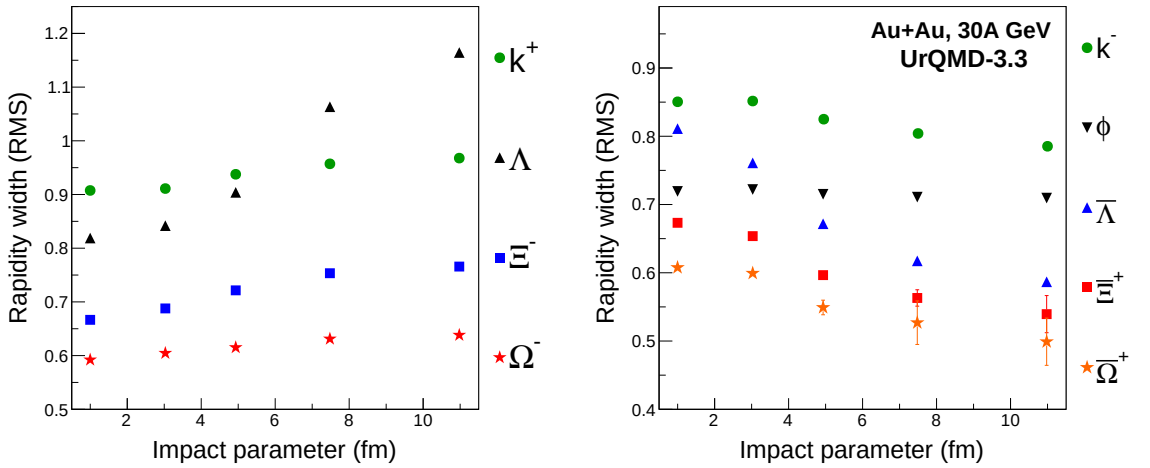

Fig. 5.4 Rapidity width as a function of impact parameter for identified particles for $Au+Au$ collisions at 30A GeV calculated using UrQMD model. The rapidity width or RMS has been calculated by parameterizing the rapidity distributions with a double Gaussian. The details of the parameterization can be found in Chapter 4 and as well as in the ref. [205].

one of its constituents. It is because of this influence of Ξ^- (Ξ^0), Ω^- is found to exhibit a different pattern other than its species member (having no leading quarks). To prevent the production of Ω^- from ΞK interaction, another 60 millions of events were generated by switching off the following reaction channels,

$\Xi^- + K^- \to \Omega^- + \pi^-$, $\Xi^- + \bar{K}^0 \to \Omega^- + \pi^0$, $\Xi^0 + K^- \to \Omega^- + \pi^0$, $\Xi^0 + \bar{K}^0 \to \Omega^- + \pi^+$, $\bar{\Xi}^+ + K^+ \to \bar{\Omega}^+ + \pi^+$, $\bar{\Xi}^+ + K^0 \to \bar{\Omega}^+ + \pi^0$, $\bar{\Xi}^0 + K^+ \to \bar{\Omega}^+ + \pi^0$, $\bar{\Xi}^0 + K^0 \to \bar{\Omega}^+ + \pi^-$

in the UrQMD event generator and the resulting rapidity dependent enhancement factor of Ω^- is replotted in Fig. 5.6. It can be readily seen from this figure that the generic rise and fall pattern of E_S, as seen for leading particles, is completely missing now for Ω^-. Even though the plot is not exactly symmetric which could be due to the fact that UrQMD does not symmetrize when it does kinematics in absence of the aforementioned reaction channels as is evident from the Fig. 5.7, the presence of a clear minimum around mid-rapidity can surely be not ruled out.

Further, in order to investigate the influence of string fragmentation scheme on the observed strangeness enhancement pattern, another 45 million events were generated by implementing the Lund-fragmentation [211] function as string fragmentation scheme for the produced particles in the UrQMD model. The Lund string fragmentation function is,

$$f(x) \propto \frac{1}{x}(1-x)^a \exp\left(-\frac{bm_T^2}{x}\right). \tag{5.5}$$

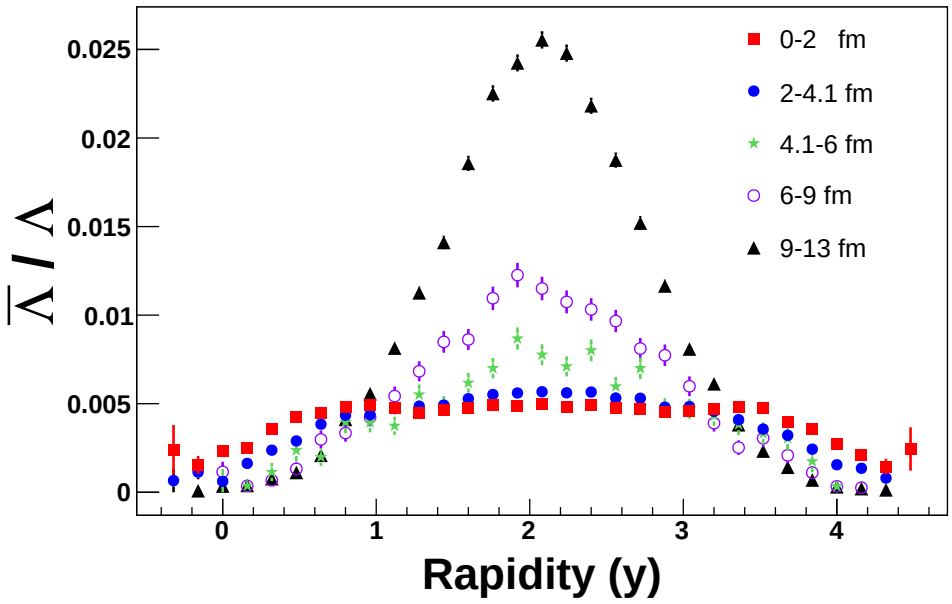

Fig. 5.5 $\bar{\Lambda}/\Lambda$ as a function of rapidity for different centrality interval in $Au+Au$ collisions at $E_{lab} = 30A$ GeV calculated using UrQMD model.

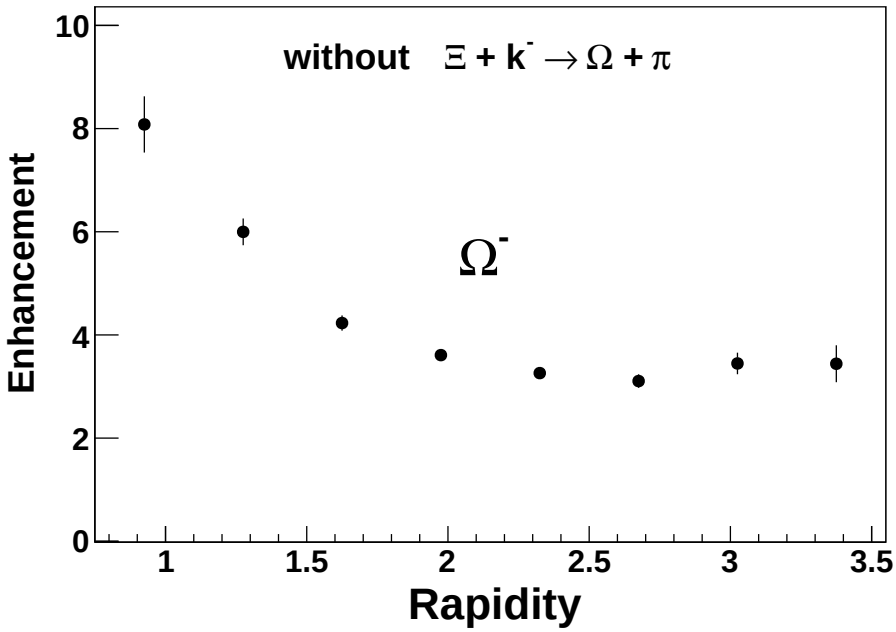

Fig. 5.6 Strangeness enhancement factor for Ω^- as a function of rapidity for $Au+Au$ collisions at $30A$ GeV.

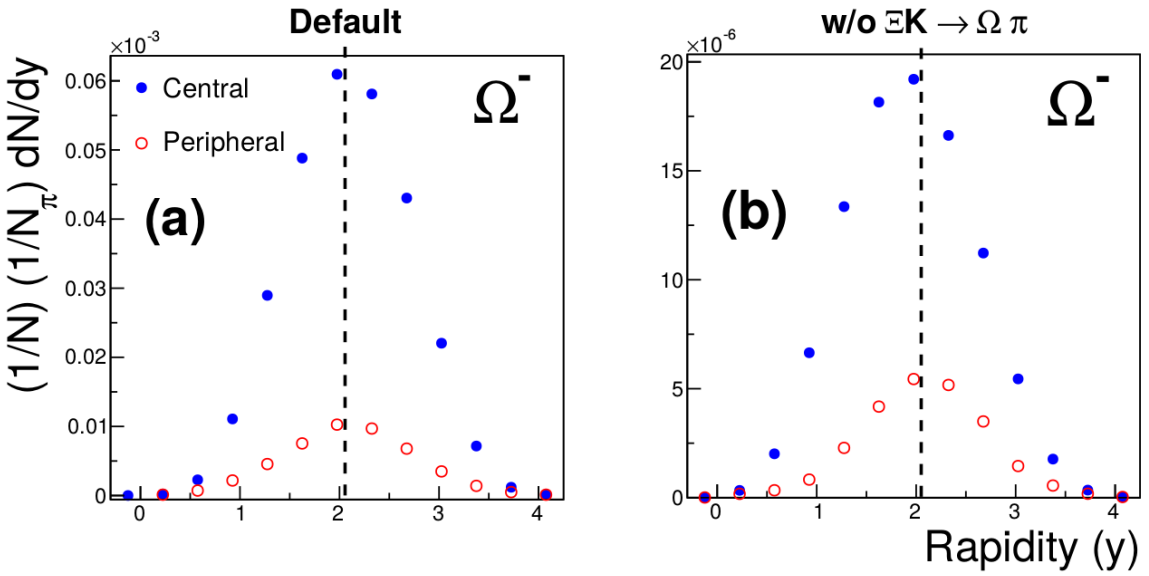

Fig. 5.7 Normalized rapidity distribution of Ω^- baryon in central and peripheral collisions (a) for default UrQMD and (b) by switching off the $\Xi K \rightarrow \Omega\pi$ channel in $Au+Au$ collision at 30A GeV. The errors are small and are within the symbol size.

where, a and b are the free parameters to be fixed by the experimental data. m_T represents the transverse mass of the produced hadron. The average squared transverse momentum i.e. $\langle p_T^2 \rangle$ of produced particle is proportional to the string tension κ. The two parameters a and b are approximately related to the string tension by the following relation [216],

$$\kappa \propto [b(2+a)]^{-1}. \tag{5.6}$$

Fig. 5.8 illustrates the rapidity dependent strangeness enhancement for the produced particles using Lund fragmentation model as the string fragmentation function scheme. It is clearly seen from the figure that similar to that of Field-Feynman fragmentation scheme (blue solid line in Fig. 5.2), the Lund model also predicted two distinctive rapidity dependent strangeness enhancement patterns for the particles containing and not containing leading quarks.

5.4 Summary

Strangeness enhancement factor of various produced particles containing and not containing leading quark(s) as one of the constituents is studied at various rapidity bins for $Au+Au$ collisions at 30A GeV. It is interesting to observe from this investigation that the pattern

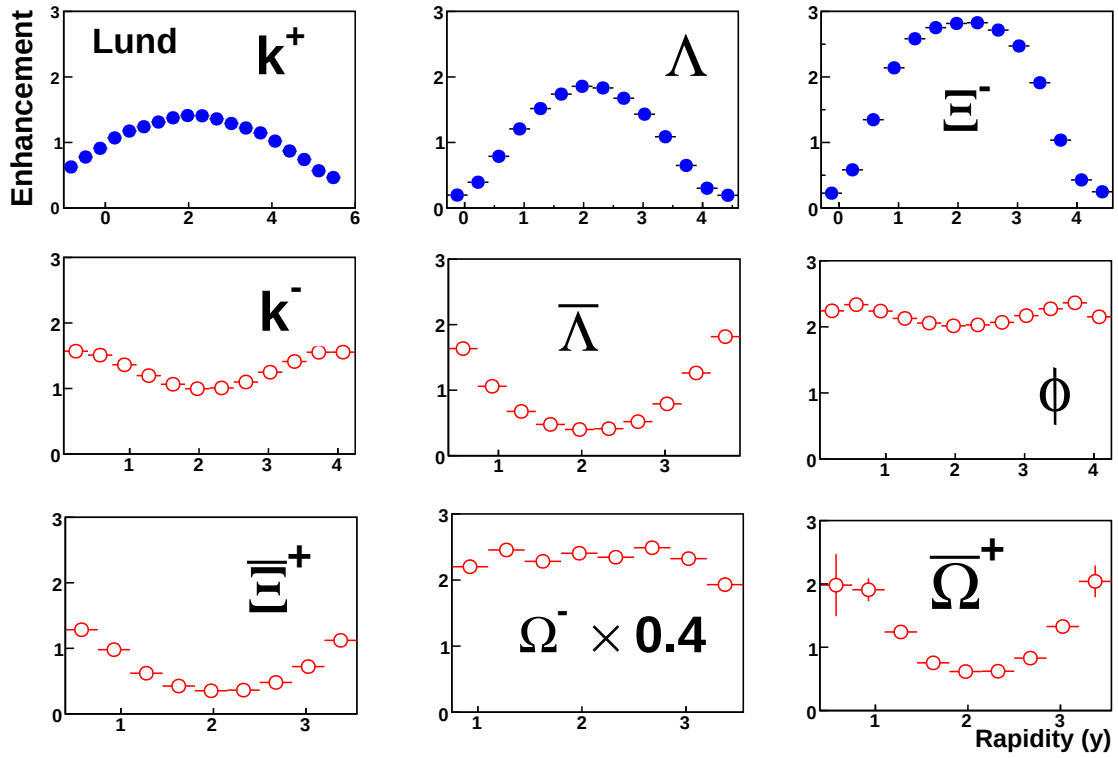

Fig. 5.8 Strangeness enhancement factor as a function of rapidity for particles containing at least one leading quark (filled circle) and particles containing only produced quarks (open circle) for Au + Au collisions at 30A GeV using Lund fragmentation function.

of rapidity dependent strangeness enhancement factor depends on the quark content of hadrons. At mid-rapidity, the strangeness enhancement factor is found to be maximum for the particles containing leading quarks while it shows a minimum at mid-rapidity for the particles containing produced quarks only. Such two distinctive patterns of variation of strangeness enhancement with rapidity have been attributed to the fact that the width of the rapidity distribution of the produced particles follows two different patterns with centrality (impact parameter) for particles containing and not containing leading quarks. This difference in the variation of width of rapidity distribution is attributed to the variation of net-baryon density with centrality. Further, the observed rapidity dependent strangeness enhancement pattern is found to be independent of the string fragmentation schemes considered for particle production.

6

Summary and conclusion

Electromagnetic probes (photons and dileptons) as discussed in Chapter 1, are believed to be the cleanest messengers of the fireball created in high-energy heavy-ion collisions. Among them, dilepton (di-muon and di-electron) detection is one of the priorities of the proposed CBM experiment to be held at FAIR, Darmstadt, Germany. In order to gather a detail information regarding the created matter, the CBM experiment is proposed to measure dileptons both from the decay of low mass vector mesons (LMVM) and J/ψ. MUon CHamber (MUCH) detector will be responsible for the detection of di-muons for the CBM experiment. A study has been performed to optimize the MUCH detector in terms of various optimization parameters i.e. hadron absorber material, the total absorber thickness, the individual absorber thickness, choice of the detector technology, their granularities etc. In SIS-300 configuration, the optimized MUCH detector consists of 6 hadron absorbers and 18 detector layers. The material of the first absorber is chosen as carbon with an optimized thickness of 60 cm, while the rest are chosen to be iron having thickness 20 cm, 20 cm, 30 cm, 35 cm, and 100 cm each. Because of having two distinct properties such as *low dead time* and *radiation hardness*, a micro-pattern detector called Gas Electron Multiplier (GEM) is chosen as the active detector component for MUCH. From the present investigation, the optimized granularity of the detector or the segmentation angle is found to be 1^0. Using the optimized detector setup, a performance study has also been conducted in terms of the

figure of merit i.e. signal reconstruction efficiency and S/B ratio. Suitable tracking algorithm and various quality criteria are imposed in order to subtract various hadronic and leptonic (decayed muons) backgrounds and to reconstruct probable primary muon tracks. While the *invariant mass* technique is employed in order to reconstruct signals, for background estimation, the *superevent* technique is adopted. The S/B ratio is estimated by calculating both signals and backgrounds around $\pm 2\sigma$ window of the signal peak. The S/B ratio and J/ψ reconstruction efficiency for central $Au + Au$ collisions are observed to be 0.84 and 16.20% respectively. The same for the minimum biased collisions are respectively found to be 16.92 and 15.2%. In both the cases, the J/ψ peak is clearly visible and is found to be above the continuum arising from the combinatorial background. Further, with this adopted MUCH configuration, the mass resolution of J/ψ is found to be 28.7 MeV/c^2. This value is far better than the previous muon detection experiments like NA50 and NA60 and existing experiment like CMS. The S/B ratio has further been improved by adding the TOF detector downstream of MUCH. The present optimized MUCH detector set-up, coupled with the TOF detector is, therefore, compatible enough for the J/ψ measurement at FAIR energies.

An attempt has also been made to ascertain the feasibility of the measurement of the effective temperature of the fireball from the dilepton spectra using the proposed MUCH detector. The study has been conducted within the `CBMROOT` framework, where, the signal (J/ψ) and the hadronic background were generated using PLUTO and UrQMD event generators respectively. The optimized SIS-100b geometry along with the newly optimized beam pipe have been used for the present study. All the necessary quality criteria, as discussed in Chapter 2, have been imposed during the reconstruction of the tracks so as to achieve a good signal reconstruction efficiency and high S/B ratio. The transverse mass distribution of the identified J/ψ is parametrized with the help of an exponential function (Eqn. 3.4) in order to calculate the effective temperature T_{eff}. To see the effect of variation of bin-width and fitting m_t-range on the effective temperature, for each bin-width value, different fitting ranges of the transverse mass spectra have been considered for the calculation of T_{eff}. In order to compare the effective temperature of the input and the reconstructed signal, the best-fitted T_{eff} value (i.e. with best χ^2/NDF) has been considered. The values of T_{eff} for reconstructed J/ψ are found to be in agreement with the input temperature within the uncertainty (see Table 6.1) indicating the usefulness of MUCH design for the CBM experiment. Further, J/ψ reconstruction efficiency is calculated and is plotted as a function of transverse momentum P_T. The reconstruction efficiency is found to be almost independent of the transverse momentum over the entire studied range. Moreover, from the present study, the observed dependence of the fireball temperature on the bin width of transverse mass is found to be well within the estimated error.

$J/\psi \rightarrow \mu^+\mu^-$		Bin width (MeV)		
		500	160	100
Input	T_{eff} (MeV)	172.6 ± 1.30	173.5 ± 0.5	173.6 ± 1.3
Reconstructed	T_{eff} (MeV)	174.8 ± 10.06	174.2 ± 4.6	182.8 ± 9.7

Table 6.1 The extracted fitting parameter i.e. temperature (T_{eff}) selected on the basis of χ^2/NDF for J/ψ meson with different m_t bin width (both for input and reconstructed signal).

As already discussed, the CBM experiment at FAIR will be conducted in order to explore the QCD phase diagram at the region of high baryon density and moderate temperature. The beam energies of the FAIR accelerator is chosen in such a way that a high baryon density of the order of 5-10 times the ground state nuclear matter density could be created. At such extreme baryon density, the inherent properties of hadrons are expected to modify and in fact, the effects which couple to baryon density would be very prominent. Considering these facts, in the present investigation, an attempt has been made to study the width of the rapidity distribution of the produced mesons and baryons at FAIR energies and results are presented in Chapter 4. One of the important observation of NA49 experiment regarding the width of the rapidity distribution was made by the Friese *et al.* using the data from Pb+Pb collisions. They observed a scaling behavior of the width of the rapidity distribution with beam rapidity. Also, they found that the width of the rapidity distribution follows an inverse relationship with the mass. It is worthwhile to mention that as Λ baryon has contamination from Σ^0 decay, their results include $\overline{\Lambda}$ instead of Λ as both being are of the same mass. Friese *et al.* describe their results to have a kinematical origin. In the present study, a comparison of the rapidity distribution of a few hadrons such as π^-, k^-, ϕ, and Λ produced in UrQMD generated $Au+Au$ collisions at 10, 20, 30 and 40A GeV were made with the existing experimental data. It has clearly been seen from the present study that lighter mesons like π^-, k^- show a fair agreement between experimental data and UrQMD prediction at all energies. However, for heavier meson like ϕ, as the energy of collision increases, there is a considerable disagreement between the experimental data and UrQMD predicted values. This result can be understood from the fact that, at lower energies, although hadronic interactions are responsible for ϕ meson production, yet, at higher energies, there might be a significant contribution from the non-hadronic channels. In this work, the rapidity width has been extracted by parameterizing the rapidity distribution with the help of a double Gaussian function (see Eqn. 4.14). The extracted width of the rapidity distribution is seen to follow a scaling behavior with beam rapidity. Additionally, the variation of the width of the rapidity distribution with beam rapidity follows a mass ordering separately for mesons and baryons. The mass ordering is violated if the studied hadrons are taken together. Experimental data of

NA49 also exhibit the same behavior if Λ instead of $\bar{\Lambda}$ is taken into consideration (Fig. 6.1). It may be mentioned here that the disagreement between the ϕ meson rapidity distribution of the experimental and UrQMD generated values has found to have insignificant effect on the scaling behavior of rapidity width and has been discussed in Chapter 4 as well as in the published work of the present investigation (Phys. Rev. C 89:054910, 2014).

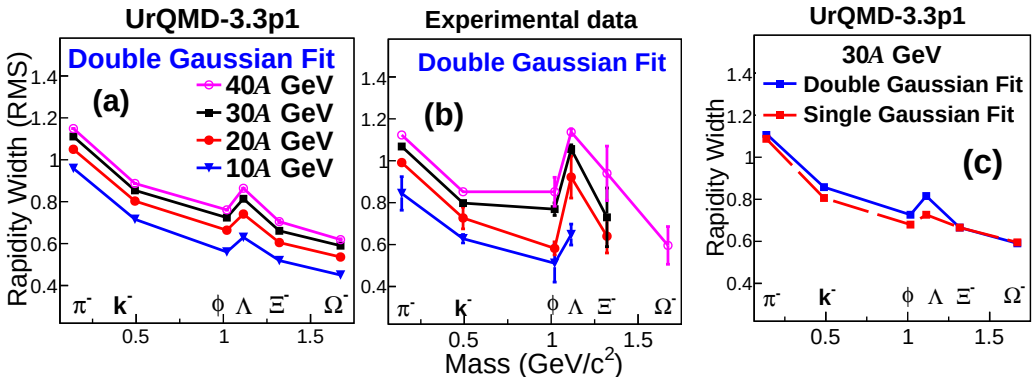

Fig. 6.1 Variation of rapidity width as a function of mass of the produced particles in central $Au+Au$ collision at FAIR energies for UrQMD and experimental data. The left and middle panels correspond to double Gaussian parametrization while the right panel corresponds to a comparison of single and double Gaussian fits for 30A GeV. The errors seen in the figure correspond to the statistical error.

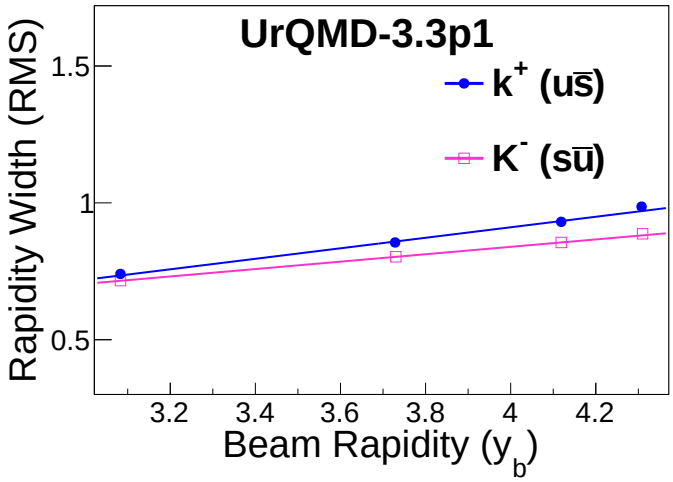

Fig. 6.2 Rapidity widths of K^+ and K^- as a function of beam rapidity for UrQMD-3.3p1 generated central Au+Au collision.

This separate mass ordering is attributed to the fact that, unlike hadrons containing produced quarks only, the width of the leading hadrons' rapidity distribution is being influenced by kinematic consideration as well as the net-baryon density. It has also been observed that

the rapidity distribution of mesons containing leading quarks, e.g., K^+ ($u\bar{s}$), have also been affected by the net-baryon density as is evident from the width of the rapidity distribution of both K^+ ($u\bar{s}$) and K^- ($s\bar{u}$) (Fig. 6.2).

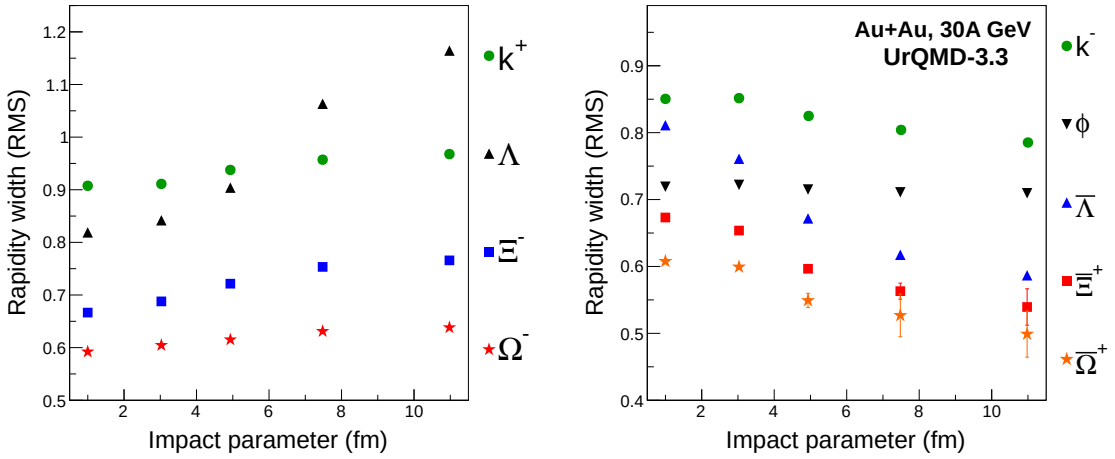

Fig. 6.3 Rapidity width as a function of impact parameter for identified particles for $Au+Au$ collision at 30A GeV calculated using UrQMD model [205].

Predicted by Rafelski and Müller in the early 80's, strangeness enhancement is considered to be one of the potential signatures of QGP. This signature has been studied by several heavy-ion experiments like NA49, NA57, STAR, ALICE etc. Due to the limitation of the detector acceptance, all such heavy-ion experiments could measure the strangeness enhancement at mid-rapidity only. Such measurements have assumed a global conservation of strangeness. However, Steinheimer *et al.* from UrQMD calculation predicted that strangeness is unevenly distributed over the rapidity space leading to a local violation of strangeness conservation. The present study on rapidity dependent strangeness enhancement (E_S) reveals that the pattern of rapidity dependent E_S depends strongly on the quark content of hadrons. The strangeness enhancement factor is found to be maximum at mid-rapidity for the particles containing leading quarks. On the other extreme, the enhancement is observed to be minimum at mid-rapidity for the particles containing produced quarks only. Such two distinctive patterns of rapidity dependent strangeness enhancement have been attributed to the fact that, the widths of the rapidity distribution of the produced particles follow two different patterns with centrality (impact parameter) for particles containing or not containing leading quarks (Fig. 6.3). This difference in the variation of the width of rapidity distribution of particles containing leading and produced quarks is attributed to the variation of net-baryon density with centrality. Further, the observed rapidity dependent strangeness enhancement pattern is seen to be independent of the string fragmentation mechanism. This unique prediction of

the string model like UrQMD could well be tested in the near future with the FAIR-CBM experiment.

References

[1] S. L. Glashow, Nucl. Phys. **22**, 579 (1961).

[2] S. Weinberg, Phys. Rev. Lett. **19**, 1264 (1967).

[3] S. L. Glashow, J. Iliopoulos, and L. Maiani, Phys. Rev. D **2**, 1285 (1970).

[4] G. Aad et al., Physics Letters B **716**, 1 (2012), ISSN 0370-2693.

[5] S. Chatrchyan et al., Physics Letters B **716**, 30 (2012), ISSN 0370-2693.

[6] H. Fritzsch, in *QCD 20 Years Later: Proceedings, Workshop, Aachen, Germany, June 9-13* (1992), pp. 827–852.

[7] *Standard Model of Elementary Particles* (2016), https://commons.wikimedia.org/wiki/File:Standard_Model_of_Elementary_Particles_af.svg.

[8] F. Wilczek, Phys. Today **53N8**, 22 (2000).

[9] C. Amsler et al., Tech. Rep. CERN-PPE-91-215, CERN, Geneva (1991).

[10] D. J. Griffiths, *Introduction to elementary particles; 2nd rev. version*, Physics textbook (Wiley, New York, NY, 2008).

[11] D. J. Gross and F. Wilczek, Phys. Rev. Lett. **30**, 1343 (1973).

[12] H. D. Politzer, Phys. Rev. Lett. **30**, 1346 (1973).

[13] J. C. Collins and M. J. Perry, Phys. Rev. Lett. **34**, 1353 (1975).

[14] E. V. Shuryak, Sov. Phys. JETP **47**, 212 (1978), [Zh. Eksp. Teor. Fiz.74,408(1978)].

[15] F. Karsch, Nuclear Physics A **698**, 199 (2002), ISSN 0375-9474, 15th Int. Conf. on Ultra-Relativistic Nucleus-Nucleus Collisions (Quark Matter 2001).

[16] E. V. Shuryak, Physics Reports **61**, 71 (1980), ISSN 0370-1573.

[17] F. Karsch, E. Laermann, and A. Peikert, Nuclear Physics B **605**, 579 (2001), ISSN 0550-3213.

[18] K. Rajagopal and F. Wilczek (2000), hep-ph/0011333.

[19] Z. Fodor and S. D. Katz, Prog. Theor. Phys. Suppl. **153**, 86 (2004), hep-lat/0401023.

[20] S. Ejiri, C. R. Allton, S. J. Hands, O. Kaczmarek, F. Karsch, E. Laermann, and C. Schmidt, Prog. Theor. Phys. Suppl. **153**, 118 (2004), hep-lat/0312006.

[21] S. Borsanyi et al., JHEP **11**, 077 (2010), 1007.2580.

[22] A. Bazavov, P. Petreczky, and T. H. collaboration, Journal of Physics: Conference Series **230**, 012014 (2010).

[23] P. Bicudo, N. Cardoso, and M. Cardoso, PoS **BORMIO2011**, 062 (2011), 1105.0063.

[24] Z. Fodor, Nucl. Phys. **A715**, 319 (2003), hep-lat/0209101.

[25] T. D. Lee, Rev. Mod. Phys. **47**, 267 (1975).

[26] H. A. Gustafsson, H. H. Gutbrod, B. Kolb, H. Löhner, B. Ludewigt, A. M. Poskanzer, T. Renner, H. Riedesel, H. G. Ritter, A. Warwick, et al., Phys. Rev. Lett. **52**, 1590 (1984).

[27] S. Blyth, PhD thesis, University of Cape Town, South Africa (2007).

[28] G. Paic, AIP Conf. Proc. **1116**, 111 (2009), 0901.1884.

[29] C.-Y. Wong, Phys. Rev. **C78**, 054902 (2008), 0808.1294.

[30] J. Adam et al. (ALICE Collaboration), Phys. Rev. C **94**, 034903 (2016).

[31] C. Collaboration, *Compressed Baryonic Matter Experiment - Technical Status Report* (2005), https://www-alt.gsi.de/documents/DOC-2005-Feb-447.html.

[32] P. S. C. Collaboration), J. Phys.: Conf. Ser. **50**, 257 (2006).

[33] P. Senger, Cent. Eur. J. Phys. **10**, 1289 (2012).

[34] C. H. et al. (CBM Collaboration), Nucl. Phys. A **749**, 141 (2005).

[35] V. Friese, Nucl. Phys. A **774**, 377 (2006).

[36] I. Arsene et al. (BRAHMS), Nucl. Phys. **A757**, 1 (2005), nucl-ex/0410020.

[37] S. S. Adler et al. (PHENIX), Phys. Rev. **C71**, 034908 (2005), [Erratum: Phys. Rev.C71,049901(2005)], nucl-ex/0409015.

[38] B. B. Back et al., Nucl. Phys. **A757**, 28 (2005), nucl-ex/0410022.

[39] J. Adams et al. (STAR), Nucl. Phys. **A757**, 102 (2005), nucl-ex/0501009.

[40] P. Foka and M. A. Janik, Reviews in Physics **1**, 154 (2016), ISSN 2405-4283.

[41] P. Staszel (BRAHMS), in *Proceedings, 40th International Symposium on Multiparticle Dynamics (ISMD 2010): Antwerp, Belgium, September 21-25, 2010* (2010), pp. 325–331.

[42] F. Videbæk and O. Hansen, Phys. Rev. C **52**, 2684 (1995).

[43] I. C. Arsene et al. (BRAHMS), Phys. Lett. **B677**, 267 (2009), 0901.0872.

[44] A. Andronic, P. Braun-Munzinger, and J. Stachel, Nucl. Phys. **A772**, 167 (2006), nucl-th/0511071.

[45] B. Friman, C. Hohne, J. Knoll, S. Leupold, J. Randrup, R. Rapp, and P. Senger, Lect. Notes Phys. **814**, pp. 980 (2011).

[46] J. S. P. Braun-Munzinger, K. Redlich, *Quark Gluon Plasma 3* (World Scientific, Singapore, 2004), p. p. 491.

[47] P. Braun-Munzinger, J. Stachel, J. Wessels, and N. Xu, Physics Letters B **344**, 43 (1995), ISSN 0370-2693.

[48] P. Braun-Munzinger, J. Stachel, J. Wessels, and N. Xu, Physics Letters B **365**, 1 (1996), ISSN 0370-2693.

[49] P. Braun-Munzinger, I. Heppe, and J. Stachel, Physics Letters B **465**, 15 (1999), ISSN 0370-2693.

[50] R. Averbeck, R. Holzmann, V. Metag, and R. S. Simon, Phys. Rev. C **67**, 024903 (2003).

[51] Z. Fodor and S. D. Katz, Journal of High Energy Physics **2004**, 050 (2004).

[52] C. M. Hung and E. V. Shuryak, Phys. Rev. **C57**, 1891 (1998), hep-ph/9709264.

[53] L. V. Hove, Physics Letters B **118**, 138 (1982), ISSN 0370-2693.

[54] J. Rafelski and B. Müller, Phys. Rev. Lett. **48**, 1066 (1982).

[55] P. Koch, B. Muller, and J. Rafelski, Physics Reports **142**, 167 (1986), ISSN 0370-1573.

[56] *Strangeness production* (2009), https://en.wikipedia.org/wiki/Strangeness_production#/media/File:Strange_production_5.gif.

[57] F. Antinori et al. (NA57), J. Phys. **G32**, 427 (2006), nucl-ex/0601021.

[58] B. I. Abelev et al. (STAR), Phys. Lett. **B673**, 183 (2009), 0810.4979.

[59] A. R. Timmins (STAR), J. Phys. **G36**, 064006 (2009), 0812.4080.

[60] S. Voloshin and Y. Zhang, Z. Phys. **C70**, 665 (1996), hep-ph/9407282.

[61] G. M. Welke, M. Prakash, T. T. S. Kuo, S. Das Gupta, and C. Gale, Phys. Rev. C **38**, 2101 (1988).

[62] C. Hartnack, J. Aichelin, H. Stöcker, and W. Greiner, Physics Letters B **336**, 131 (1994), ISSN 0370-2693.

[63] P. Danielewicz, R. A. Lacey, P.-B. Gossiaux, C. Pinkenburg, P. Chung, J. M. Alexander, and R. L. McGrath, Phys. Rev. Lett. **81**, 2438 (1998).

[64] A. Andronic, Nuclear Physics A **661**, 333 (1999), ISSN 0375-9474.

[65] P. F. Kolb, J. Sollfrank, P. V. Ruuskanen, and U. W. Heinz, Nucl. Phys. **A661**, 349 (1999), nucl-th/9907025.

[66] T. Matsui and H. Satz, Phys. Lett. **B178**, 416 (1986).

[67] S. Arumugam, *J/ψ Suppression* (2006), http://www.uio.no/studier/emner/matnat/fys/FYS4530/v06/undervisningsmateriale/Talk.pdf.

[68] D. de Florian and R. Sassot, Phys. Rev. **D69**, 074028 (2004), hep-ph/0311227.

[69] K. Eskola, V. Kolhinen, and R. Vogt, Nuclear Physics A **696**, 729 (2001), ISSN 0375-9474.

[70] A. Peshier, B. Kämpfer, O. P. Pavlenko, and G. Soff, Phys. Rev. D **54**, 2399 (1996).

[71] A. Peshier, B. Kämpfer, and G. Soff, Phys. Rev. C **61**, 045203 (2000).

[72] A. Peshier, B. Kämpfer, and G. Soff, Phys. Rev. D **66**, 094003 (2002).

[73] A. Lardeux, Journal of Physics: Conference Series **446**, 012042 (2013).

[74] U. W. Heinz and M. Jacob (2000), nucl-th/0002042.

[75] R. S. Bhalerao, in *Proceedings, 1st Asia-Europe-Pacific School of High-Energy Physics (AEPSHEP): Fukuoka, Japan, October 14-27, 2012* (2014), pp. 219–239, 1404.3294, URL https://inspirehep.net/record/1290394/files/arXiv:1404.3294.pdf.

[76] S. Chatrchyan et al. (CMS Collaboration), Phys. Rev. Lett. **113**, 132301 (2014).

[77] S. Sarkar, H. Satz, and B. Sinha, Lect. Notes Phys. **785**, pp. 369 (2010).

[78] L. Bhattacharya, R. Ryblewski, and M. Strickland, Phys. Rev. **D93**, 065005 (2016), 1507.06605.

[79] M. Gyulassy, in *Structure and dynamics of elementary matter. Proceedings, NATO Advanced Study Institute, Camyuva-Kemer, Turkey, September 22-October 2, 2003* (2004), pp. 159–182, nucl-th/0403032.

[80] *FAIR Green Paper: The Modularized Start Version* (2009), https://www.gsi.de/documents/DOC-2009-Nov-124-1.pdf.

[81] C. S. H. Stoecker, Rom. Journ. Phys **58**, 1023 (2013).

[82] B. Sinha, Journal of Radioanalytical and Nuclear Chemistry **290**, 5 (2011), ISSN 1588-2780.

[83] *Appa - atomic, plasma physics and applications.* (2009 (accessed February 3, 2014)), http://www.fair-center.eu/for-users/experiments/appa-external.htmlb.

[84] U. Wiedner, Nuclear Physics B - Proceedings Supplements **147**, 119 (2005), ISSN 0920-5632.

[85] C. Schwarz and the PANDA Collaboration, Journal of Physics: Conference Series **374**, 012003 (2012).

[86] T. Nilsson and for the NUSTAR collaboration, Physica Scripta **2015**, 014070 (2015).

[87] *Facility for Antiproton and Ion Research* (2016), URL http://www.fair-center.eu/uploads/pics/FAIR_3DModel_72dpi_Legend_01.jpg.

[88] W. Barth, W. Bayer, L. Dahl, L. Groening, S. Richter, and S. Yaramyshev, Nuclear Instruments and Methods in Physics Research Section A: Accelerators, Spectrometers, Detectors and Associated Equipment **577**, 211 (2007), ISSN 0168-9002, proceedings of the 16th International Symposium on Heavy Ion Inertial FusionHIF 06.

[89] W. Ehehalt and W. Cassing, Nucl. Phys. **A602**, 449 (1996).

[90] J. Geiss, W. Cassing, and C. Greiner, Nucl. Phys. **A644**, 107 (1998), nucl-th/9805012.

[91] W. Cassing and E. L. Bratkovskaya, Phys. Rept. **308**, 65 (1999).

[92] A. Prakash, P. P. Bhaduri, S. Chattopadhyay, A. Dubey, and B. K. Singh, Nucl. Phys. **A862-863**, 493 (2011), 1102.0882.

[93] J. Heuser, W. Muller, V. Pugatch, P. Senger, C. J. Schmidt, C. Sturm, and U. Frankenfeld, eds., *[GSI Report 2013-4] Technical Design Report for the CBM Silicon Tracking System (STS)* (GSI, Darmstadt, 2013).

[94] S. Chattopadhyay, Y. P. Viyogi, P. Senger, W. F. J. Müller, Schmidt, and C. J. C. Collaboration), eds., *Technical Design Report for the CBM : Muon Chambers (MuCh)* (GSI, Darmstadt, 2015).

[95] *CBM 3D models* (2016), http://www.fair-center.eu/for-users/experiments/cbm/introduction.html.

[96] K. A. Olive et al. (Particle Data Group), Chin. Phys. **C38**, 090001 (2014).

[97] S. Ahmad, P. Bhaduri, H. Jahan, A. Senger, R. Adak, S. Samanta, A. Prakash, K. Dey, A. Lebedev, E. Kryshen, et al., Nuclear Instruments and Methods in Physics Research Section A: Accelerators, Spectrometers, Detectors and Associated Equipment **775**, 139 (2015), ISSN 0168-9002.

[98] V. Friese, *Simulations for CBM* (2008), https://www-alt.gsi.de/documents/DOC-2008-Mar-117.html.

[99] R. Brun and F. Rademakers, Nuclear Instruments and Methods in Physics Research Section A: Accelerators, Spectrometers, Detectors and Associated Equipment **389**, 81 (1997), ISSN 0168-9002.

[100] S. A. Bass et al., Prog. Part. Nucl. Phys. **41**, 255 (1998), [Prog. Part. Nucl. Phys.41,225(1998)], nucl-th/9803035.

[101] M. Bleicher et al., J. Phys. **G25**, 1859 (1999), hep-ph/9909407.

[102] H. Petersen, M. Bleicher, S. A. Bass, and H. Stocker (2008), 0805.0567.

[103] I. Fröhlich, T. Galatyuk, R. Holzmann, J. Markert, B. Ramstein, P. Salabura, and J. Stroth, Journal of Physics: Conference Series **219**, 032039 (2010).

[104] T. Sjostrand, S. Mrenna, and P. Z. Skands, JHEP **05**, 026 (2006), hep-ph/0603175.

[105] T. Sjostrand, S. Mrenna, and P. Z. Skands, Comput. Phys. Commun. **178**, 852 (2008), 0710.3820.

[106] R. Brun, F. Bruyant, F. Carminati, S. Giani, M. Maire, A. McPherson, G. Patrick, and L. Urban (1994).

[107] S. Agostinelli et al., Nuclear Instruments and Methods in Physics Research Section A: Accelerators, Spectrometers, Detectors and Associated Equipment **506**, 250 (2003), ISSN 0168-9002.

[108] M. Galassi, J. Theiler, and B. Gough, *Gnu scientific library – design document* (2016), https://www.gnu.org/software/gsl/design/gsl-design.html.

[109] L. Lonnblad, *Clhep - a class library for high energy physics* (2008), http://proj-clhep.web.cern.ch/proj-clhep/.

[110] B. Dawes, D. Abrahams, and R. Rivera, *Boost c++ libraries* (2007), http://www.boost.org/.

[111] R. Brun and F. Rademakers, Nucl. Instrum. Meth. **A389**, 81 (1997).

[112] T. Sjostrand, p. 25 p (1991), URL https://cds.cern.ch/record/226013.

[113] S. Lehti (2016), Computing Methods In High Energy Physics, Spring 2016, Helsinki Institute of Physics (Lecture 8), URL http://www.helsinki.fi/~slehti/ComputingMethodsInHEP/CompInHEP_lect8.pdf.

[114] D. B. M. Al-Turany and I. Koenig, Proceedings, Computing in High Energy and Nuclear Physics (CHEP-2006) (2006).

[115] M. Al-Turany, D. Bertini, R. Karabowicz, D. Kresan, P. Malzacher, T. Stockmanns, and F. Uhlig, Journal of Physics: Conference Series **396**, 022001 (2012).

[116] M. Al-Turany, D. Bertini, and I. Koenig (2006), computing in High Energy and Nuclear Physics (CHEP 06), Feb 13-17 2006, TIFR Mumbai (India).

[117] M. A.-T. et. al, J. Phys.: Conf. Ser. **396**, 022001 (2012).

[118] M. Bussa, Czechoslovak Journal of Physics **55**, A279 (2005), ISSN 0011-4626.

[119] D. Bettoni, Journal of Physics: Conference Series **9**, 309 (2005).

[120] D. Bertini, Journal of Physics: Conference Series **331**, 032036 (2011), URL http://stacks.iop.org/1742-6596/331/i=3/a=032036.

[121] P. R. et. al., Journal of Physics: Conference Series **420**, 012092 (2013).

[122] K. Dey, S. Chattopadhyay, and B. Bhattacharjee, CBM progress report 2013 (2014).

[123] W. R. Leo, *Techniques for Nuclear and Particle Physics Experiments: A How to Approach* (1987).

[124] I. Smirnov, Nuclear Instruments and Methods in Physics Research Section A: Accelerators, Spectrometers, Detectors and Associated Equipment **554**, 474 (2005), ISSN 0168-9002.

[125] M. Ryzhinskiy (2007), cBM Collaboration Meeting September 25-28, 2007, Dresden, Germany, URL https://www.hzdr.de/workshops/CBM/uploads/2007-09-27/15:40:00_M._Ryzhinskiy_(SPbSPU)_1.ppt.

[126] E. Kryshen and M. Ryzhinskiy (2009), first seminar of FRRC Fellows FAIR - Russian Research Center, June 9-10, 2009, Moscow, URL web-docs.gsi.de/~kryshen/presentations/mryzhinskiy_09.06.2009.ppt.

[127] I. Kisel, Nucl. Instrum. Meth. **A566**, 85 (2006).

[128] A. Lebedev, C. Hohne, I. Kisel, and G. Ososkov, *Status of the global track reconstruction algorithm for the cbm experiment*.

[129] A. Lebedev, C. Hohne, I. Kisel, G. Ososkov, and the Cbm collaboration, Journal of Physics: Conference Series **219**, 032048 (2010).

[130] G. Welch and G. Bishop, in *Computer Graphics, Annual Conference on Computer Graphics & Interactive Techniques* (2001), pp. 12–17.

[131] S. Chatrchyan et al. (CMS), JHEP **05**, 063 (2012), 1201.5069.

[132] B. Abelev et al. (ALICE), Phys. Rev. Lett. **109**, 072301 (2012), 1202.1383.

[133] C. Hohne (CBM), Nucl. Phys. **A931**, 735 (2014).

[134] L. D. McLerran and T. Toimela, Phys. Rev. D **31**, 545 (1985).

[135] R. D. Pisarski, Phys. Lett. **B110**, 155 (1982).

[136] G. E. Brown and M. Rho, Phys. Rept. **363**, 85 (2002), hep-ph/0103102.

[137] R. Rapp and J. Wambach, Adv. Nucl. Phys. **25**, 1 (2000), hep-ph/9909229.

[138] R. Rapp, J. Wambach, and H. van Hees, Landolt-Bornstein **23**, 134 (2010), 0901.3289.

[139] R. Arnaldi et al. (NA60 Collaboration), Phys. Rev. Lett. **100**, 022302 (2008).

[140] I. G. Bearden et al. (The NA44 Collaboration), Phys. Rev. Lett. **78**, 2080 (1997).

[141] M. Gazdzicki and M. I. Gorenstein, Phys. Lett. **B517**, 250 (2001), hep-ph/0103010.

[142] R. Hagedorn, Nuovo Cim. Suppl. **3**, 147 (1965).

[143] J. K. Nayak, Ph.D. thesis, Homi Bhabha National Institute, Department of Physical Sciences (2013).

[144] E. Bratkovskaya, Nuclear Physics A **931**, 194 (2014), ISSN 0375-9474, Quark Matter 2014XXIV International Conference On Ultrarelativistic Nucleus-Nucleus Collisions.

[145] T. Sakaguchi, Pramana **84**, 845 (2015), 1401.2481.

[146] E. B. Bratkovskaya (2014), xXIV Quark Matter conference, May 19-24 2014, Darmstadt (Germany), URL https://indico.cern.ch/event/219436/contributions/1523399/attachments/355980/495719/Bratkovskaya_QM14.pdf.

[147] R. Rapp, J. Wambach, and H. van Hees, *The Chiral Restoration Transition of QCD and Low Mass Dileptons* (Springer Berlin Heidelberg, Berlin, Heidelberg, 2010), pp. 134–175, ISBN 978-3-642-01539-7.

[148] J. Goldhaber, *Bevalac Had 40-Year Record of Historic Discoveries* (1992), http://www2.lbl.gov/Science-Articles/Archive/Bevalac-nine-lives.html.

[149] R. J. Porter et al. (The DLS Collaboration), Phys. Rev. Lett. **79**, 1229 (1997).

[150] W. K. Wilson et al. (The DLS Collaboration), Phys. Rev. C **57**, 1865 (1998).

[151] P. Salabura et al., Nuclear Physics A **749**, 150 (2005), ISSN 0375-9474.

[152] M. Masera (HELIOS), Nucl. Phys. **A590**, 93C (1995).

[153] E. Scomparin et al. (NA50), Nucl. Phys. **A610**, 331C (1996).

[154] G. Agakichiev et al. (CERES Collaboration), Phys. Rev. Lett. **75**, 1272 (1995).

[155] P. Wurm et al., Nuclear Physics A **590**, 103 (1995), ISSN 0375-9474.

[156] H. K. Wohri, Ph.D. thesis, Vienna, Tech. U. (2004).

[157] K. Dey, P. P. Bhaduri, S. Chattopadhyay, and B. Bhattacharjee, CBM progress report 2014 (2015).

[158] S. Ahmad et al., CBM progress report 2015 (2016).

[159] C. Y. Wong, *Introduction to high-energy heavy ion collisions* (1995), ISBN ISBN-9789810202637, singapore: World Scientific (1994) 516 p.

[160] S. A. Bass, M. Gyulassy, H. Stoecker, and W. Greiner, J. Phys. **G25**, R1 (1999), hep-ph/9810281.

[161] S. Scherer et al., Progress in Particle and Nuclear Physics **42**, 279 (1999), ISSN 0146-6410.

[162] I. C. Arsene, L. V. Bravina, W. Cassing, Y. B. Ivanov, A. Larionov, J. Randrup, V. N. Russkikh, V. D. Toneev, G. Zeeb, and D. Zschiesche, Phys. Rev. C **75**, 034902 (2007).

[163] S. Vogel, J. Phys.: Conf. Ser. **426**, 012012 (2013).

[164] Y. M. Kohsuke Yagi, Tetsuo Hatsuda, *Quark-Gluon Plasma: From Big Bang to Little Bang* (Cambridge University Press, 2005), chap. 11, pp. 274–275.

[165] G. E. Bruno, in *Proceedings, 18th International Conference on Ultra-Relativistic Nucleus-Nucleus Collisions (Quark Matter 2005)* (2005), nucl-ex/0511022.

[166] M. Jeżrabek and M. Różańska, Physics Letters B **175**, 206 (1986), ISSN 0370-2693.

[167] J. L. Klay et al. (E895 Collaboration), Phys. Rev. Lett. **88**, 102301 (2002).

[168] B. Mohanty and J.-e. Alam, Phys. Rev. C **68**, 064903 (2003).

[169] P. K. Netrakanti and B. Mohanty, Phys. Rev. C **71**, 047901 (2005).

[170] L. A. et al. (E802 Collaboration), Phys. Rev. C **57**, R466 (1998).

[171] L. A. et al. (E802 Collaboration), Phys. Rev. C **58**, 3523 (1998).

[172] L. A. et al. (E802 Collaboration), Phys. Rev. C **59**, 2173 (1999).

[173] J. B. et al. (E877 Collaboration), Phys. Rev. C **63**, 014902 (2000).

[174] S. A. et al. (E896 Collaboration), Phys. Rev. Lett. **88**, 062301 (2002).

[175] B. B. B. et al. (E917 Collaboration), Phys. Rev. C. **69**, 054901 (2004).

[176] J. Stachel, Nucl. Phys. **A610**, 509C (1996).

[177] A. M. et al. (NA49 Collaboration), Nucl. Phys. A **715**, 453c (2002).

[178] S. V. A. et al. (NA49 Collaboration), Phys. Rev. C **66**, 054902 (2002).

[179] C. A. et al. (NA49 Collaboration), Phys. Rev. C **78**, 044907 (2008).

[180] C. A. et al. (NA49 Collaboration), Phys. Rev. C **78**, 034918 (2008).

[181] R. L. et al. (E877 Collaboration), Nucl. Phys. A **610**, 152c (1996).

[182] C. B. et al. (NA49 Collaboration), J. Phys. G **31** (2005).

[183] V. Friese et al. (NA49 collaboration), PoS(CPOD 2009) p. 005 (2009).

[184] A. Galoyan, J. Ritman, and V. Uzhinsky (2006), nucl-th/0605039, nucl-th/0605039.

[185] Q. Li and M. Bleicher, Journal of Physics G: Nuclear and Particle Physics **36**, 015111 (2009).

[186] S. A. Bass, M. Hofmann, M. Bleicher, L. Bravina, E. Zabrodin, H. Stöcker, and W. Greiner, Phys. Rev. C **60**, 021901 (1999).

[187] F. Wang, M. Nahrgang, and M. Bleicher, Phys. Rev. C **85**, 031902 (2012).

[188] R. M. B. et al, Phys. Rev. D **54**, 1 (1996).

[189] K. Goulianos, Physics Reports **101**, 169 (1983), ISSN 0370-1573.

[190] J. Schwinger, Phys. Rev. **82**, 664 (1951).

[191] J.-X. Sun, J. Kor. Phys. Soc. **59**, 3128 (2011).

[192] T. A. et al. (NA49 Collaboration), Phys. Rev. C. **80**, 034906 (2009).

[193] J. Adams et al. (STAR), Phys. Lett. **B612**, 181 (2005), nucl-ex/0406003.

[194] C. Blume and the NA49 Collaboration, Journal of Physics G: Nuclear and Particle Physics **31**, S685 (2005).

[195] M. Bleicher, J. Phys.: Conf. Ser. **50**, 410 (2006).

[196] J. Steinheimer and M. Bleicher, Eur. Phys. J. **A48**, 100 (2012), 1207.2792.

[197] S. Feng and Y. Zhong, Phys. Rev. C **83**, 034908 (2011).

[198] Y. Mehtar-Tani and G. Wolschin, Phys. Rev. C **80**, 054905 (2009).

[199] Z. Feng-Chu, Y. Zhong-Bao, and Z. Dai-Cui, Chinese Physics Letters **27**, 052503 (2010).

[200] C. Blume and the NA49 Collaboration, Journal of Physics G: Nuclear and Particle Physics **34**, S951 (2007).

[201] I. G. Bearden et al. (BRAHMS Collaboration), Phys. Rev. Lett. **93**, 102301 (2004).

[202] C. Blume, Journal of Physics: Conference Series **230**, 012003 (2010).

[203] M. Broz, Nuclear Physics A **904**, 429c (2013), ISSN 0375-9474.

[204] M. Broz, Nuclear Physics A **904**, 429c (2013), ISSN 0375-9474.

[205] K. Dey and B. Bhattacharjee, Phys. Rev. C **89**, 054910 (2014).

[206] J. Steinheimer, M. Mitrovski, T. Schuster, H. Petersen, M. Bleicher, and H. Stöcker, Physics Letters B **676**, 126 (2009), ISSN 0370-2693.

[207] B. Andersson, G. Gustafson, G. Ingelman, and T. Sjöstrand, Physics Reports **97**, 31 (1983), ISSN 0370-1573.

[208] R. Field and R. Feynman, Nuclear Physics B **136**, 1 (1978), ISSN 0550-3213.

[209] S. A. Bass, Journal of Physics G: Nuclear and Particle Physics **28**, 1543 (2002).

[210] M. L. Miller et al., Ann. Rev. Nucl. Part. Sci. **57**, 205 (2007).

[211] E. Andersen et al., Physics Letters B **449**, 401 (1999), ISSN 0370-2693.

[212] S. Soff, S. Bass, M. Bleicher, L. Bravina, M. Gorenstein, E. Zabrodin, H. Stöcker, and W. Greiner, Physics Letters B **471**, 89 (1999), ISSN 0370-2693.

[213] K. Dey and B. Bhattacharjee, in *Proc. of the DAE Symp. on Nucl. Phys. , Dec. 8-12, 2014.* (2014), pp. 736–737.

[214] J. Randrup and J. Cleymans, Phys. Rev. C **74**, 047901 (2006).

[215] T. Anticic et al. (NA49 Collaboration), Phys. Rev. C **86**, 054903 (2012).

[216] Z.-w. Lin, S. Pal, C. M. Ko, B.-A. Li, and B. Zhang, Phys. Rev. C **64**, 011902 (2001).

List of publications

Publications in refereed journals

1. **Kalyan Dey** and B. Bhattacharjee.

   Separate mass scaling of the widths of the rapidity distributions for mesons and baryons at energies available at the Facility for Antiproton and Ion research

   Phys. Rev. C **89**, (5) 054910 (2014); arXiv:1303.7347 [hep-ph].

2. S. Ahmad, P. P. Bhaduri, H. Jahan, A. Senger, R. Adak, S. Samanta, A. Prakash, **K. Dey**, A. Lebedev, E. Kryshen, S. Chattopadhyay, P. Senger, B. Bhattacharjee, S. K. Ghosh, S. Raha, M. Irfan, N. Ahmad, M. Farooq, B. Singh

   Design and performance simulation of a segmented-absorber based muon detection system for high energy heavy ion collision experiments

   Nuclear Inst. and Methods in Physics Research, A **775** 139-147 (2015).

3. **Kalyan Dey** and B. Bhattacharjee.

   Strange behavior of rapidity dependent strangeness enhancement of particles containing and not containing leading quarks

   Nucl. Phys. A **965**, 74-84 (2017); arXiv:1503.06283 [hep-ph]

Conference Proceedings

1. **Kalyan Dey** and B. Bhattacharjee.

   Rapidity dependence of strangeness enhancement factor at FAIR energies

   Proc. of the DAE Symp. on Nucl. Phys. **59**, 736 (2014).

2. **Kalyan Dey** and B. Bhattacharjee.

   An investigation on the mass/species type behavior of produced particles at FAIR energies - A different approach

   Proc. of the DAE Symp. on Nucl. Phys. **58**, 690 (2013).

3. **Kalyan Dey** and B. Bhattacharjee.

   Pseudorapidity Response of MuCh Detector in FAIR-CBM Experiment

   Proc. of the DAE Symp. on Nucl. Phys. **56**, 1025 (2011).

Technical Reports

1. **Kalyan Dey**, P. P. Bhaduri, S. Chattopadhyay, and B. Bhattacharjee

   Sensitivity of the MUCH in extraction of fireball temperature from dilepton spectra

   CBM progress report 2014, Darmstadt p-130 (2015).

2. **Kalyan Dey** and B. Bhattacharjee.

   Rapidity dependent strangeness enhancement of the produced particles at FAIR energies

   CBM progress report 2014, Darmstadt p-136 (2015).

3. **Kalyan Dey**, S. Chattopadhyay, and B. Bhattacharjee

   Hit finding efficiency and J/ψ reconstruction efficiency of the MUCH detector

   CBM progress report 2013, Darmstadt p-114 (2014).

Conference/Workshop/School Attended

1. Presented a poster at "*7th International Conference on Physics and Astrophysics of Quark Gluon Plasma* (ICPAQGP-2015)" held at Variable Energy Cyclotron Centre, **Kolkata**, (India), 2-6 February, 2015.

2. Oral presentation at National conference "*IXth Biennial Conference of PANE*" held at North Eastern Regional Institute of Science & Technology (NERIST) Nirjuli, **Arunachal Pradesh** (India), 18th-20th December, 2014.

3. Oral presentation at International conference "*Matter at extreme Conditions: Then & Now*" held at Bose Institute **Kolkata**, (India), 18th-20th December, 2014.

4. Presented a poster at "*DAE-BRNS International Symposium on Nuclear Physics*" held at Bhabha Atomic Research Centre, **Mumbai**, (India) 02-04 December, 2013.

5. "*FAIR Computing: Accelerated Computing via GPU*" held at Bose Institute **Kolkata** (India), 11th-15th November, 2013.

6. Presented a poster at "*International Conference on Triggering Discoveries in High Energy Physics*" held at Department of Physics and Astrophysics, Jammu University, **Jammu** (India), 09-14th September, 2013.

7. Oral presentation at "*CBM Collaboration meeting and CBM software school*" held at VECC **Kolkata** (India), 2012.

8. Participated at "*QGP meet 2012*" held at VECC **Kolkata** (India), 2012.

9. Participated at "*SERC school on Experimental High Energy Physics*" held at VECC **Kolkata** (India), 2012.

10. Participated at "*CBM software workshop*" held at **Ebunburg Castle** (Germany), 2011.

11. Participated at "*Physics and Astro Physics of Quark Gluon Plasma* (ICPAQGP)" held at National Institute of Oceanography, **Goa** (India), 2010.

12. Participated at "*QCD in medium*" held at Calcutta University, **Kolkata** (India), 2010